Search for top-antitop quark resonances with the ATLAS detector at the Large Hadron Collider

Bertrand Chapleau

Doctor of Philosophy

Physics Department

McGill University

Montréal,Québec

March 2014

A thesis submitted to McGill University in partial fulfillment of the requirements of the degree of Doctor of Philosophy

DÉDICACE

À mes parents, Marc et Sylvie, et mon frère Julien.

ACKNOWLEDGEMENTS

ABSTRACT

The intriguing nature of the top quark, by far the heaviest particle in the Standard Model of particle physics, has motivated the development of many theoretical extensions predicting the existence of new massive particles decaying to a pair of top-antitop quarks. The production of these hypothetical particles in proton-proton collisions at the Large Hadron Collider would reveal itself as a resonance in the expected smooth distribution of the top-antitop quark invariant mass. This thesis presents a search for such a new heavy particle decaying to a pair of top-antitop quarks in the semi-leptonic final state. The analyzed data sample amounts to a total of 4.6 fb^{-1} at a proton-proton collision center-of-mass energy of 7 TeV. Novel techniques specifically tailored to the identification of the decay products of highly energetic top quarks are developed and used. No evidence for resonant production of pairs of top-antitop quarks is found and, as a result, constraints are set on two theoretical models. Upper limits on the production cross-section times branching ratio are established at a 95% credibility level for a leptophobic Z' boson from the Topcolor model, and a Kaluza-Klein gluon from the Randall-Sundrum model. The Z' boson and the Kaluza-Klein gluon are excluded to exist (at a 95% credibility level) in the mass ranges 0.8-1.65 TeV and 0.8-1.88 TeV, respectively. The constraints derived in this thesis on the two theoretical models are more stringent than the ones obtained at other experiments, thanks to the large center-of-mass energy and the dedicated high-energy top quark identification techniques used.

ABRÉGÉ

La nature intrigante du quark top, de loin la particule élémentaire la plus lourde du Modèle standard de la physique des particules, a motivé le développement de nombreuses théories prédisant l'existence de nouvelles particules massives se désintégrant en une paire de quarks top-antitop. La production de ces particules hypothétiques dans des collisions de type proton-proton au Grand collisionneur de hadrons (LHC) se manifesterait sous la forme d'une résonance dans la distribution de la masse invariante des paires de quarks top-antitop. La présente thèse consiste en une recherche d'une telle particule se désintégrant en une paire de quarks top-antitop dans l'état final dit semi-leptonique. La taille de l'échantillon de données analysé équivaut à 4.6 fb^{-1} à une énergie de centre de masse des collisions proton-proton de 7 TeV. Des techniques novatrices d'identification des produits de désintégrations de quarks top à grande énergie sont développées et utilisées. La présence d'une résonance dans la production de paires de quarks top-antitop n'a pu être établie et, conséquemment, des contraintes sont dérivées sur deux modèles théoriques. Des limites supérieures sur la section efficace de production multipliée par le rapport de branchement sont établies avec un niveau de crédibilité de 95% pour un boson Z' leptophobique du modèle Topcolor, ainsi que pour un gluon Kaluza-Klein du modèle Randall-Sundrum. Le boson Z' et le gluon Kaluza-Klein sont proscrits (avec un niveau de crédibilité de 95%) dans la région de masse 0.8-1.65 TeV et 0.8-1.88 TeV respectivement. Grâce à la grande énergie de centre de masse ainsi qu'aux techniques spécialisées d'identification des quarks top de grande énergie, les contraintes dérivées dans la présente thèse sur les

deux modèles théoriques ici considérés sont plus restrictives que celles obtenues par le biais d'autres expériences.

AUTHOR'S CONTRIBUTION

This thesis builds upon a lot of research, work and effort from the whole ATLAS collaboration and the LHC community in general, which involves thousands of physicists, engineers and technicians. The results presented herein thus rely on a complex *machinery* (software framework, Monte Carlo simulations, grid computing infrastructure, etc.) developed for and by the collaboration. The data analysis that led to these results, including the production of all the tables and plots, was performed by the author itself, unless stated otherwise. In addition, the author contributed to the collaboration-wide effort in two specific areas: the jet trigger and the software implementation of jet substructure reconstruction algorithms.

The jet trigger performance was enhanced by allowing the anti-k_t jet reconstruction algorithm to run, at the Event Filter, on topological clusters. For analyses dealing specifically with boosted topologies, the use of large-R jets ($R = 1.0$) at the Event Filter level also improves the trigger selection efficiency. The addition of those new jet trigger features was achieved (by the author) by porting the offline software tools into the online computing environment where the said features were thoroughly validated.

The implementation of the jet trimming procedure and the jet substructure observables into the main ATLAS software framework was performed by the author. The author also designed and configured derived data samples production software modules specific to analyses relying on jet substructure. These modules were used in

the production of official ATLAS derived data samples used by all ATLAS analyses using jet substructure observables.

TABLE OF CONTENTS

LIST OF TABLES

LIST OF FIGURES

CHAPTER 1
Introduction

Over the last century, our understanding of Nature has come to a point of remarkable refinement. From molecules, to atoms, to nucleons, to today's elementary particles, the description of the "infinitely small" reached many fundamental milestones that changed our perception of Nature. To date, the most accurate model of Nature's internal mechanisms is known as the Standard Model of particle physics; a theory which describes all known elementary particles as well as how they physically interact with each other. Developed over the past several decades, the Standard Model is a very successful theory whose predictions have been verified many times, notably at large-scale particle accelerator experiments. Despite this apparent success, some aspects of the subatomic world remain unexplained by this theory. Several theoretical models have thus been developed to overcome its current limitations. Many of those models predict the existence of one or several new heavy particles that are yet to be discovered. The observation of such new particles would therefore be an unambiguous indication of the existence of new physics phenomena beyond those described by the Standard Model.

The present thesis consists of a search for evidence of the existence of such a new heavy particle which is expected to be produced in proton-proton collisions at the Large Hadron Collider (LHC) particle accelerator. The search is performed by looking for the distinctive features that characterize its expected disintegration using

data recorded by the ATLAS detector. At the LHC, ionized hydrogen atoms (protons) collide at relativistic speeds. The large amount of energy released in a collision is such that a plethora of particles is spontaneously produced. The ATLAS detector identifies the trajectory and energy of the particles produced in each collision, effectively taking a three dimensional "picture" of the result of each collision. The presence or absence of the new physics phenomenon can then be assessed by looking for specific and repetitive patterns in those pictures.

The remainder of this chapter briefly presents basic concepts of the Standard Model as well as provides an overview of the present analysis. Chapter 2 gives more detailed insights into the theory describing interactions among elementary particles and the expectations related to the observation of the new particle searched for. Chapter 3 describes the experimental setup, the ATLAS detector at the LHC, used to carry out the search for a new particle. Chapter 4 details the algorithms employed for reconstructing and identifying the different experimental signatures based on the information recorded by the detector. Chapter 5 presents the strategy for selecting collisions featuring experimental signatures that are consistent with the disintegration of the hypothetical particle searched for. Chapter 6 details the different systematic uncertainties considered in the present analysis. The results of the search are presented in Chapter 7. Finally, Chapter 8 discusses the constraints that are established on different theoretical models, and concluding remarks are found in Chapter 9.

1.1 Theory overview

The Standard Model (SM) of particle physics [1] is the theoretical framework describing interactions among elementary particles due to three of the four fundamental forces in Nature: the electromagnetic, the weak, and the strong forces [1] . In its current form, the SM, which was developed over the past half century, includes two types of particles, fermions and bosons. The former consists in leptons and quarks, the constituents of matter that surround us, and the latter in bosons, particles that are often thought of as force *carriers*. Figure 1–1 presents the elementary particles of the SM and their intrinsic properties.

Fermions are characterized by their intrinsic spin quantum number (an analog of angular momentum) of half-integer value. Particles called leptons are fermions which are further characterized by an integer electric charge of one unit for the massive electron, muon and tau leptons, and null electric charge for the almost massless corresponding neutrinos. Quarks, on the other hand, are fermions that have a fractional electric charge of 2/3 for *up*-type quarks (up, charm, top), and −1/3 for the *down*-type quarks (down, strange, bottom). Quarks are observed in nature solely in the form of bound states known as hadrons, such as protons and

---

[1] The gravitational force is several orders of magnitude weaker in strength and is thus completely negligible at the energy scale the experiment is carried out.
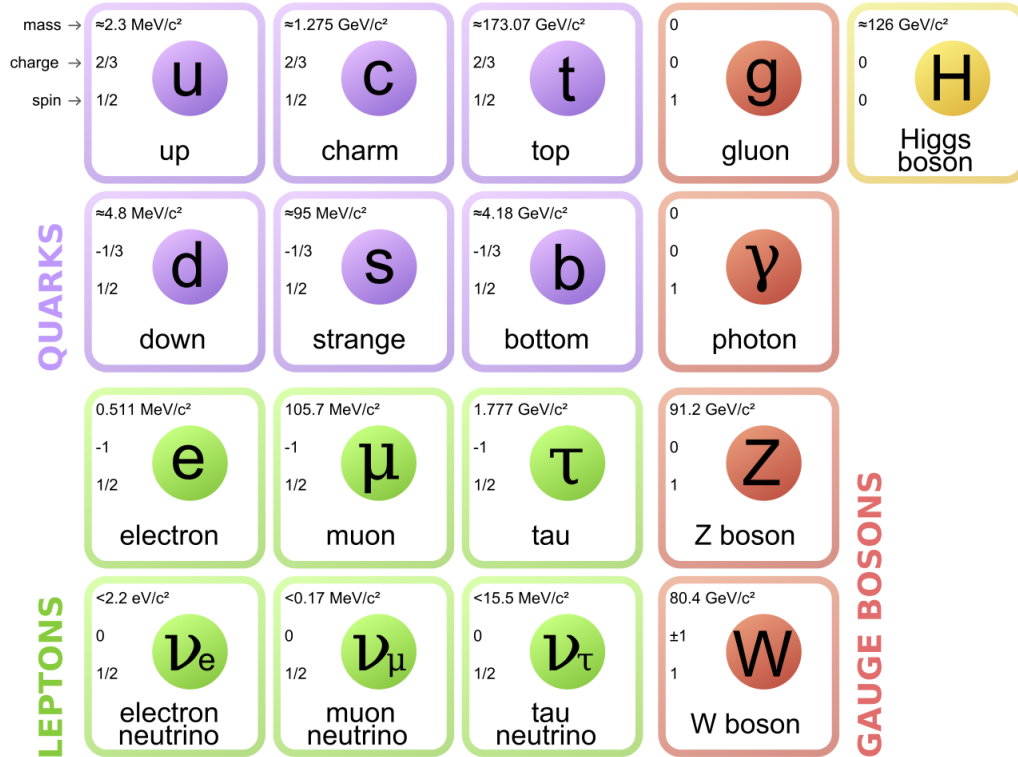
Figure 1–1: Elementary particles in the Standard Model. Taken from [2].

neutrons. Each fermion is further accompanied by its *antiparticle* which has the same mass but opposite quantum numbers such as the charge(s)[2] .

---

[2] A charge is a quantum number associated with a fundamental force. Example of charges are the electric charge for electromagnetic interactions and the so-called color charge for strong interactions.

Bosons, for their part, have spin of integer value and mediate the interactions (forces, at the macroscopic level) among the elementary particles. Photons are responsible for electromagnetic interactions and couple to any electrically charged particles. The $W^{+/-}$ and Z bosons are massive particles and mediate the weak interactions. Through its exchange, the W boson[3] has the ability to induce flavor changing among fermions (from an *up*-type quark to a *down*-type quark or from a charged lepton to a neutrino, and vice-versa). The mathematical descriptions of the interactions involving these four bosons, together with the photon, were unified in a unique theory, the electroweak theory, by Glashow, Salam and Weinberg in the 1960's [3, 4, 5].

The Higgs boson is an elusive particle of the Standard Model that was experimentally observed very recently. Indeed, in July 2012, both the ATLAS and CMS experiments claimed strong evidence for the production of a new neutral boson with a measured mass of about 125 GeV [6, 7] and with properties compatible with that of the Standard Model Higgs boson. The Higgs boson plays a special role in the Standard Model. It reveals the existence of the postulated Higgs field [8, 9, 10, 11] which accounts for the different masses of the electroweak bosons[4] . The existence of this field also gives rise to the masses of all known particles.

---

[3] Throughout this thesis, a W boson refers to either W^+ or W^-, similarly for charged leptons.

[4] The so-called Higgs mechanism provides an explanation for the breaking of the underlying symmetry of the electroweak theory.

Finally, the massless gluons are the carriers of the strong force and interact with quarks as well as with themselves by virtue of the fact that they carry a so-called *color* charge. The color charge is an ad-hoc quantum property of quarks and gluons that gave rise to the theory of the strong interaction, quantum chromodynamics.

1.2 Analysis overview

The analysis conducted in this thesis consists in identifying experimental signatures compatible with the production of a new heavy particle decaying to a pair of top-antitop quarks. To this end, a set of criteria was developed to isolate the recorded outcome of certain proton-proton collisions which exhibit features consistent with those signatures. These criteria are based on novel techniques that are exploited to identify patterns of disintegration in line with what is expected from top quarks produced with a large amount of energy (which are said to be *boosted*).

The invariant mass of the detected decay products of the top and antitop quarks produced as a result of the disintegration of a new heavy particle should be equal to the mass of the new particle. The invariant mass of the detected top and antitop quark candidates is therefore compared to the Standard Model predictions to search for hints of the existence of a new particle. No evidence for such a new particle decaying to a pair of top and antitop quarks is found. In light of this result, constraints are calculated on parameters describing the properties of new heavy particles in two different theoretical extensions of the Standard Model. The constraints on the two specific models presented in this thesis surpass the ones obtained in previous experiments.

CHAPTER 2
Theory

The strong interaction plays an essential role at the LHC. Pairs of top-antitop quarks are for instance produced in proton-proton collisions via the strong interaction. Properties of the strong force also explain the observation of collimated sprays of particles called *jets* in collisions involving quarks or gluons in the final state.

This chapter describes the properties of the theory of strong interactions that are relevant at high energy colliders. A description of the top quark production mechanisms and detection is also presented.

2.1 Theory of strong interactions

Quantum Chromodynamics (QCD) is a quantum field theory that describes interactions induced by the strong force among elementary particles (quarks and gluons) [12]. This theory explains a rich set of experimental results that notably exposed the composition of the proton.[1] The development of QCD followed Feynman and Bjorken's proposal of the so-called *parton* model [13, 14] where hadrons can be viewed, at high energies (or equivalently, at small distances or short timescales), as composite objects made of a small number of pointlike constituents, the partons[2] ,

---

[1] Such as experiments conducting (deep inelastic) scatterings of electrons onto proton targets in the late 1960's at the Stanford Linear Accelerator Center laboratory and more recently at HERA.

[2] A parton is the generic term referring to either a quark or a gluon.

which barely interact among themselves within the confines of the hadron. This property, where the interaction strength between partons diminishes at small distances, is known as *asymptotic freedom* [15] and is a key feature of the theory of QCD. Asymptotic freedom is naturally accounted for by non-abelian gauge theories[3] such as QCD by means of an energy-scale dependent coupling constant[4] that becomes small at short distances.

One fortunate consequence of asymptotic freedom is that calculations in QCD can be carried out perturbatively at high energies, a regime where the coupling constant is small enough to render perturbation theory a legitimate approximation to an exact solution that is otherwise too difficult to obtain.

Particles (quarks and gluons) that interact through the strong force are characterized by an extra quantum property, the "color charge" which can take six different values. The color charges are referred to as (anti) red, (anti) blue and (anti) green. Quarks can carry one of the three color charges whereas anti-quarks carry anti-color charges. Gluons, on the other hand, can carry a mixture of color and anti-color charges. The strong interaction thus takes place among color-charged particles through the exchange of gluons, the quanta of the field mediating the force (analogous to photons for electrically charged particles). The increasing force quarks exert

---

[3] A non-abelian gauge theory is a field theory for which the Lagrangian is invariant under a set of gauge transformations. This set forms a so-called symmetry group which is said to be non-abelian, i.e. non-commutative.

[4] A *coupling constant* determines the strength of an interaction in a given theory. In the case of the strong force, the coupling constant is represented by the symbol α_s.

on each other as they are pulled apart is explained in QCD through the property of *color confinement* [16, 17, 18]: the only stable states of the theory are the ones for which quarks are confined into colorless bound states (hadrons), prohibiting the observation of "bare" quarks. Thus, quarks produced in a short timescale interaction will very rapidly form hadrons by combining with other quarks in order to respect color confinement. This is a key result that explains the experimental observation of collimated sprays of particles, or *jets*, where one would have otherwise expected to detect individual quarks or gluons.

Along with our increasing understanding of physics processes involving the strong force, a more refined description of hadrons arose. In this refined model, most of the hadron's momentum is carried by the so-called *valence* quarks[5] , but that are immersed in a *sea* of quark-antiquark pairs (of all flavors) and gluons carrying a small fraction of the total hadron's momentum. The probability for an impinging particle to interact with a quark or gluon inside a hadron is modeled by parton distribution functions (PDFs) [19]. The PDFs are functions of the momentum fraction carried by the parton inside the hadron and of the momentum transferred in the interaction with the incoming particle.

QCD predictions can be experimentally tested in hadron collisions at high energies such as those at the LHC. In a high energy proton-proton collision, the interaction taking part among two partons (from each one of the incoming protons)

---

[5] For instance, the two *up* quarks and the *down* quark in the proton.

is known as the hard scattering process. Hard scattering of partons can be studied using perturbative QCD, provided that the momentum transfer is large enough. When this requirement is met, the strong coupling constant α_s [1] is small and thus allows for a perturbative expansion of QCD calculations in α_s through the use of the Feynman diagram approach [20]. Feynman diagrams are a visual representation of the different terms in the perturbative series expansion of a given calculation in QCD.

2.1.1 Jets

Jets are complex objects produced in high energy collisions involving partons (quarks or gluons) in the final state. They are observed as collimated sprays of particles, mostly light hadrons. Even though the exact details that bring a final-state parton resulting from a hard scattering to detectable hadrons are not yet fully understood in QCD, jets can nevertheless be used to assess our understanding of high-energy QCD processes, and as a means to identify (non-leptonic) decay products of massive particles.

Loosely speaking, the formation of a jet can be viewed as a two-step process. An outgoing parton will first undergo a series of gluon emissions that might themselves radiate and/or produce quark-antiquark pairs. At short enough timescales (that is at sufficiently large momentum), part of this process can be described by perturbative QCD calculations. However, low energy gluon emissions at small angle (with respect to the original parton) still dominate and result in a cascade of collimated partons. It is only later that quarks combine in a non-trivial fashion to form hadrons, in view of color confinement, a highly non-perturbative QCD mechanism known as

hadronisation. It is the collective identification of those observed hadrons, according to some well defined prescription, that defines a jet. To some extent, the kinematic properties (energy and direction) of a jet are correlated with that of the parton that initiated the hadronic cascade later observed as a jet.

2.2   Top quark

The top quark has a fairly recent (experimental) history, having been discovered less than 20 years ago[6] by the CDF [21], and DØ [22] collaborations at Fermilab. Its distinctive feature is unarguably its mass of about 173 GeV [7] [1], by far the heaviest elementary particle of the Standard Model. Furthermore, the Standard Model predicts its lifetime to be shorter than the timescale associated with quark hadronisation [1], and as a consequence, the top quark will decay long before any hadronisation can take place. Its intriguing high mass suggests also that it might play a non trivial role in Nature with potential links to phenomena *beyond* those described by the Standard Model.

---

[6] Although its existence was postulated in the 1970's.

[7] Natural units with $c = 1$ are used throughout this thesis.

2.2.1   Top quark production

In hadron-hadron collisions, top quarks are mainly produced in pairs of top-antitop $(t\bar{t})$ [8] , according to the Standard Model. Those pairs are produced via the strong interaction predominantly through quark-antiquark annihilation and gluon-gluon fusion mechanisms; the leading order Feynman diagrams depicting those processes can be found in figure 2–1. The overall relative importance of the two produc-

(a) gluon-gluon fusion   (b) $q\bar{q}$ annihilation
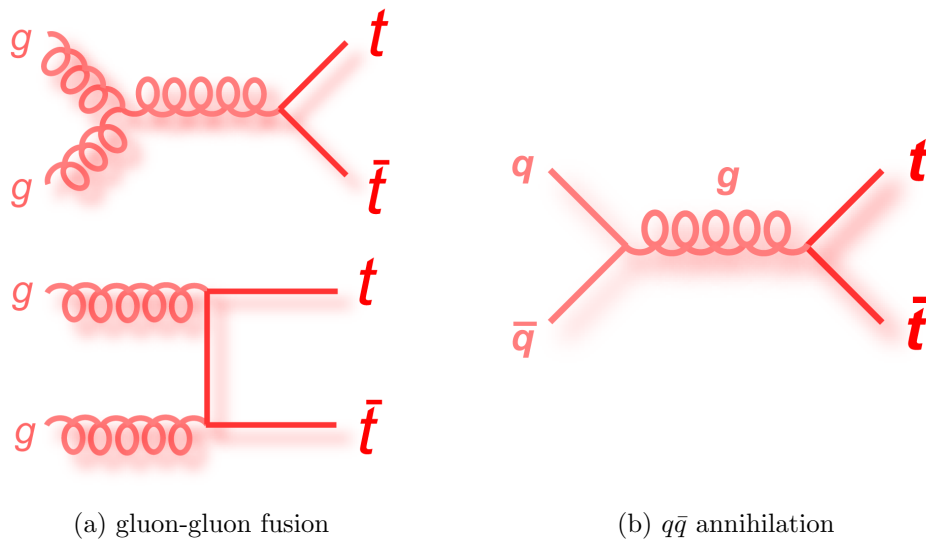
Figure 2–1: Leading order Feynman diagrams for $t\bar{t}$ production at hadron colliders, according to the Standard Model. One diagram for gluon-gluon fusion where the incoming partons cross is not shown. Time evolves from left to right. Taken from [23].

tion mechanisms depends on the center-of-mass energy $\sqrt{s}$ of the colliding hadrons.

---

[8] The other relevant production mechanism in the SM is the *single top* production which is approximately two times less likely to occur than $t\bar{t}$ production.

At the Tevatron[9] , proton-antiproton collisions occurred at $\sqrt{s} \sim 2$ TeV. For the kinematical threshold of top-antitop production (twice the top quark mass) to be reached, the interacting partons had to carry a significant fraction of the colliding (anti)protons, a regime in which the valence quarks are probed. At the LHC, on the other hand, given the large center-of-mass energy of 7, 8 and eventually 14 TeV, the incoming partons are only required to carry a small fraction of the proton's momentum. In these conditions, the interaction between two gluons is much more likely to occur than that of a quark and anti-quark because the gluon PDF dominates [24]. Gluon-gluon fusion is thus the leading production mechanism of top-antitop pairs at the LHC according to the Standard Model.

The number of expected events[10] where a pair of top-antitop quarks is produced is predicted by the Standard Model. It is quantified via the cross-section $\sigma_{t\bar{t}}$, which can be thought of as a probability for a specific process to occur (in this case, the production of a $t\bar{t}$ pair). The cross-section depends notably on the center-of-mass energy of the colliding hadrons. At the LHC collision center-of-mass energy of 7 TeV, the top-antitop quark production cross-section is estimated to be $\sigma_{t\bar{t}}(\sqrt{s} = 7 \text{ TeV}) = 158.7^{+13}_{-14}$ picobarns[11] [25]. In the calculations presented in [25], the mass of the top is taken to be 173.3 GeV . The super- and sub-script numbers

---

[9] The Tevatron was a proton-antiproton collider at Fermi National Accelerator Laboratory in the United-States. It was in operation from 1985 to 2011.

[10] An event is the result of a proton-proton collision

[11] A barn is equivalent to 10^{-24} cm^2 and picobarns can be abbreviated as "pb".

represent the up and down theoretical uncertainties on the cross-section calculation. In contrast, at the Tevatron, where proton-antiproton beams were made to collide at a center-of-mass energy of 1.96 TeV, the cross-section is calculated to be $\sigma_{t\bar{t}}(\sqrt{s} = 1.96 \text{ TeV}) = 6.7^{+0.3}_{-0.4}$ pb [25]. When comparing an equal amount of total events, this means that for every $t\bar{t}$ pair produced at the Tevatron, more than 20 are produced at the LHC. In the data sample collected in 2011 at the LHC, about 800 thousand events are expected to contain a $t\bar{t}$ pair[12] .

2.2.2 Top quark decay

The top quark decays through the electroweak force to a W boson and a b quark almost 100% of the time. Because the W boson is unstable and itself decays, one can classify the top-antitop pair decay types according to the decay products of the two W's in play. To a first approximation, a W will decay with equal probability to a charged lepton-neutrino pair or to a pair of light quarks, thus its total leptonic branching ratio (fraction of decays to a leptonic final state) is $\sim \frac{1}{3}$, and its hadronic branching ratio is $\sim \frac{2}{3}$ [13] .

In the remainder of this thesis, focus will be put on the production of top-antitop quark pairs. Figure 2–2(a) gives an overview of the possible $t\bar{t}$ decay channels. In this

---

[12] The number of expected events is given by the relation $N_{t\bar{t}} = \sigma_{t\bar{t}}\mathcal{L}$, where $\mathcal{L}$ is the *integrated luminosity* of the 2011 data sample which amounts to ~ 5000 pb^{-1}.

[13] A W boson can decay into three possible charged lepton-neutrino pairs and into two quark-antiquark pairs each carrying one of the three possible color-anticolor charge (for a total of six different pairs involving (anti)quarks). There are thus 3 out of 9 decays involving leptons, and 6 out of 9 involving light (anti)quarks.

table, each decay channel is represented by a colored rectangle or square whose area is roughly proportional to the corresponding branching ratio. For a given channel, the visible decay products of the W produced in the disintegration of the top (antitop) quark are listed at the bottom of the column (left of the row).

(a) $t\bar{t}$ decay channels.

(b) Diagram of a lepton+jets $t\bar{t}$ decay.

Figure 2–2: The table in (a) summarizes the different classes of decay channels, and their relative importance, for a pair of top-antitop quarks. Shown in (b) is a visual representation of the lepton+jets top-antitop quark pair decay. The collision occurred at the center and time evolves outward (length of lines is for presentation purposes only). Taken from [23].

The most statistically favored channel is the so-called "all-hadronic" channel where both Ws decay to pairs of light quarks. It is an experimentally challenging channel to observe because of the overwhelming background, i.e. processes that do not involve any top quark production but that nevertheless give rise to events with a lot of jets. Although it is experimentally easier to identify and reconstruct the leptonic disintegration of a W boson, top-antitop decays where both W bosons

decay leptonically (so called dilepton channel) only account for approximately 10% of all the $t\bar{t}$ decays. The second most common outcome of a $t\bar{t}$ decay is when only one of the Ws decays to a pair of quarks, and the other one decays leptonically (see figure 2–2(b)). This disintegration chain is typically referred to as the lepton+jet channel. When the lepton[14] is either an electron or a muon, this channel accounts for about 30% of all the possible decay types[15] . The tau lepton is omitted for experimental reasons: it is unstable and decays before reaching the detector, making its identification much more difficult. The lepton+jets decay channel provides a good signal over background ratio and adequate statistics and is therefore said to be the golden channel to identify events where a top-antitop pair has been produced.

In this thesis, only the electron+jets ($t\bar{t} \to WbWb \to e\nu_e bq'\bar{q}b$) and muon+jets ($t\bar{t} \to WbWb \to \mu\nu_\mu bq'\bar{q}b$) channels will be considered.

2.2.3   Top quark reconstruction

At the unprecedented energies the LHC is operating at, top quark decays are a source of new experimental phenomenology. Indeed, at previous experiments such as the ones at the Tevatron accelerator, top quarks were produced with a small amount of momentum in the laboratory frame. Top quarks were thus identified by resolving individually each disintegration particle and reconstructing the decay chain. At

---

[14] In the remainder of this thesis, for brevity, the term lepton will refer to a *charged* lepton.

[15] One of the Ws decays to either an electron or a muon, while the other W decays to a pair of light (anti)quarks. Mathematically: $2 \times \left(W^{+/-} \to e^{+/-}\nu_e \text{ OR } W \to \mu^{+/-}\nu_\mu\right)$ AND $\left(W^{+/-} \to q'\bar{q}\right) = 2 \times \left(\frac{1}{9} + \frac{1}{9}\right) \times \frac{2}{3} \approx 0.3$

the LHC energies however, a top quark is often produced with a large amount of momentum, and its decay products will tend to be collimated. As a result, regular identification algorithms fail to identify each decay product. Novel identification techniques are therefore required to identify the (Lorentz *boosted*) top quark disintegration products. These new techniques will be discussed in detail in Chapter 5.

2.3   Beyond the Standard Model

Despite many successful predictions, it is known for a fact that the Standard Model cannot be a complete and self-consistent theory of particle physics. Indeed, because of various theoretical aspects, the Standard Model is merely an approximation (although very accurate) to some more encompassing yet unknown theory. The Standard Model does not explain, for instance, why particles have the masses they have, or why gravity is so weak with respect to the other fundamental forces of Nature. Searching for experimental evidence of new phenomena, that cannot be accounted for by the Standard Model, is thus an essential step in establishing the viability of new candidate theories that attempt to address some of the Standard Model shortcomings.

Many of those theoretical models predict the existence of one or several new massive particles decaying in a large proportion to a pair of top-antitop quarks. Two specific models will be briefly outlined in the subsequent sections.

The reconstructed top-antitop invariant mass is defined as

$$\mathrm{M}_{t\bar{t}} \equiv \sqrt{\left(p^{\bar{t}} + p^{t}\right)_{\mu} \left(p^{\bar{t}} + p^{t}\right)^{\mu}} \, , \tag{2.1}$$

17

where p is the top four-momentum and a sum over the components $\mu = 0, ..., 3$ is implicitly assumed. Because of the top quark's high mass, no real particle predicted by the Standard Model is allowed to decay into a top-antitop pair. $M_{t\bar{t}}$ is therefore expected to exhibit a smooth and exponentially decreasing distribution of masses (spectrum). A new heavy particle that would primarily decay to a top-antitop pair would therefore reveal itself as a resonance (a "bump") in the $M_{t\bar{t}}$ spectrum (as predicted by the Standard Model), thus providing a model-independent way of searching for the existence of such new particles.

2.3.1 Topcolor model

The Topcolor model [26, 27, 28] was developed to naturally explain the large top quark mass as well as to provide a mechanism for the electroweak symmetry breaking[16] . In this model, the masses of the bottom and top quarks need to be regulated so that the b-quark stays light with respect to the top quark. This is indirectly achieved by introducing a heavy neutral gauge boson Z' which exhibits an enhanced coupling to top quarks. In particular, Model IV presented in [27] predicts the existence of such a (leptophobic) Z' boson that strongly couples only to the first and third generation of quarks, with a preference for top quarks[17] . This Z' could reveal itself as a narrow resonance (with a width of a few percent of its mass) in the top-antitop invariant mass distribution (spectrum). Figure 2–3 shows a schematic

---

[16] The mechanism by which some of the fermions and W/Z bosons acquire mass.

[17] For this particular model, the Z' boson decays one third of the time into top quarks

diagram of the production and decay of the Z'. In the present work the width of the Z' was set to 1.2% in order to be able to compare results with other experiments that used the same assumptions. The predicted production cross-section decreases with increasing mass of the Z'; it is approximately 1 pb (0.02 pb) for $m_{Z'} = 1$ TeV ($m_{Z'} = 2$ TeV), including the branching ratio into $t\bar{t}$.
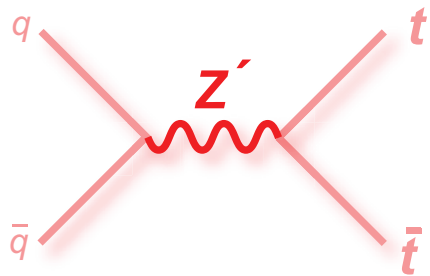
Figure 2–3: Leading order Feynman diagram of a Z' boson, predicted to exist in the Topcolor model, decaying to $t\bar{t}$. Time evolves from left to right. Taken from [23].

2.3.2 Randall-Sundrum model

In the Randall-Sundrum scenario [29, 30], one warped (curled up) dimension is added to the usual four dimensional space-time. This model was proposed in order to solve the so-called hierarchy problem[18] . In this particular model, the Standard Model quantum fields (and corresponding particles) are free to propagate in the extra warped spatial dimension. The excitation of a SM particle into this extra dimension results in massive excited states of the said particle known as Kaluza-Klein (KK) excitations. The first excitation of the gluon (g_{KK}) in a basic Randall-Sundrum

---

[18] This is related to the large difference between the strength of the electroweak force and gravity.

scenario, notably, is predicted to acquire enough mass to decay to a pair of top-antitop quarks. In the Randall-Sundrum model, the g_{KK} decays primarily to top quarks (92.5% of the time [30]) and would reveal itself as a broad resonance in the top-antitop invariant mass spectrum. For example, its width is calculated to be 15.3% of its mass in the basic Randall-Sundrum scenario considered in this thesis [31]. The g_{KK} does not couple to regular gluons and thus the main predicted production mechanism is through quark-antiquark annihilation. The predicted production cross-section also decreases with the mass of the g_{KK}; it is approximately 4 pb (0.1 pb) for $m_{g_{KK}} = 1$ TeV ($m_{g_{KK}} = 2$ TeV), including the branching ratio into $t\bar{t}$.

CHAPTER 3
Experimental environment

The experimental apparatus used in this analysis comprises the Large Hadron Collider particle accelerator and the ATLAS detector, located at the CERN laboratory near Geneva.

At the Large Hadron Collider, particles created in proton-proton collisions are detected by two general purpose detectors, ATLAS and CMS, and two specialized ones, ALICE (Heavy Ions physics) and LHCb (b quark physics). The substantial amount of data recorded since the first collisions in 2010, combined with the highest center-of-mass energy ever achieved in a laboratory, provide a unique environment to search for new physics phenomena beyond the Standard Model.

In 2010 and 2011, proton-proton collisions occurred at a center-of-mass energy of $\sqrt{s} = 7$ TeV as a first step in the commissioning of this new machine. In 2012, the collision center-of-mass energy was $\sqrt{s} = 8$ TeV. The design value $\sqrt{s} = 14$ TeV is the next milestone soon to be reached.

This chapter first describes details of the particle accelerator operation and of different components of the ATLAS detector most relevant for this work. The data set and different event simulation programs used are also described.

3.1   The Large Hadron Collider

The Large Hadron Collider (LHC) [32] is a proton[1] accelerator and collider complex installed in an underground 27 km long circular tunnel straddling the French-Swiss border. The LHC consists of two rings in which counter-rotating beams of protons travel. These beams are set to cross, and hence protons to collide, at four different interaction regions along the circular path, where four detectors can record the outcome of the collisions.

The LHC injector complex, depicted in Figure 3–1, consists of four distinct smaller particle accelerators. They work in concert to accelerate protons from rest, before injecting them in the LHC main rings where they are further accelerated. Protons are obtained from hydrogen gas by stripping off electrons using an electric field. They are then accelerated in the Linear Accelerator 2 up to an energy of 50 MeV. The protons, arranged in *bunches*, are then injected in the Proton Synchrotron Booster in which they are accelerated to an energy of 1.4 GeV. The purpose of the Booster is to allow higher intensity beams to be fed to the Proton Synchrotron[2]. The Proton Synchrotron further accelerates the proton up to an energy of 25 GeV while generating bunches with the required spacing of 25 nano-seconds using radio frequency cavities. These bunches are finally accumulated into the Super Proton Synchrotron where protons acquire an energy of 450 GeV before being

---

[1] The LHC also has an heavy-ion (lead-lead) program, where lead nuclei are set to collide instead of protons, as well as a proton-lead program.

[2] The Booster helps to overcome the so-called space-charge limit of the Proton Synchrotron [33].

injected into the LHC rings. In the LHC itself, a series of radio frequency resonant cavities is used to accelerate protons up to their final energy.
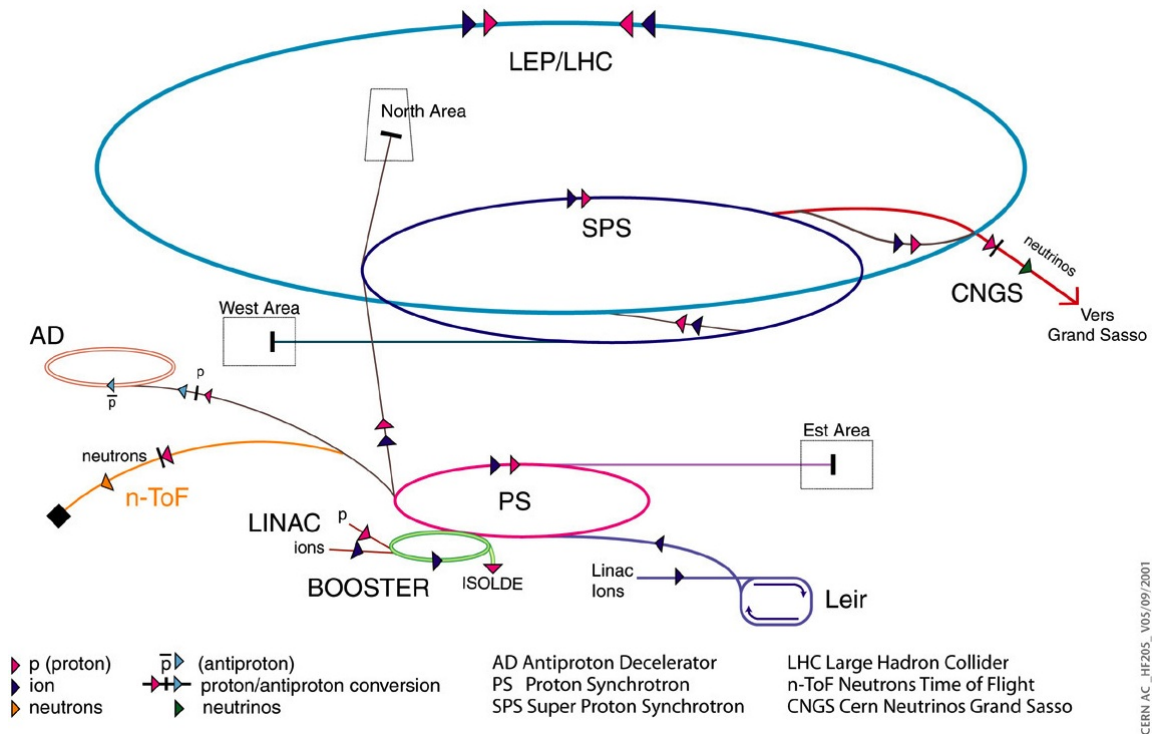
Figure 3–1: Diagram of the LHC injector complex. [34]

One of the many engineering *tour de force* that made the LHC program possible is the use of a novel superconducting dipole magnet design [32] aimed at confining the proton beams in a circular trajectory around the LHC ring. The LHC magnets can provide a peak magnetic field of 8.33 Teslas which will eventually make it possible to steer protons around the rings at an energy of 7 TeV, giving rise to collisions at an unprecedented center-of-mass energy of $\sqrt{s} = 14$ TeV. Quadrupole magnets are used to keep the beams focused along the rings. Additional quadrupole magnets are

employed in the vicinity of the interaction regions in order to squeeze the beams down to 16 micrometers in the transverse dimension. A small beam transverse size increases the collision rate.

A typical LHC cycle consists in first accelerating protons in the injector complex and into the LHC. Collisions then occur once the desired energy is achieved and detectors start collecting and recording data. As time passes, fewer and fewer protons are present in the beams and the collision rate decreases. After approximately 20 hours, it becomes more efficient to dump the beams and re-start a new cycle.

The rate at which specific events are produced as a result of proton-proton collisions is defined as

$$\frac{dN}{dt} = \sigma L \ , \tag{3.1}$$

where σ is the cross-section of a given process, and where the proportionality constant L is referred to as the instantaneous luminosity of the machine (a measure of the beam intensity). The cross-section can be thought of as the probability of producing a certain type of event as a result of proton-proton collisions at a fixed center-of-mass energy. For a rare process (i.e. that is characterized by a small cross-section) to happen in a finite amount of time, the particle collider needs to deliver a high event (collision) rate which is quantified by a high value of L.

The LHC is designed to eventually operate at $L = 10^{34}$ cm^{-2}s^{-1}. In 2011, the maximum instantaneous luminosity achieved was $\mathcal{O}\left(10^{33}\right)$ cm^{-2}s^{-1} which fulfilled the expectations for the first few years of exploitation of the machine. Figure 3–2 presents the instantaneous luminosity as well as the integrated luminosity $\mathcal{L} \equiv \int L dt$

24

delivered by the LHC during the 2011 data taking campaign. More than 5 fb^{-1} worth of data was recorded by the ATLAS detector that year.

The instantaneous luminosity achieved depends in part on the number of protons present in the beams. Protons making up the two beams are arranged into bunches each consisting of billion of particles. The LHC will be able to accommodate 2808 such bunches, separated by 25 nano-seconds. This corresponds to a beam current of about 0.58 A. During the 2011 data taking period, a maximum of about 1300 bunches per beam at 50 ns spacing were used. It is the crossing of two incoming bunches at an interaction point (where the detectors are located) that gives rise to the proton-proton collisions per se. When two "clouds" of protons (i.e. the colliding bunches) pass through each other, only a few $\mathcal{O}(10)$ protons will actually collide, with different amounts of momentum transfer. A *single* event may thus consist of a hard (large momentum transfer) collision accompanied by additional proton-proton interactions from the current bunch crossing. This feature is inherent to high luminosity data taking and is known as in-time pile-up.

3.2 The ATLAS detector

The ATLAS[3] detector[36] is one of two general purpose detectors at the LHC. It is designed to have the ability to identify a wide variety of physics signatures at the highest instantaneous luminosity expected to be delivered by the LHC. ATLAS is made up of several sub-detector systems, as depicted in Figure 3–3.

---

[3] ATLAS stands for "A Toroidal LHC ApparatuS".
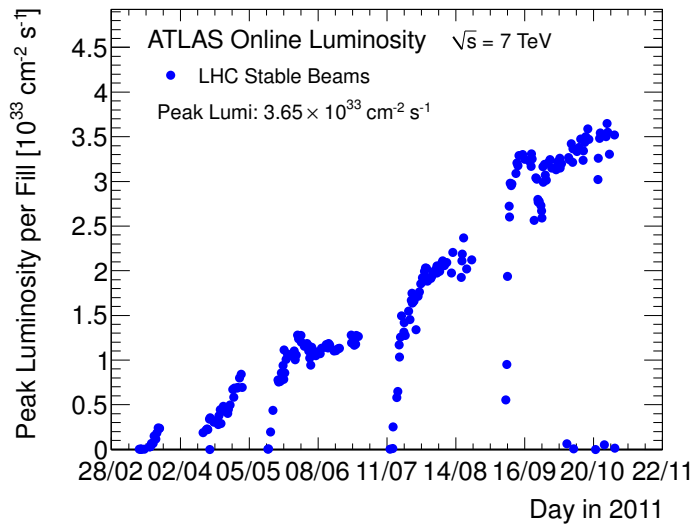
(a)
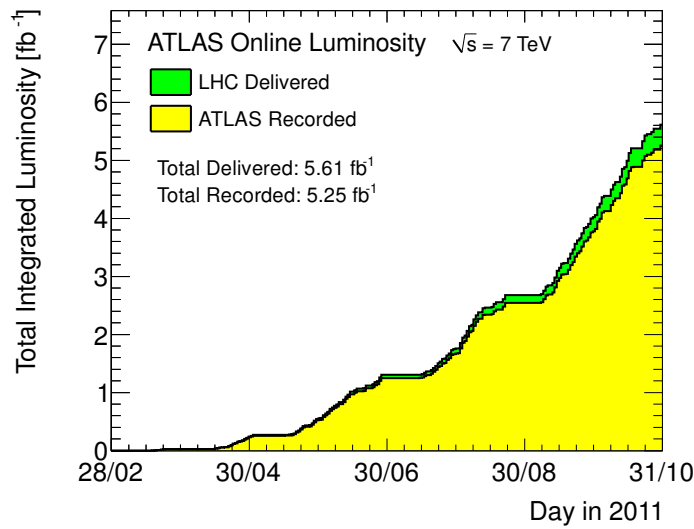
(b)

Figure 3–2: (a) Maximum instantaneous luminosity achieved at the beginning of a data taking period (fill) as function of time [35], and (b) total integrated luminosity delivered by the LHC (green) and recorded by the ATLAS experiment (yellow) as function of time [35].
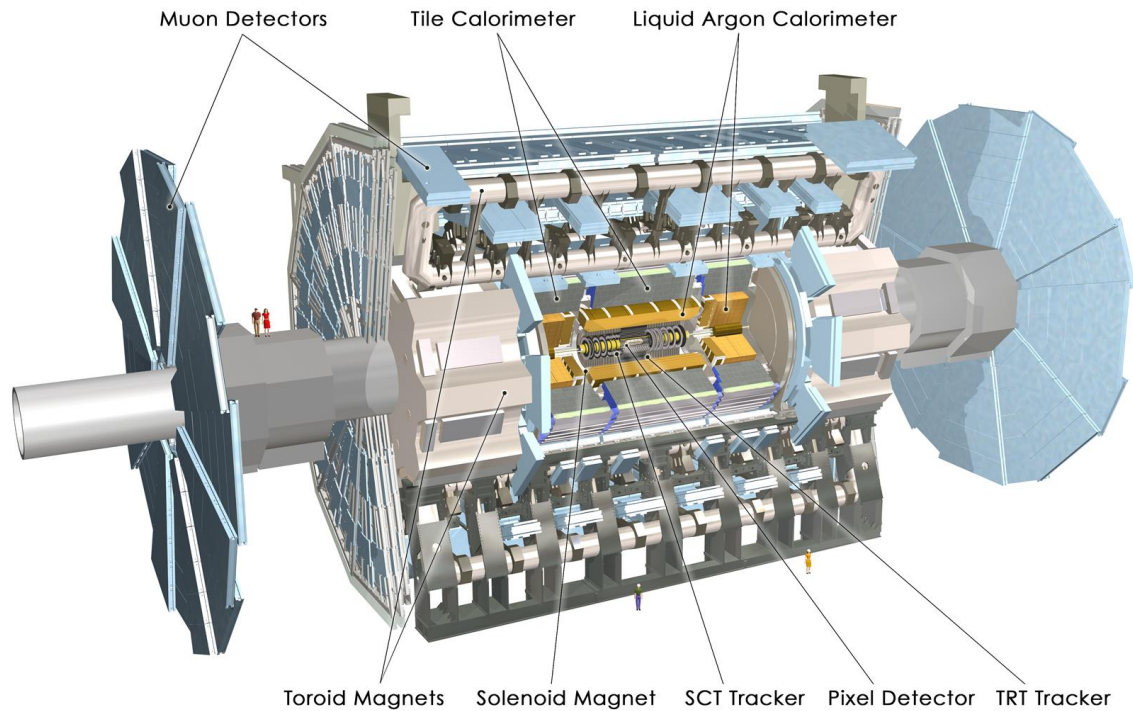
Figure 3–3: Computer generated layout of the ATLAS detector [37]. The TRT and SCT acronyms stand for Transition Radiation Tracker and Semiconductor Tracker, respectively.

ATLAS comprises three main sub-systems arranged in concentric layers centered around the colliding proton beams. Closest to the beam pipe is the Inner Detector whose purpose is to measure precisely the trajectories of charged particles produced in the collisions. The Inner Detector is embedded in a strong solenoidal magnetic field of 2 T, which bends the trajectories of electrically charged particles in order to infer their momenta. Surrounding the Inner Detector are the calorimeters which measure the energy deposited by electrons, photons and hadrons (such as protons, neutrons, light mesons, etc.). The outermost system, by far the biggest component of ATLAS,

27

is the muon spectrometer. Its size comes from the large toroid magnets which bend the trajectories of muons in order to accurately measure their momenta. Figure 3–4 illustrates how different types of particles interact with the different layers of the ATLAS detector. Particles emerging from a collision can therefore be identified based on the different patterns, or "signature", that they leave in the ATLAS detector.
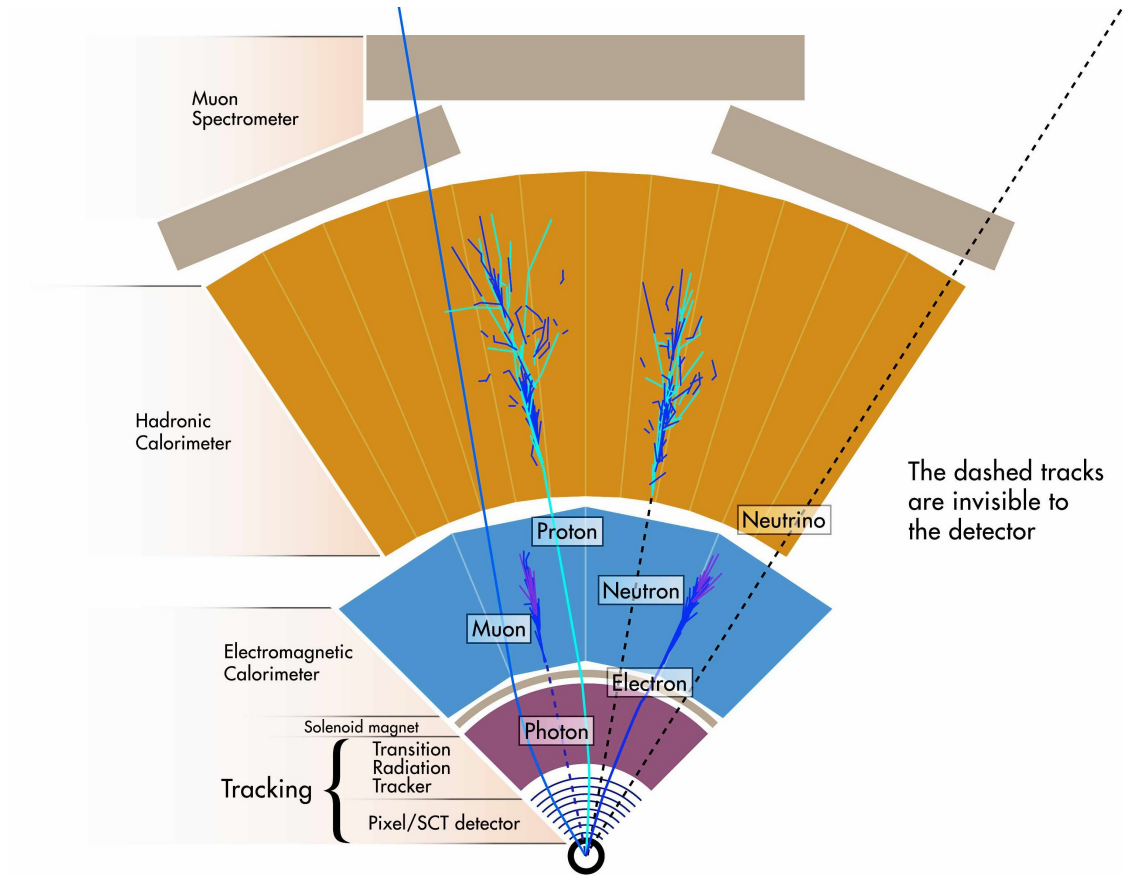
Figure 3–4: Schematic diagram of part of the transversal cross-section of the ATLAS detector showing the different sub-detectors used for particle detection and identification [38]. The colliding beams travel in and out of the page.

The coordinate system and some further conventions that were adopted by the ATLAS experiment will be outlined in the next section. A more detailed description of the main components of the ATLAS detector will follow in the subsequent sections.

3.2.1   Coordinate system

ATLAS uses a right-handed coordinate system where the x-axis points towards the center of the LHC tunnel and the y-axis points upwards. The z-axis thus lies in the direction of the colliding proton beams. The origin $(x, y, z) = (0, 0, 0)$ is taken to be at the geometrical center of the detector where the nominal interaction point is located. At hadron colliders, since the z-component of the momentum of the colliding partons system is unknown, it is convenient to define the detector solid angle in terms of quantities that are (almost) invariant under a longitudinal (i.e. along the z-axis) Lorentz boost. The parametrization is done using the azimuthal angle ϕ, defined in the x-y plane, and the pseudorapidity, defined as $\eta \equiv -\ln[\tan\theta/2]$ where θ is the polar angle (from the z-axis). Pseudorapidity is numerically equivalent to the Lorentz invariant quantity called rapidity[4] at high energy colliders where the mass of particles is typically much smaller than their momentum. As a consequence, the Euclidean distance in pseudorapidity-azimuthal angle space, $(\Delta R)^2 = (\Delta\eta)^2 + (\Delta\phi)^2$, is thus approximately Lorentz boost invariant along the z direction. *Transverse* quantities are also commonly utilized at hadron colliders for the same reason. The transverse

---

[4] The rapidity is defined as $y \equiv \frac{1}{2}\ln\left(E + p_z\right)/\left(E - p_z\right)$. In the limit where $p \gg m$, where p and m are the momentum and mass of a particle, $\eta \to y$.

momentum of particles for instance is defined as $p_{\mathrm{T}} = |\vec{p}\,| \sin\theta = |\vec{p}\,| / \cosh\eta$.

3.2.2   Inner Detector

The ATLAS Inner Detector [36] system is the instrumented volume closest to the beam pipe. Its purpose is to sample spatial points (*hits*) along a charged particle's trajectory, which, when combined, lead to the reconstruction of *tracks*. The longitudinal magnetic field bends the charged particles' trajectory in the ϕ direction. The transverse momentum of charged particles is inferred from the radius of curvature of the bent tracks. The tracking system covers the $|\eta| < 2.5$ region and is composed of three sub-detectors, as illustrated in Figure 3–5.

The innermost sub-system of the Inner Detector is the Pixel detector [36], consisting of three concentric barrel layers (in addition to two end-caps, with three disks each, for higher $|\eta|$ coverage) of silicon pixel modules. Each module contains a 250 μm thick sensor consisting of a two dimensional array of approximately 50 thousand pixels. The fine-grained pixels of 50 μm × 400 μm in size (roughly oriented in the ϕ, z plane) ensure a very precise position measurement. The intrinsic spatial resolution of individual modules in the pixels short pitch (50 μm) direction was measured to be ~ 12 μm at normal incidence [40].

Moving away from the beam pipe, the Semiconductor Tracker (SCT) [36] comes next. It consists of four concentric barrel layers (and nine disks in each of the two end-caps) of silicon-strip modules. Strips on the silicon sensors are aligned along the z-axis in the barrel, with an average pitch of 80 μm. To allow for a z position measurement, two sensors are glued together back-to-back but with a small relative
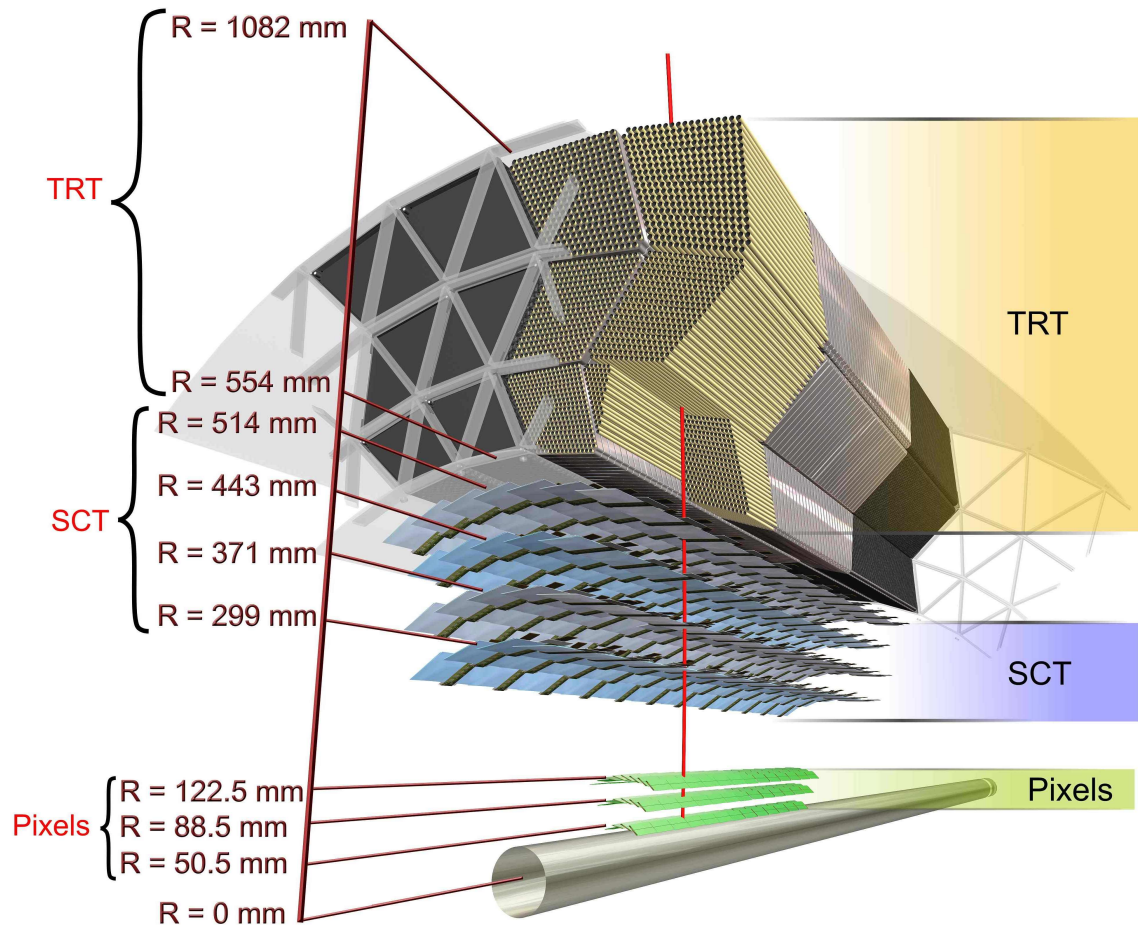
Figure 3–5: Computer generated picture of the ATLAS Inner Detector (barrel sections) [39]. The TRT and SCT acronyms stand for Transition Radiation Tracker and Semiconductor Tracker, respectively.

stereo angle in order to define a segmentation in z through the crossings of the superimposed strips. An incident charged particle will thus typically give rise to eight hits (from the two planes per module times the four layers), yielding four three dimensional spatial points. At normal incidence, the intrinsic spatial resolution of

a single module along the direction perpendicular to the strips was measured to be $\sim 16\ \mu$m [41].

Both silicon-based precision tracking detectors are crucial instruments for the reconstruction of interaction vertices[5] .

The outermost sub-detector of ATLAS's tracking system is the Transition Radiation Tracker (TRT) [36]. The Transition Radiation Tracker spans the largest volume and thus provides a large number of hits necessary for a precise charged particle momentum measurement. It consists of long proportional drift tubes, called straw tubes, that are filled with a Xe-based gas mixture. Each tube is 4 mm in diameter to ensure a small drift time of the ionization electrons and hence obtain a quick signal extraction. The measured relationship between the drift time and the minimum distance of a particle track to the anode wire is used for coordinate measurement. The single straw coordinate measurement resolution was found to be $\sim 130\mu$m [42]. Straw tubes in the barrel are aligned along the z-axis and therefore only provide position measurements in the azimuthal plane. A charged particle with $p_{\mathrm{T}} > 0.5$ GeV will typically traverse 36 straws in the central region of the detector.

The Transition Radiation Tracker owes its name to its ability to detect transition-radiation photons induced by the passage of charged particles. A charged particle will radiate as it traverses the interface between two media with different dielectric properties. Because the intensity of this radiation is proportional to the relativistic gamma

---

[5] A (*primary*) vertex is commonly found at the interaction point of the hard scattering from the pp collision itself. More than one primary vertex can be reconstructed in an event with in-time pileup.

factor ($\gamma = E/m$), lighter particles will tend to emit much more transition-radiation photons than heavier ones, hence providing a means to discriminate electrons from charged hadrons. This phenomenon is provoked in the Transition Radiation Tracker by the insertion of plastic fibres in the interstices of the straw tubes pattern. The emitted transition-radiation photons are absorbed[6] by the gas in the straw tubes and deposit a lot more energy than what is expected from the ionization of the gas by the passage of the incident charged particle. It is possible to tell apart transition-radiation and tracking signals by using two separate energy thresholds (low, high) in the electronic devices that read out the electric signal coming from each straw tube. Using this information, it is therefore possible to discriminate between electrons and charged hadrons.

The tracking system is required to provide a transverse momentum resolution $\sigma_{p_\mathrm{T}}/p_\mathrm{T}$ for charged particles of 0.05% $p_\mathrm{T} \oplus 1\%$ [36], where the symbol $\oplus$ indicates that the two terms are added in quadrature.

3.2.3   Calorimeters

Jets produced in hard scattering collisions typically contain neutral hadrons (among many other types of particles) which cannot be detected by the tracking detectors. Calorimeters, which are used to measure the energy of hadrons in jets, are thus crucial detectors for any jet-related measurements. Unlike both the inner

---

[6] Transition-radiation photons are emitted with an energy of a couple of keV and ionize the gas by means of the photoelectric effect.

detector and the muon spectrometer, the calorimeters measure the energy of particles by means of a destructive process: incident high-energy particles, with the exception of neutrinos and most muons, are "stopped" and "absorbed" by a dense material. It is this deposited energy, or equivalently the energy loss of the incident particles in the material, that is measured by the calorimeters. Because of the different forces that govern the interactions of different types of particles with matter, ATLAS features two distinct calorimeter systems specifically adapted to electromagnetic particles (electrons, photons), and hadrons. The calorimeters are illustrated in Figure 3–6.
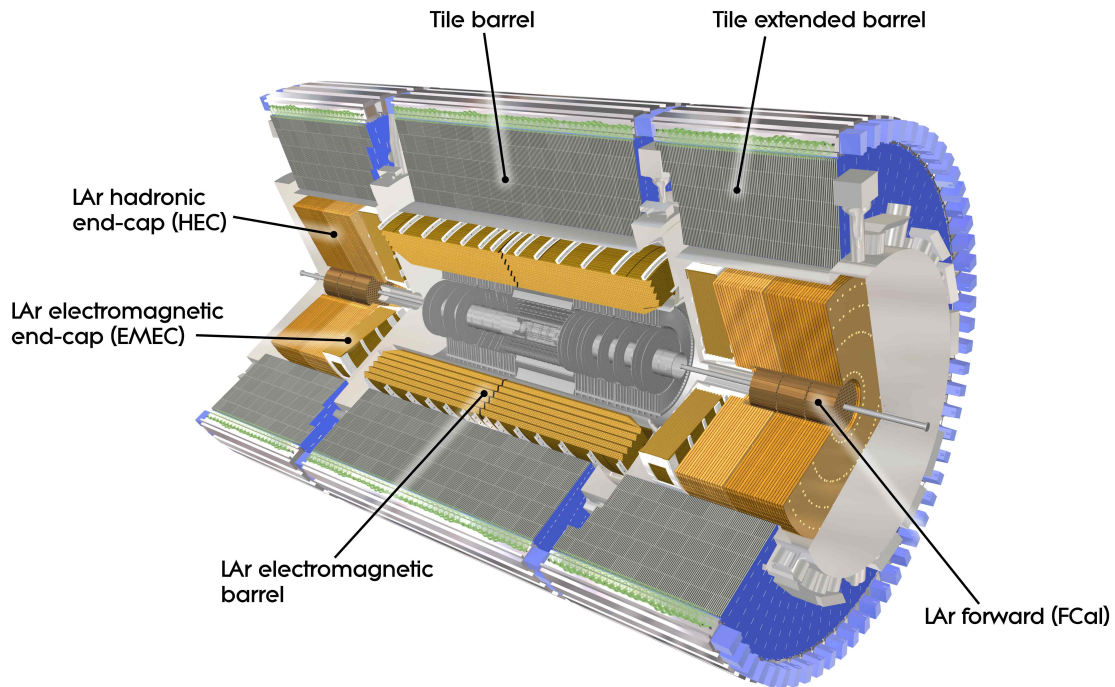
Figure 3–6: Computer generated picture of the ATLAS calorimeters [43]. LAr stands for liquid argon.

3.2.3.1 Electromagnetic Calorimeter

The aim of the electromagnetic calorimeter [36] is to measure the energy of electrons and photons. It consists of successive layers of a passive absorber, lead, and an active medium, liquid argon (LAr) which is kept at low temperatures by means of a cryogenic system (cryostat). Hence, the electromagnetic calorimeter is a *sampling* calorimeter because it measures only a fraction of the total energy deposited. When an incident particle impinges on the calorimeter, it initiates a cascade of electromagnetic processes as it traverses the lead layers (bremsstrahlung, electron-positron pair production), giving rise to an increasing number of secondary particles. Because those particles are produced with ever decreasing energies, this stochastic process eventually comes to a halt, resulting in a finite size electromagnetic *shower* well contained inside the electromagnetic calorimeter. The detection per se occurs when the electrons from this shower ionize the liquid argon. The ionization electrons produced drift in an electric field to reach kapton electrode plates. The signal strength from a liquid argon gap is proportional to the energy deposited in the liquid argon and the total measured energy deposited in all the liquid argon gaps is propotional to the energy of the original incoming particle. The peculiarity of the ATLAS electromagnetic calorimeter is indisputably its accordion shape geometry, which is depicted in Figure 3–7. The alternating electrode and lead plates were folded prior to assembly and provide quick signal extraction at either end of the electrode plates (i.e. towards or away from the interaction point, in the radial direction). This choice also prevents the appearance of dead zones, given that no cables are running
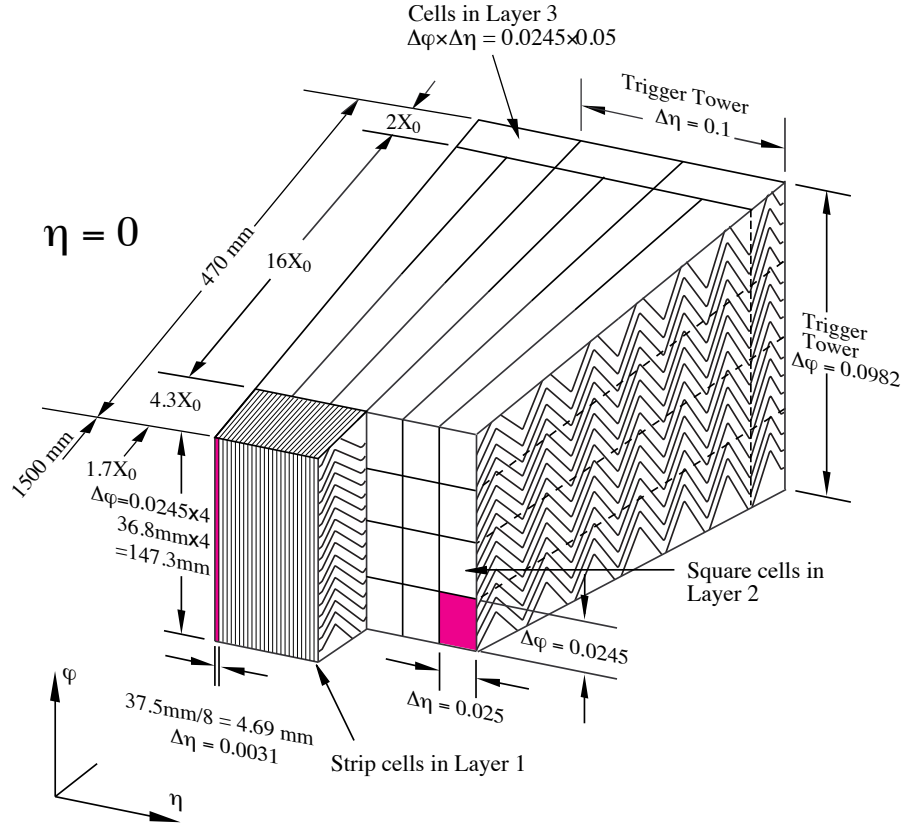
Figure 3–7: Illustration of a section of the ATLAS electromagnetic calorimeter (barrel section, $|\eta| < 1.475$) [36]. At $\eta = 0$, incoming particles are traveling along the radial direction, that is perpendicular to the ϕ and η axes. The interaction point is located on the front side of the module where those axes are drawn in the diagram.

inside the module itself, and provides full coverage in ϕ around the beam axis[7] . The electromagnetic calorimeter furthermore provides position measurements by means of a three-dimensional segmentation. It is segmented into three main sections in

---

[7] If the plates were straight, rather than folded in this accordion shape, incident particles could traverse the liquid argon portions of the calorimeter without crossing the absorber, thus creating *crack* regions in ϕ.

depth (for the barrel) with varying η-ϕ granularity. Etched patterns on the electrodes themselves provide the fine longitudinal (η) segmentation, notably in the first section, necessary for photon/π^0 separation[8] . The azimuthal (ϕ) segmentation, in turn, is achieved by grouping electrodes together. The resulting readout cell sizes can be seen in figure 3–7.

In view of the ATLAS broad physics requirements, the energy resolution σ_E/E of the electromagnetic calorimeter is required to be at most $10\%/\sqrt{E} \oplus 0.7\%$ [36].

3.2.3.2 Hadronic Calorimeter

The very nature of the interactions of hadrons with matter dictates the design choices made for the hadronic calorimeter. Hadrons penetrate deeper in a dense material and initiate (hadronic) showers that are also typically larger in size than electromagnetic showers. As shown in Figure 3–6, the hadronic calorimeter surrounds the electromagnetic one and is also a sampling calorimeter. The electromagnetic calorimeter is *thick* enough to prevent leakage into the hadronic calorimeter when the incident particle is an electron or a photon. An incident hadron, on the other hand, may produce an hadronic shower that begins in the electromagnetic calorimeter but the hadronic cascade will eventually reach the hadronic calorimeter. Here, two different technologies are employed: the barrel ($|\eta| < 1$) and extended-barrel ($0.8 < |\eta| < 1.7$) sections rely on plastic scintillating tiles, whereas the end-cap and forward sections use liquid argon as the active medium.

---

[8] $\pi^0 \rightarrow \gamma\gamma$ produces two close-by *clusters* of energy in the calorimeter, hence the need for good position resolution.
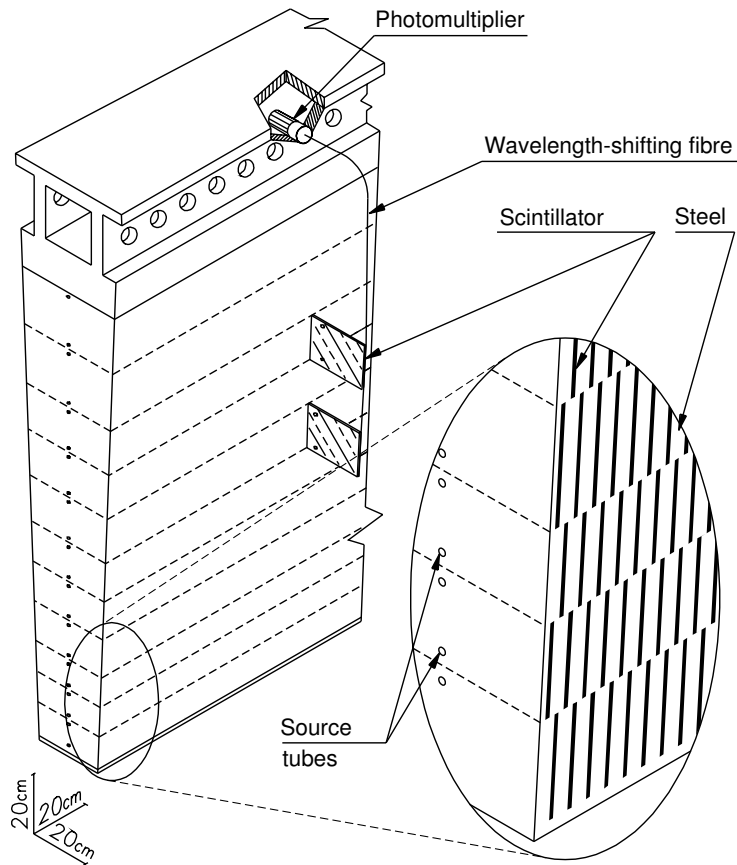
Figure 3–8: Illustration of a section of the ATLAS Tile hadronic calorimeter [36]. The incident particles travel from bottom to top.

Figure 3–8 shows a module of the Tile calorimeter [36]. Alternating plates of steel (absorber) and scintillating tiles are arranged in a perpendicular configuration with respect to the z-axis direction. The tiles are thus staggered in depth to prevent any uninstrumented regions (cracks), and the readout is performed by wavelength shifting fibres fed into photomultiplier tubes. The unconventional orientation of the tiles allows the fibres to adopt a simple straight route to the photomultipliers located at the top of each module by coupling to tiles at both edges in the ϕ direction [44].

The barrel section features 64 such modules positioned around the z-axis, resulting in a ϕ segmentation of ~ 0.1 radian. Readout cells are then defined by grouping together a set of fibres into a photomultiplier tube, giving rise to a longitudinal (through a projective geometry in pseudorapidity) and radial (three layers in depth) segmentation of the calorimeter. A granularity of $\Delta\eta \times \Delta\phi = 0.1(0.2) \times 0.1$ is achieved in the first two (last) layers of the Tile calorimeter. It is this fine granularity of the ATLAS calorimeters that allows for precise jet substructure measurements as described later in this thesis.

ATLAS calorimeters are so-called non-compensating calorimeters as they feature a ratio of the electromagnetic response[9] over the hadronic one that is greater than unity ($e/h > 1$); hadrons will thus have their measured energy systematically under-estimated. This behavior is due to the complex hadronic shower development in which both the electromagnetic and strong forces play a role. Indeed, not only is the fraction of the energy of the hadronic cascade that is purely electromagnetic[10] subject to large fluctuations, but there is a significant portion of undetected energy produced in the hadronic shower. This "invisible" energy is mainly due to nuclear interactions (excitation, breakup of nuclei) for which the binding energy cannot be measured, to the production of low energy neutrons that go undetected and to escaping neutrinos. Although the non-compensating behavior leads in general to a

---

[9] The detector energy response is defined as the ratio of the measured energy of an incident particle to the actual energy of that particle.

[10] That is energy deposited through electromagnetic processes.

worse energy resolution, it can be partly compensated by a calibration procedure performed at the software level.

Both calorimeters are calibrated at the so-called electromagnetic scale, that is calibrating the measured energy by accounting for electromagnetic processes only. Additional calibration procedures are applied at the software level to correct for the non-compensating nature of the calorimeters and restore the true energy scale.

In view of the ATLAS broad physics requirements, the energy resolution σ_E/E of the hadronic calorimeter is required to be at most $50\%/\sqrt{E} \oplus 3\%$ in the barrel region [36].

3.2.4 Muon Spectrometer

Because muons traverse the calorimeters depositing only a small fraction of their energy in the calorimeters, a dedicated detector is required for their identification. The ATLAS muon spectrometer fulfills this purpose [36]. It is located outside the calorimeters, thus within reach of only muons (and neutrinos), and consists of large superconducting toroid magnets (one barrel, two end-caps) and precision tracking measurement units. The trajectory of a muon is bent by the strong magnetic field[11] , therefore providing a means to measure its momentum. In order to avoid disruptive effects on the trajectories of muons, the toroids are made out of an air core instead of a ferromagnetic one. The magnetic field is produced within the core of the toroids

---

[11] The toroid magnetic field strength is of approximately 0.5 T in the barrel, and 1 T in the end-cap regions.

in the ϕ direction. The *bending* plane is thus defined as the plane where the muons are deflected, i.e. in the η direction.

The tracking capabilities of the muon spectrometer is provided by different types of muon *chambers*. Monitored Drift Tube (MDT) chambers [36] are arranged in three concentric layers around the beam pipe in the barrel, and form wheels in the end-cap regions, thus covering most of the tracking range in η. Each Monitored Drift Tube chamber in the barrel is of rectangular shape, a few meters wide, and consists of several layers of narrow ($\sim$ 30 mm in diameter) drift tubes perpendicular to the z-axis and filled with an Argon-based gas mixture. The resulting position resolution in a Monitored Drift Tube chamber is approximately 35 μm (along the z-direction, in the barrel).

ATLAS's muon system is also equipped with special chambers featuring quick signal extraction (of the order of a few tens of nanoseconds), at the expense of a lower position resolution (a few millimeters). These dedicated chambers are used for triggering[12] purposes. In the barrel, Resistive Plate Chambers (RPC) [36] consist of gaseous parallel electrode-plate detectors with orthogonal readout strips providing ϕ and η segmentations. They either sandwich or are located only on the bottom or top of Monitored Drift Tube chambers, depending on the radial layer under consideration. In the end-caps, Thin Gap Chambers (TGC) [36] were assembled in wheel-like structures. Thin Gap Chambers are multi-wire proportional chamber detectors that

---

[12] The trigger system selects in real-time events that are potentially interesting and worth recording for subsequent detailed analysis.

provide tracking measurements in the bending coordinate (η) from the signal induced on the anode wires. Azimuthal segmentation is, in turn, provided by pick-up strips running perpendicular to the wires (i.e. in the radial direction). The fast trigger chambers also complement the precision measurements performed by the Monitored Drift Tube chambers by providing a measurement of the ϕ coordinate of a track.

The muon spectrometer was designed to provide a transverse momentum resolution σ_{p_T}/p_T of 10% for muons with $p_T = 1$ TeV [36].

3.2.5 Trigger

The purpose of the ATLAS trigger system [36] is to select in real-time a subset of all the proton-proton collision events that will be recorded for subsequent detailed analyses. An event is considered potentially interesting, and thus worthy of being recorded, if it contains patterns left in the detector that are specific to energetic jets or leptons. Only $\mathcal{O}(100)$ out of ~ 40 millions events to be delivered by the LHC machine every second at designed operating parameters are selected by the trigger system.

The ATLAS trigger system consists of three distinct and successive levels of event selection where more stringent requirements are applied at each subsequent level.

The first trigger level, called Level-1 (L1), makes use of dedicated custom electronics and is entirely hardware-based. It was designed to reduce the event rate from ~ 40 MHz down to 75 kHz, with a maximum single-event processing time of 2.5 μs. In order to achieve such stringent requirements, the L1 calorimeter trigger

system, for instance, reconstructs jets using information from the calorimeter at a reduced granularity. The reconstructed jets which are above a given transverse energy threshold define so-called *regions of interest* (RoI) that are passed on to and further investigated by the second trigger level.

The Level-2 (L2) trigger system is software-based. Thanks to the rate reduction provided by the upstream L1 trigger, it can use the full granularity information of the different sub-detectors, within the previously identified RoI's, in order to more accurately identify potential physics signatures. The per-event processing time is on average a few tens of milliseconds. The event rate must be reduced by a factor of about 20 with respect to the L1 output rate, as to reach approximately 3.5 kHz. Relatively simple but very fast reconstruction algorithms are used at L2. If the L1 decision is confirmed, the event makes its way to the final step of the selection process.

The third level, referred to as the Event Filter (EF) is also software-based. It is designed to reduce the event rate received from the L2 down to 200-300 Hz. Unlike the L2, the EF has a few seconds to process an event. It can thus use the full granularity information of the sub-detectors over the entire detector[13] and can utilize the most refined reconstruction algorithms provided by ATLAS.

---

[13] That is to say, without the need to be restricted to the identified RoI's.

3.3 Datasets

The data sample used for the present analysis consists of proton-proton collisions delivered by the LHC at $\sqrt{s} = 7$ TeV and recorded by the ATLAS detector during the year 2011. The data collected amount to a total integrated luminosity of 4.6 ± 0.2 fb^{-1}.

Samples of Monte Carlo (MC) simulated events are used to predict the expected background that can be accounted for by the Standard Model. MC samples are also used to model hypothetical $t\bar{t}$ resonance signals, namely heavy Z' bosons and g_{KK} gluons. The Standard Model predicts the total expected background to be made of contributions from many different processes. Several MC samples were thus generated for each of those processes provided that their relative contribution to the analysis exceeds the sub-percent level.

The MC samples were passed through a GEANT4-based simulation [45] of the ATLAS detector [46]. The GEANT4 program simulates the interactions between particles and matter, in this case, the ATLAS detector. The experimental signatures were reconstructed using the exact same algorithms and analysis software as used to analyze real data events. Some physics quantities (such as the measured lepton energy scale and identification efficiencies) in Monte Carlo simulated events are corrected to match what is measured in actual data to compensate for small differences (~ 1 % or less).

A large number of proton-proton collisions were simulated using various MC event generators and parton showering, hadronisation and underlying event[14] models. Table 3–1 summarizes the samples of Monte Carlo simulated events, as well as their respective configuration, for the different processes relevant to this analysis.

---

[14] The underlying event consists of all processes taking place in a proton-proton collision apart from the hard scattering interaction itself. It mainly consists of beam remnants, initial state radiations and multiple-parton interactions.

Process	Event Generator	Parton Shower/Hadronisation & Underlying Event	PDF Set	Effective luminosity (fb^{-1})
$pp \to t\bar{t}$	MC@NLO [47]	Herwig + Jimmy [48, 49]	CT10 [50]	130
$pp \to W + \text{jets}$	Alpgen [51]	Herwig + Jimmy	CTEQ6L1 [52]	10
$pp \to Z + \text{jets}$	Alpgen	Herwig + Jimmy	CTEQ6L1	50
$pp \to tb$	MC@NLO	Herwig + Jimmy	CT10 [50]	600
$pp \to tW$	MC@NLO	Herwig + Jimmy	CT10	50
$pp \to tq(b)$	AcerMC [53]	Pythia [54]	CTEQ6L1	120
$pp \to qq'$	Pythia	Pythia	MRST LO* [55]	4
$pp \to WW/ZZ/WZ$	Herwig	Herwig + Jimmy	MRST LO*	200

Table 3–1: Summary of event generators, simulation software, parton distribution function (PDF) sets and the approximate sample effective luminosity used to simulate the dominant Standard Model processes for the analysis presented in this thesis.

For each of the physics processes relevant for this analysis, the shapes of the distributions are directly obtained from the samples of Monte Carlo simulated events. Each sample is normalized to the predicted cross-section of its corresponding physics process. The total expected background is thus obtained from the sum of these properly normalized Monte Carlo samples.

The $t\bar{t}$ sample (the dominant background process in the analysis) is normalized to the cross-section calculated at approximate NNLO (next-to-next-to-leading-order) in perturbative QCD [56]. Being an important contribution to the total expected background for this analysis, the $t\bar{t}$ sample has to provide a good description of the data. An event generator that incorporates next-to-leading-order (in perturbative QCD) corrections was thus chosen over a *tree-level* generator in order to improve the predictions of the shape of the distributions.

The overall normalization of the sample of the direct production of W bosons decaying to an electron ($W \to e\nu_e$) or a muon ($W \to \mu\nu_\mu$), in association with jets, is set to the W production cross-section (times branching ratio) calculated at NNLO [57]. Positively charged W bosons are produced more abundantly than negatively charged ones in proton-proton collisions because of the dominance of u quarks in the proton. The predicted ratio of the W^+ to W^- boson cross-sections is better understood, from a theoretical standpoint, than the inclusive $W + \text{jets}$ cross-section [58]. This ratio, extracted from Monte Carlo simulation, together with the difference between the number of data events with a positively charged lepton and a negatively charged one, can then be used to infer the total number of $W + \text{jets}$ events observed

in data. Correction to the $W + $ jets sample normalization were calculated in [59] using this observed charge asymmetry and are applied here.

The remaining samples from other Standard Model processes[15] are normalized to their respective cross-sections calculated in perturbative QCD at LO (multi-jet using PYTHIA), NLO (dibosons [60]) and NNLO (single top [61, 62, 63], W/Z production [57]).

The $Z' \to t\bar{t}$ signal samples were generated using PYTHIA [54] (event generation, parton showering and hadronisation) as sequential Z' bosons[16] and are used to model the leptophobic Z' boson of the Topcolor model. A Z' MC sample consists of ~ 100 thousand events generated at a fixed Z' (pole) mass. Several samples were generated at different mass values, namely $m_{Z'} = 0.8$, 1.0, 1.3, 1.6, 2.0 and 2.5 TeV (only 20 thousand events were generated for $m_{Z'} = 2.5$ TeV). The predicted Leptophobic Z' production cross-section times branching ratio for different values of mass (to which the samples are normalized) are calculated at leading-order in QCD [27, 28]. Predicted values of the cross-section are multiplied by 1.3 to account for next-to-leading order QCD corrections [64].

---

[15] These samples consist of the direct Z boson production in association with jets, W+jets production with the W decaying to a τ lepton, single top production, diboson ($WW/ZZ/WZ$) production and multi-jet production.

[16] The couplings to fermions of the Z' are identical to those of the Standard Model Z boson. This results in a Z' width of approximately 3% of its mass which is comparable with the leptophobic Topcolor Z' width of 1.2%. The difference in width at the percent level is indistinguishable experimentally because of detector effects.

The Randall-Sundrum Kaluza Klein gluon $g_{KK} \to t\bar{t}$ signal samples were generated using MADGRAPH (event generation) [65] and PYTHIA (parton showering, hadronisation). The g_{KK} MC samples contain 20 thousand events and were generated at $m_{g_{KK}} = 0.8, 0.9, 1.0, 1.15, 1.3, 1.6, 1.8$ and 2.0 TeV. The predicted g_{KK} production cross-section times branching ratio for different values of mass (to which the samples are normalized) are also calculated at leading-order in QCD [30].

CHAPTER 4
Event reconstruction

Experimental signatures expected from jets, leptons and neutrinos produced in proton-proton collisions are reconstructed from raw ATLAS detector data using different software algorithms. This chapter presents an overview of the reconstruction of experimental signatures relevant for the identification of events consistent with the production of a top and antitop quark decaying to a lepton+jets final state.

4.1 Electrons

The experimental signature of an electron in the ATLAS detector is a track in the Inner Detector and a localized energy deposit in the electromagnetic calorimeter.

The electromagnetic shower induced by the passage of an electron in the calorimeter is reconstructed as a cluster of cells with measured energy above a certain threshold in the electromagnetic (EM) calorimeter. This EM cluster is identified using a sliding window algorithm that operates on a grid consisting of square elements in the $\eta - \phi$ plane. The amount of energy deposited in each of those elements is obtained by summing all the cells in the different radial layers of the EM calorimeter, into what is referred to as a "tower". The cluster energy is corrected for small energy losses due notably to potential leakage of the electron shower outside the cluster's geometrical definition.

Within the tracking volume ($|\eta| < 2.5$), reconstructed tracks in the Inner Detector are then extrapolated from their outward-most hit to the second layer of the EM calorimeter, where most of the energy from electrons is expected to be deposited. EM clusters are then required to be matched in $\eta-\phi$ space to an extrapolated track's impact point on the surface of this second layer, in order for an electron candidate to be successfully reconstructed.

The energy of the reconstructed electron candidate is taken as the measured EM cluster energy and its direction (in $\eta-\phi$ space) is given by the matched track direction as measured at the track's associated vertex. The fractional energy resolution of reconstructed electrons is less than 2% in the central region of the detector [36, 66].

In order to reduce the number of charged mesons wrongly identified as electron candidates, additional requirements are applied [66]. A candidate electron is required to have a distribution of the energy (shower shape) in the EM cluster that is compatible with that of a real electron, with very small leakage in the hadronic calorimeter. The matched track must also satisfy some quality requirements such as having hits in both the pixel and the silicon tracker detectors, while having a measured momentum that is comparable to the EM cluster's total measured energy. Lastly, a high ratio of "high-threshold" hits to the total number of hits in the Transition Radiation Tracker is required to select charged particles having produced a significant number

of transition radiation photons[1] .

4.2 Muons

Unlike electrons, energetic muons deposit only a small amount of energy (a few GeV), through ionization, in the calorimeters. Raw data from the Inner Detector and Muon Spectrometer are instead used to reconstruct and identify muons.

Because of its large volume, the reconstruction of tracks in the Muon Spectrometer is divided into two steps. The first step consists of identifying segments (i.e. straight lines) in each muon station[2] where hits were recorded. Segments from the outer-most stations are then extrapolated back through the magnetic field towards segments found in the middle and inner muon stations. A track candidate is then reconstructed from those matched segments.

A muon will also produce hits in the Inner Detector. Tracks reconstructed in the Inner Detector are geometrically matched to tracks reconstructed in the Muon Spectrometer. With a successful match, an extended reconstructed track is obtained using all hits, from both the original tracks in the Inner Detector and Muon Spectrometer detectors, by finding the trajectory that can be best fitted to those hits. This leads to the reconstruction of a so-called *combined* muon. The combined muon

---

[1] This ratio of high-threshold hits to the total number of hits is of the order of 20% for real electrons, whereas it is $\sim$ 5% for pions.

[2] A muon station in the barrel region corresponds to a Monitored Drift Tube chamber with one or two Resistive Plate chambers.

momentum is calculated from the curvature of the reconstructed track, and is corrected for the small energy losses in the calorimeters. The transverse momentum resolution of a combined muon with $p_\mathrm{T} = 100$ GeV ($p_\mathrm{T} = 10$ GeV) is typically $\sim 3\%$ ($\sim 2\%$). This is $\sim 10\%$ ($\sim 50\%$) better than the resolution of a muon reconstructed only on the basis of hits in the Muon Spectrometer [36].

4.3 Jets

Jets, which are produced as a result of the hadronisation of partons, give rise to a copious amount of hadrons that will deposit a significant fraction of their energy in the hadronic calorimeter. Jets are reconstructed from those energy deposits in the electromagnetic and hadronic calorimeters. Because an incident particle will produce a shower that spans many calorimeter cells, it is first necessary to group neighboring cells together to form clusters which can then be fed as input to a jet reconstruction algorithm.

4.3.1 Topological cell clustering

The cell clustering algorithm, unique to ATLAS, is known as topological clustering [67]. It aims at grouping into clusters close-by calorimeter cells which have a significant amount of measured energy[3] with respect to the expected electronic and pile-up noise present in the calorimeters.

---

[3] The measured energy of both hadronic and electromagnetic calorimeters cells is initially calibrated at the electromagnetic scale [68, 69]. That is to say, the measured energy is calibrated to the response of electrons and photons.

The topological clustering is performed in two steps. First, clusters are formed using *seed* cells whose energy, in absolute value, is at least four times greater than the expected total noise[4] in a given region of the calorimeter. All (immediate) neighboring cells, in both $\eta - \phi$ and adjacent calorimeter layers, are then added to the seed cell, irrespective of their energies. The cluster is allowed to further expand if any neighboring cell has an absolute value of its energy that is greater than twice the expected total noise. In such a case, the cells adjacent to this cell are also added to the cluster. The expansion procedure is repeated iteratively until all neighboring cells of the formed cluster have a measured energy below the threshold (i.e. twice the total noise).

To limit the growth of clusters, the second and final step consists of "splitting" individual clusters so that each final cluster exhibits only a single local energy maximum. The final topological clusters are therefore three dimensional reconstructed "blobs" of energy deposited in the calorimeter representative of the shower induced by a single incident particle.

Before being passed on to a jet reconstruction algorithm, topological clusters are calibrated on an individual basis, a procedure known as local calibration [70]. The purpose of this calibration is to increase the cluster's measured energy to compensate for the lower hadronic response of the calorimeters. The method relies on cluster shower shape variables to classify clusters into two categories: clusters consistent

---

[4] The "total noise" consists of the electronic noise and expected mean energy deposited by pile-up added in quadrature. The electronic noise is defined as the root mean square of the readout electronics noise.

with the shape expected from an electromagnetic shower, and clusters consistent with the shape expected from a hadronic shower. The calibrated measured energy of hadron-like clusters is then obtained by weighting[5] the individual calorimeter cells that belong to the cluster. The weighted sum of the cells' energies corresponds to the cluster's calibrated energy. The energy of topological clusters is further corrected for leakage outside the cluster's geometrical definition and for energy losses due to non-instrumented regions of the detector. The four-momentum of a topological cluster is obtained using the $\eta - \phi$ position of the cluster, its calibrated energy and assuming a mass of zero.

The four-momenta of all calibrated topological clusters are then used as input to a jet reconstruction algorithm.

4.3.2   Jet reconstruction algorithm

Jets are not uniquely defined; it is the choice of a well-behaved prescription (the jet reconstruction algorithm) that provides a coherent picture for experimental measurements and theoretical calculations. Most modern jet algorithms used at hadron colliders fall into the category of sequential recombination algorithms. They work by sequentially adding the four-momenta of close-by reconstructed topological clusters if they are deemed close enough according to a specific proximity measure. The distance measures for some popular sequential recombination algorithms used at hadron colliders can be generalized as:

---

[5] The weights are obtained from Monte Carlo simulations of the calorimeter response of single charged pions.

$$d_{ij} = \min\left(p_{Ti}^{2\rho}, p_{Tj}^{2\rho}\right) \frac{(\Delta R_{ij})^2}{R^2}, \tag{4.1a}$$

$$d_{ib} = p_{Ti}^{2\rho} \tag{4.1b}$$

where p_{Ti} is the transverse momentum of the ith particle and ΔR_{ij} is the Euclidean distance in rapidity-azimuthal angle-space between the ith and j^{th} particles. The quantity d_{ij} is thus the momentum weighted distance between particles i and j. The quantity d_{ib} is to be interpreted as the distance between particle i and the beam. The fixed parameter R is often referred to as the jet size parameter and dictates how far (geometrically) a jet can reach for its constituent particles. The (integer) ρ parameter defines the different flavors of algorithms.

Two particles are added together if the distance d_{ij} between them is the smallest among all other pair-wise combinations in the event as well as if its value is smaller than all d_{ib} values. A final reconstructed jet is formed whenever its d_{ib} value is the smallest among all other d_{ib} and d_{ij} values.

Two jet algorithms are used in the present work: the anti-k_t algorithm [71] ($\rho = -1$) and the k_t algorithm [72] ($\rho = +1$). With the anti-k_t algorithm, high-p_T particles are combined with low-p_T particles present in their surrounding in the early stages of the clustering process. The k_t algorithm, on the other hand, tends to cluster together low-p_T particles first. The anti-k_t algorithm yields jets with more predictable geometrical properties than those obtained using the k_t algorithm which makes them easier to calibrate. Anti-k_t jets are furthermore less likely to contain extra topological clusters arising from the pile-up contamination of the event. For these reasons, the anti-k_t algorithm was chosen to reconstruct jets. The k_t algorithm,

56

however, will be employed to study the internal structure of jets as detailed in the next sections.

The choice of the jet size parameter R has non-trivial implications and is driven by the kinematic properties of the top quark hadronic decay. When a top quark is produced at rest, its three-pronged hadronic decay ($t \rightarrow bW \rightarrow bq'\bar{q}$) gives rise to three spatially separated collimated spray of particles. However, when a top quark is produced with sufficient momentum, its decay products become collimated in the laboratory frame by virtue of the Lorentz boost. It is thus much more difficult for the jet algorithm to correctly resolve (individually) the three decay products of a *boosted* top quark than it is for a top quark produced with a small amount of transverse momentum. The majority of top quarks produced in the decay of (hypothetical) heavy resonances are expected to be boosted[6] . Hence, novel reconstruction techniques specifically tailored to the identification of the decay products of boosted top quarks are required. The method used in the present work involves the use of so-called large-R jets, that is jets reconstructed with a large jet size parameter of $R = 1.0$. The explicit assumption is that all the decay products of the boosted top quark can be clustered into a single jet. With this approach, a boosted hadronically decaying top quark is thus simply reconstructed as one anti-k_t $R = 1.0$ jet.

The reconstructed jet four-momentum is defined as the four-momentum sum of all its constituents (here, topological clusters). The constituents are corrected,

---

[6] The top quarks are produced with a momentum much higher than their mass.

prior to performing the sum, for the position (along the z-axis) of the hard scattering interaction by adjusting their origin[7] to the location of the most significant reconstructed primary vertex in the event[8] .

4.3.3   Jet trimming

Due to its large geometrical size in $\eta - \phi$ space, a non-negligible fraction of a measured large-R jet energy consists of contributions from the underlying event (initial state radiations, multiple parton interactions within a single proton-proton collision, beam remnants) and pile-up (additional simultaneous collisions occurring in the current bunch crossing) effects. The following paragraph describes the technique used to approximately remove such contributions from reconstructed jets, thereby improving the resolution of jet kinematic properties.

The procedure, referred to as jet *grooming*, consists of removing, after the fact, low energy constituents in a jet. Several grooming algorithms exists. They differ from each other by the way possibly irrelevant constituents of a jet are identified and then removed to improve the overall jet energy resolution. Among these algorithms, trimming [74] offers a simple yet robust solution to mitigate the effect of underlying event and pile-up. The algorithmic procedure for trimming goes as follows:

---

[7] By default, the origin is assumed to be the geometrical center of the detector.

[8] Primary vertices are reconstructed by determining locations along the z-axis where more than one reconstructed track is likely to originate from [73]. The most significant vertex is the one which has the highest sum of the squared p_T values of its associated tracks.

1. Reconstruct jets using all topological clusters in the event, with the anti-k_t $R = 1.0$ algorithm. These jets are referred to as the *initial* jets or *un-groomed* jets.

2. For each initial jet, recluster its constituents into sub-jets using a smaller size parameter $R_{\mathrm{sub}} < R = 1.0$.

3. For each initial jet, discard sub-jets if $p_{\mathrm{T}i}/\Lambda_{\mathrm{hard}} < f_{\mathrm{cut}}$, where $p_{\mathrm{T}i}$ is the p_{T} of the ith sub-jet, Λ_{hard} is some scale representative of the kinematics of the event, and f_{cut} is a fixed dimensionless parameter.

4. Finally, for each initial jet, add together the remaining sub-jets into what is now a *trimmed* jet.

In this procedure, some choices are made concerning the sub-jet definition, the Λ_{hard} scale and the f_{cut} parameter. Here, the reclustering in step 2 is performed using the k_t jet reconstruction algorithm because of its ability to equally share the energy among sub-jets. The scale, defined by Λ_{hard}, is chosen to be the initial jet's p_{T} allowing the procedure to dynamically adapt itself on a jet-by-jet basis. Figure 4–1 illustrates the trimming procedure. The choice of R_{sub} and f_{cut} parameters is also driven by the experimental context. In a high pile-up environment, it has been shown that a R_{sub} value of 0.3 and an f_{cut} value of 5% results in trimmed jets whose kinematic properties are largely independent of pile-up contamination while preserving the intrinsic kinematic properties of jets [75]. These values are used in this analysis.
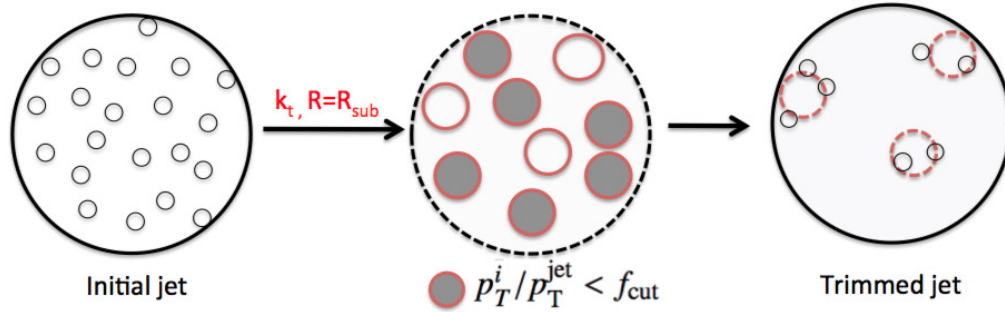
Figure 4–1: Schematic diagram illustrating the different steps of the trimming procedure described in the text. The bigger circle represents an area in the detector in $\eta - \phi$ space covered by the jet. The smallest circles represent individual topological clusters. The red circles represent sub-jets identified by the k_t algorithm.

4.3.4 Jet calibration

A final calibration is applied to the reconstructed trimmed jets in order to restore, on average, the "true" jet energy and mass[9] scales [75]. The corrections are derived, using Monte Carlo simulations, from the calorimeter's response to the true jet energy and mass. These corrections are calculated as a function of the measured energy and η position of a jet. The true jet energy and mass are obtained by reconstructing jets (using the same anti-k_t algorithm) from the four-momenta of the simulated particles themselves[10] .

Jets used in this analysis are therefore reconstructed with the anti-k_t R=1.0 algorithm with the trimming procedure previously described applied, and are fully

---

[9] The jet mass is defined as the invariant mass computed using the reconstructed jet four-momentum. It will be discussed in more detail in Section 5.4.1.

[10] Only stable particles with a lifetime of at least 10 ps, so that they can eventually reach the calorimeters, are considered, excluding neutrinos and muons.

calibrated.

4.4 Missing Transverse Energy

The colliding partons have, to a good approximation, no total transverse momentum, although they can have a significant (and unknown) longitudinal momentum component (i.e. along the z-axis). Since neutrinos are not detected in the ATLAS detector, their experimental signature is thus a measured missing transverse energy (E_T^{miss}). This quantity is defined as the momentum vector that would need to be added to the vectorial sum of all the detected particle momenta, in order for the total transverse momentum to be null. Thanks to the good hermetic coverage of the ATLAS detector, the E_T^{miss} reconstruction can be performed using energy deposited in the calorimeters and reconstructed muons in the muon spectrometer [76].

The calorimeter contribution is calculated from cells belonging to topological clusters[11] by summing energies in both the x and y directions[12] , individually. To further improve the resolution of the measured E_T^{miss}, the cell energies are calibrated according to reconstructed physics objects (e.g. electrons, jets) with which they geometrically overlap (if any) [76].

Finally, the transverse momenta of reconstructed muons are added to the vectorial sum. The missing energy in the x and y directions is then defined as the negative

---

[11] So that the noise contribution to the measured E_T^{miss} can be mitigated.

[12] The energy in the x direction is defined as $E_x = E \sin\theta \cos\phi$, and in the y direction as $E_y = E \sin\theta \sin\phi$, where θ and ϕ are the polar and azimuthal angles, respectively.

of the total detected energy in both directions, and the quantity $E_{\mathrm{T}}^{\mathrm{miss}}$ is calculated as the sum in quadrature of these two quantities.

CHAPTER 5
Event selection

This chapter presents the criteria used to select experimental signatures compatible with the production of a top-antitop quark pair decaying to a semi-leptonic final state ($t\bar{t} \rightarrow WbWb \rightarrow l\nu_l bq'\bar{q}b$, where $l = e, \mu$). In particular, a leptonically decaying top quark is identified based on the presence of an energetic lepton in the vicinity of a reconstructed jet. The decay products of a boosted top quark that decays hadronically are identified using a dedicated identification algorithm exploiting properties of the internal structure of the reconstructed top jet candidate.

The full set of criteria, which are detailed in this chapter, allows to select events in which a top-antitop quark pair was produced with a large invariant mass, with a minimal amount of contamination from background processes.

5.1 Preselection

Events selected for this analysis satisfy a number of quality requirements. Data events must have been recorded when the colliding proton beams were stabilized for normal operating conditions, and with all ATLAS sub-detectors activated and fully operational. Events are also rejected if severe noise bursts were present in the liquid argon calorimeters. Furthermore, events that contain reconstructed jets that

are not associated with measured energy coming from proton-proton collisions[1] are discarded [77]. Finally, at least one reconstructed vertex, with a minimum of five associated reconstructed tracks, must be found in each event in order to guarantee the presence of a hard scattering [73].

5.2 Trigger selection

Events in the analyzed data sample were recorded using a jet trigger that was specifically developed for this analysis. This jet trigger is defined by a different selection criterion applied at each one of the three trigger levels as described below.

Jets are reconstructed by the Level-1 trigger system using reduced calorimeter information. A primitive sliding window (in $\eta - \phi$ space) algorithm is used to locate local transverse energy maxima that will correspond to Level-1 jets. For the event to be passed on to the Level-2 trigger system, a jet with more than 75 GeV of transverse energy must be reconstructed by the Level-1 algorithm.

At Level-2, a more refined jet reconstruction algorithm is employed using the full calorimeter data around the jet candidates previously identified at Level-1. An iterative algorithm is then used to refine the $\eta - \phi$ position and the E_{T} of the jet such that the amount of energy in a circular region (with a radius of $R = 0.4$) is maximized. Only three iterations are performed due to time constraints. The event

---

[1] Sources of such "fake" measured energy in the calorimeter can come from detector defects or cosmic-rays for instance.

will be analyzed by the Event Filter if it contains at least one jet with transverse energy of at least 95 GeV at Level-2.

Finally, at the Event Filter, the full calorimeter information can be exploited over the entire detector. Thanks to the event rate reduction provided by the two previous levels, topological clusters can be reconstructed and used as input to the jet algorithm. A large-R (using $R = 1.0$) jet with transverse energy of at least 240 GeV must be reconstructed with the anti-k_t algorithm at the Event Filter.

The transverse energy thresholds applied at each trigger level are at the so-called electromagnetic energy scale, that is prior to applying any hadronic calibration. For this analysis, only events that satisfied all three selection criteria as described above were recorded and are analyzed here.

Figure 5–1 shows the trigger efficiency in events satisfying the basic object selection (minus the jet high-p_T selection) presented in the next section. The dotted line corresponds to the region (jet $p_\mathrm{T} > 350$ GeV) where the trigger is considered to be fully efficient.

5.3   Object selection

In order to select events compatible with the production of a top-antitop quark pair decaying to a semi-leptonic final state, events are required to satisfy the following criteria:

- At least one reconstructed electron with $E_\mathrm{T} > 25$ GeV and $|\eta| < 2.47$, excluding a crack region at the boundary of calorimeters ($1.37 < |\eta| < 1.52$), or

  at least one reconstructed muon with $p_\mathrm{T} > 20$ GeV and $|\eta| < 2.5$.
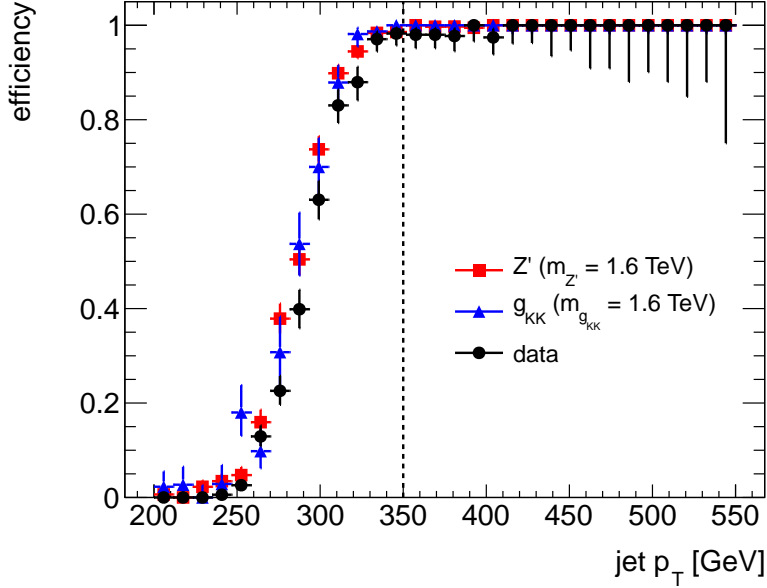
Figure 5–1: Efficiency of the jet trigger as a function of the leading *offline* reconstructed jet p_T. The offline jet is calibrated at the hadronic scale, whereas the trigger thresholds at all three levels are determined at the electromagnetic scale. The efficiency for signal (red and blue markers) is calculated from Monte Carlo samples. The efficiency in data (black markers) is estimated using events satisfying another jet trigger with looser requirements (i.e. a threshold at the Event Filter of 100 GeV at the electromagnetic scale using anti-k_t $R = 0.4$).

- $E_T^{\text{miss}} > 20$ GeV.

- At least 2 reconstructed large-R jets (using trimming) with $p_T > 100$ GeV, where one further has $p_T > 350$ GeV in order to ensure that the trigger selection is fully efficient.

Events selected at this point in the analysis predominantly come from the reactions $pp \to$ jets (multi-jet events), $pp \to W + \text{jets} \to e\nu_e/\mu\nu_\mu + \text{jets}$ (W + jets events) and $pp \to t\bar{t} \to WbWb \to e\nu_e bq'\bar{q}b/\mu\nu_\mu bq'\bar{q}b$ ($t\bar{t}$ production from the Standard Model). The latter is a so-called irreducible background because it exhibits the

exact same final state as signal ($t\bar{t}$ pairs from the decay of a Z' or a g_{KK}). Multi-jet and W + jets events are reducible backgrounds in which no top quarks are produced. These (reducible) background events can be in large part rejected by requiring that the kinematic properties of the reconstructed jets and lepton be consistent with a leptonic and a hadronic top quark decay. This refined selection is done by dedicated top quark identification algorithms, *tagging* algorithms, which will be outlined in the following section.

5.4   Top quark identification

In this analysis, a set of criteria is defined and used to select events containing both a jet and lepton consistent with a leptonic top decay, and a single jet consistent with a hadronic top decay. These selection criteria were developed based on Monte Carlo simulations of background and signal events only, that is to say without looking at the actual data distributions.

The internal structure (or *substructure*) of the reconstructed jets is exploited in order to identify boosted hadronic top decays ($t \rightarrow Wb \rightarrow bq'\bar{q}$). The top quark mass as well as the presence of a hadronic W decay inside the jet are the main features on which the hadronic top selection depends.

The identification of leptonic top decays ($t \rightarrow Wb \rightarrow bl\nu_l$) relies on distinctive kinematic properties of the jet initiated by the b-quark, and the lepton from the W boson decay. Correlations between the jet and lepton energies, and the amount of energy surrounding the lepton are notably utilized in the leptonic top selection.

Although mostly relevant for the hadronic top selection, some jet substructure techniques are also of interest for the leptonic top selection, notably when the lepton is an electron whose energy is included in the reconstructed jet energy.

Before describing in more details the top tagging algorithms and their performance, the different jet substructure observables used herein will first be presented.

5.4.1   Jet substructure

Jet mass

The most natural discriminating observable a hadronically decaying boosted top quark can offer is its mass. A single jet which contains all the final decay products of a top quark will tend to have an invariant mass that is numerically close to the top mass value (≈ 173 GeV) [1] thanks to conservation of four-momentum. The mass of a jet is defined, and so are all other components of the jet's kinematics, via the sum of the individual 4-vectors of all the jet's constituent particles[2] :

$$m_{jet}^2 = \left(\sum_i E_i \right)^2 - \left(\sum_i p_i \right)^2 \tag{5.1}$$

Jets that are initiated by a parton other than a top quark (QCD jets) also acquire a mass mainly by means of perturbative gluon emissions, even though partons (light quark and gluons) are to a good approximation massless. The mass of a QCD jet is generally much smaller than the top quark mass. To discriminate against the small

---

[2] In the present case, the constituent particles of jets are topological clusters.

fraction of high mass QCD jets[3] , different properties of the jet substructure are studied.

k_t re-clustering

The basic idea of the technique [78] is to re-cluster, using the k_t algorithm described in section 4.3.2, the constituents of a previously found jet and to stop the clustering procedure in its last iteration before the two final sub-jets are about to be combined to form the original jet. The k_t algorithm combines close-by soft particles at an early stage in the clustering process, in an attempt to reconstruct the parton showering process in a physically meaningful order. It will therefore tend to reconstruct individual parton showers first, one parton at a time, before evaluating if a single jet should contain more than one reconstructed parton shower. The final steps of the k_t re-clustering procedure thus provide a robust way of defining sub-jets that can be mapped to the decay products of the boosted particle under investigation.

One can further exploit the clustering history of the k_t algorithm by extracting the momentum scale at which sub-jets merge, also known as k_t splitting scales [79] [80] [81] [82]. When the last and penultimate sub-jets are about to be merged to form the original jet, this scale naturally corresponds to their k_t distance defined as:

$$\sqrt{d_{12}} = \min\left(p_{T1}, p_{T2}\right) \times \Delta R_{12}, \tag{5.2}$$

---

[3] A high jet mass for generic QCD jets can be due to an energetic gluon emission at a wide angle or to an accidental geometrical overlap of two partons in the detector that are reconstructed as a single jet.

where ΔR_{12} is the Euclidean distance in $\eta - \phi$ space between the two sub-jets.

For a top jet candidate containing the two-body decay $t \to bW$, the k_t re-clustering is expected to result in a value of $\sqrt{d_{12}}$ close to $m_{\text{jet}}/2 \sim m_{\text{top}}/2$, which corresponds to each of the two decay particles carrying approximately half the energy of the top quark.

One way to probe the presence of a real W inside the top jet is to consider the minimum pair-wise invariant mass, Q_W, between the three remaining sub-jets of the k_t re-clustering, as first advocated in [83] and studied in the context of the ATLAS experiment in [84]. Because QCD jets are dominated by asymmetric energy sharing between the sub-jets[4] , the quantities $\sqrt{d_{12}}$ and Q_W are expected to exhibit a steeply falling spectrum for jets initiated by a parton other than a top quark.

N-subjettiness

Another set of jet substructure observables, the N-subjettiness variables τ_N, was recently put forward in [85]. These observables are particularly useful to identify hadronic top decays because they exploit the multi-body kinematics of the decay by quantifying the extent to which a jet can be described by a configuration of at most

---

[4] A QCD jet may acquire a large mass due to the emission of a gluon at a wide angle. However, most of the QCD jet energy will be concentrated in a central core, with only a small amount left for the emitted gluon, resulting in an asymmetry in the energy distribution amongst the sub-jets found by the k_t re-clustering.

N sub-jets. The observables are defined as:

$$\tau_N = \frac{1}{d_0} \sum_k p_{\mathrm{T}k} \times \min\left(\Delta R_{1k}, ..., \Delta R_{Nk}\right) , \quad \text{with } d_0 \equiv \sum_k p_{\mathrm{T}k} \times R \qquad (5.3)$$

where R is the jet size parameter used to reconstruct the original jet, $p_{\mathrm{T}k}$ is the p_{T} of the constituent k and ΔR_{ik} is the (geometrical) distance between constituent k and subjet i. This definition is motivated by the fact that the jet's constituents will tend to be localized around the sub-jets axes in the case when the sub-jets can be mapped to a particle's decay products. This topology corresponds to $\tau_N \approx 0$. A QCD jet on the other hand with no intrinsic hard substructure is much less likely to have constituents aligned with the sub-jet axes resulting in a large value of $\tau_N \gg 0$.

The N-subjettiness observables definition offers some freedom in the choice of the sub-jet directions. Re-clustering the jet's constituents with the k_t algorithm and stopping the process with N (sub-) jets remaining is a safe and robust way of defining those axes [85].

A good discriminating variable for a boosted three-pronged decay is the ratio τ_3/τ_2 that will be herein denoted by τ_{32}. The reason being that a top jet candidate will prefer a three-sub-jets configuration over a two-sub-jets one such that $\tau_3 \ll \tau_2$. A QCD jet on the other hand will not exhibit such a well defined preference and will generally have $\tau_3 \lesssim \tau_2$.

Similarly, the ratio τ_2/τ_1 is denoted τ_{21} and is useful for identifying two-pronged decays inside jets.

5.4.2 Leptonic top tagging

One of the features inherent to boosted topologies is that outgoing particles tend to be close to each other in the detector. In the case of a leptonic top decay $(t \to bW \to bl\nu)$, this translates into the lepton from the W boson decay becoming spatially close to the jet initiated by the b quark. In other words, the lepton becomes *non-isolated*. Multi-jet events can have such non-isolated leptons (especially muons) due to the presence of QCD jets containing heavy flavor mesons (such as B, D mesons) decaying semi-leptonically. In order to discriminate boosted leptonic top decays from QCD jets produced in multi-jet events, a novel lepton isolation requirement, called *mini-isolation*, proposed in [86] and studied in ATLAS in [84, 87] is used. The isolation energy is measured from reconstructed tracks that lie within a cone centered on the lepton's momentum direction. The use of charged particles, reconstructed as *tracks* in the detector, is experimentally more favorable as it mitigates the impact of pile-up on the measured energy deposited around a lepton by selecting particles that stem from a common interaction point (reconstructed as a *vertex*), to which tracks are fitted. The size (in $\eta - \phi$ space) of the cone is defined as:

$$
R_{\text{iso}} = \begin{cases} 0.4 & \text{for} \quad p_{\text{Tlepton}} < 25 \text{ GeV} \\ 10 \text{ GeV}/p_{\text{Tlepton}} & \text{for} \quad 25 \text{ GeV} \le p_{\text{Tlepton}} \le 1 \text{ TeV} \\ 0.01 & \text{for} \quad p_{\text{Tlepton}} > 1 \text{ TeV} . \end{cases} \tag{5.4}
$$

The cone size R_{iso} thus "shrinks" as the transverse momentum of the lepton increases, in order to accommodate the fact that a higher p_{T} top will have smaller angular separations between its decay products and therefore a higher probability

for the hadronic activity from the jet to spatially overlap with the lepton's immediate surroundings. The mini-isolation variable is defined as

$$\text{mini-iso} \equiv \frac{p_{\text{Tlepton}}}{p_{\text{Tlepton}} + p_{\text{Tcone}}}, \tag{5.5}$$

where p_{Tcone} is the scalar sum of the transverse momenta of tracks[5] reconstructed in the Inner Detector that lie within a distance R_{iso} from the lepton.

Figure 5–2 shows the mini-isolation distributions for the different background contributions stacked on each other as well as the distribution measured in data. Two examples of expected signal distributions (semi-leptonic final state of the Z' and g_{KK} $t\bar{t}$ decay) are also shown superimposed. The multi-jet background dominates in muon+jets events, whereas it is almost negligible in electron+jets events, because the reconstruction efficiency of muons *in* jets is much higher than that of electrons. The requirement that at most 5% of the lepton's p_{T} can be found in the isolation cone (mini-iso $> 1/1.05$) results in a signal efficiency of $\sim 90\%$ with a background rejection of about 500 (for muon+jets events), making mini-isolation a very effective discriminating observable.

Because the top quark is expected to be boosted, its visible decay products, that is excluding the neutrino, are identified as a jet-lepton pair satisfying $\Delta R\,(\text{jet}, \text{lepton}) <$ 1. Both the jet and the lepton must satisfy the object selection requirements presented in section 5.3 and, in addition, the lepton must satisfy the mini-isolation

---

[5] The reconstructed tracks are required to have $p_{\text{T}} > 1$ GeV and the track associated with the lepton itself is excluded from the sum.
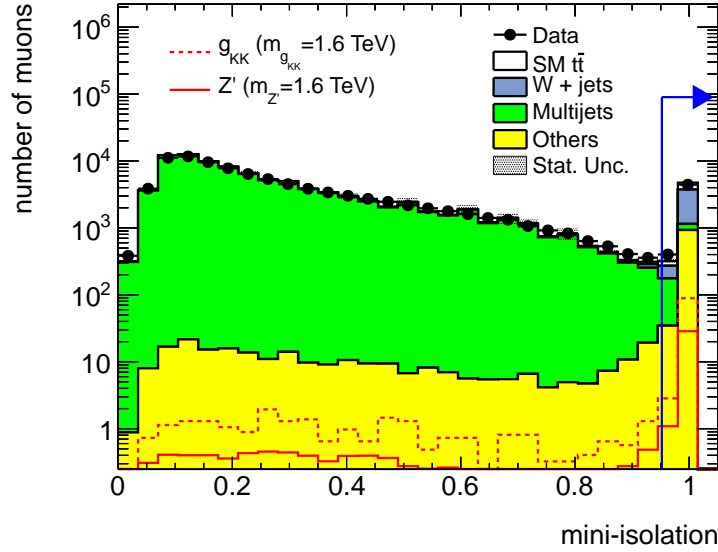
(a)
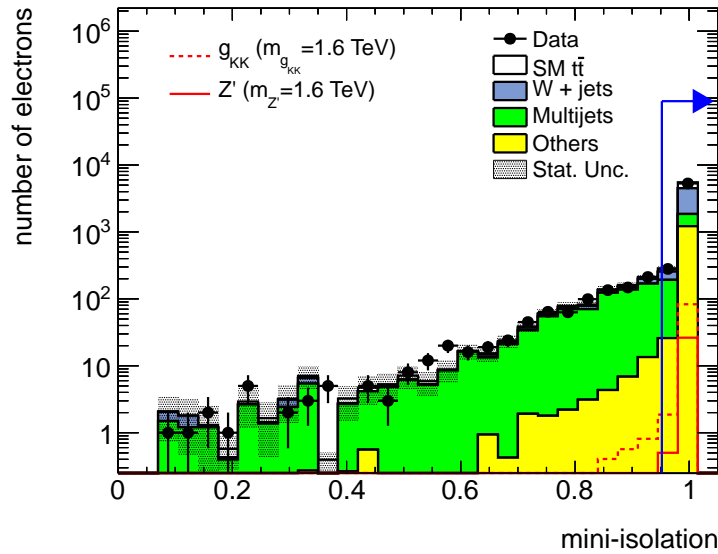
(b)

Figure 5–2: Mini-isolation for selected muons (a) and electrons (b) in events satisfying the basic object selection as well as the trigger requirement. The blue line and arrow indicate the position and direction of the cut value. Backgrounds categorized in *Others*, here and in subsequent figures (unless stated otherwise), consist of $W \rightarrow \tau\nu + $ jets, $Z + $ jets, single top and diboson $(WW/ZZ/WZ)$ production processes. The two signal examples shown here and in subsequent figures are from the two models described in Section 2.3.

requirement. Distributions of $\Delta R\,(\text{jet}, \text{lepton})$ are shown in Figures 5–3 and 5–4 for muons and electrons respectively. Signal is predominant at low values of ΔR by virtue of the Lorentz boost of the top quark. The $W + \text{jets}$ background, on the other hand, shows no such strong preference since to a first approximation no kinematic constraints will force the lepton to be close to a jet.

In ATLAS, clusters of measured energy in the calorimeter can simultaneously satisfy the electron identification selection and also be reconstructed as a jet. In order to reject such pathological top candidates, the jet (in the identified jet-electron pair) must have a k_t splitting scale $\sqrt{d_{12}}$ of at least 10 GeV to account for the expectation that two clusters of energy must be present inside the jet: one from the hadronisation of the b quark itself, and one from the electron. It is also required that the component of the electron's momentum that is perpendicular to the jet direction, multiplied by the ΔR between the two objects, be greater than 1 GeV . More details regarding this overlap removal procedure can be found in [82, 84]. Figures 5–4(a) and 5–4(b) shows the $\Delta R\,(\text{jet}, e)$ distributions before and after this procedure, respectively. As expected, only jet-electron pairs with very small values of ΔR are discarded. The dip at values around $\Delta R \sim 1$ is an artifact of the jet definition used in this analysis (anti-k_t with $R = 1.0$). For ΔR values smaller than 1, the electron energy is very likely to be included in the jet energy which biases $\Delta R\,(\text{jet}, e)$ towards smaller values.

With an identified jet-lepton pair candidate in hand, it is possible to discriminate further genuine boosted top decays from fake candidates found in reducible backgrounds such as multi-jet events. Indeed, the invariant mass of the jet-lepton pair, Q_{visible}, can be used to select leptonically decaying top quark decays. The
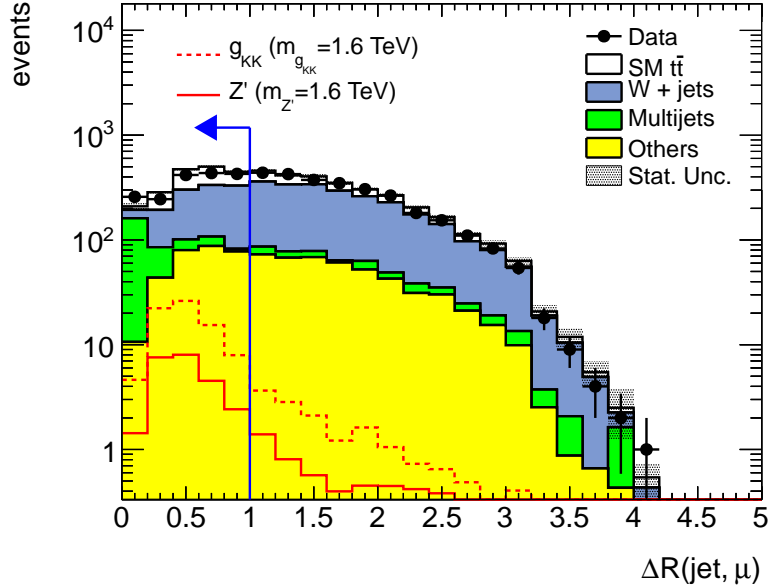
Figure 5–3: $\Delta R\,(\text{jet}, \mu)$ in events satisfying the basic object selection, the trigger requirement and the mini-isolation requirement on the muon. Only the jet-muon pair with the smallest value of ΔR enters the distribution. The blue line and arrow indicate the position and direction of the cut value.

quantity Q_{visible} was proposed in [83] and studied with simulations in the context of the ATLAS experiment in [84]. Appendix A contains a detailed derivation of the kinematically allowed values of Q_{visible}. Figure 5–5 shows the Q_{visible} distribution for jet-muon and jet-electron pairs. In both channels, the signal peaks at high values as expected given that $Q_{visible}$ should be roughly proportional to the top quark mass (minus the neutrino energy). Fake candidates from multi-jet events in particular tend to exhibit low values of Q_{visible}, especially in the muon channel. In order to identify leptonically decaying top quarks, a jet-lepton pair is therefore required to have $Q_{\text{visible}} > 50$ GeV. The peak at $Q_{\text{visible}} \sim 90$ GeV for jet-electron pairs is due to candidates in $Z \to ee$ events where the decaying Z is boosted enough so that both

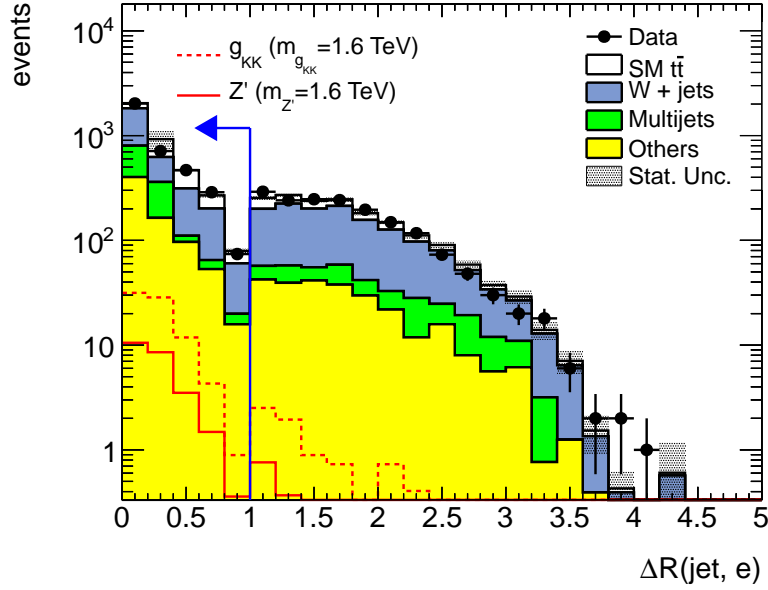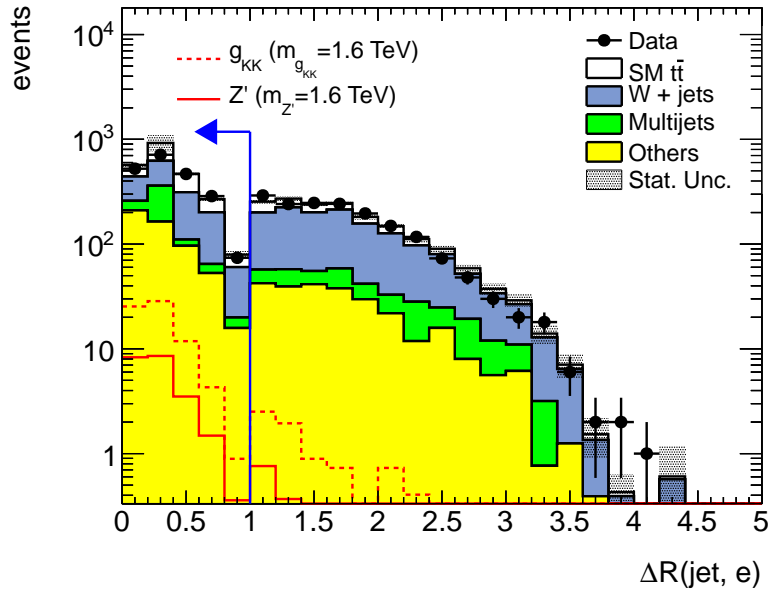Figure 5–4: $\Delta R\,(\mathrm{jet}, e)$ before (a) and after the overlap removal (b), in events satisfying the basic object selection, the trigger requirement and the mini-isolation requirement on the electron. Only the jet-electron pair with the smallest value of ΔR enters the distribution. The blue line and arrow indicate the position and direction of the cut value.

77

electrons end up in a single reconstructed jet. These fake candidates are legitimate as far as the leptonic top quark selection is concerned and no attempt to distinguish them from real top decays is made at this point. The contribution from this background is to be mitigated by also requiring the presence of a hadronically decaying top candidate in the event, as described in the upcoming section.

Another effective way to further probe distinctive features of leptonically decaying top quarks is through a "mass-drop" observable first proposed in [83] and also studied with simulations in the context of the ATLAS experiment in [82, 84]. The mass-drop observable is defined as

$$x_{\text{lepton}} \equiv 1 - \frac{m_b^2}{Q_{\text{visible}}^2}, \tag{5.6}$$

where m_b is taken as the mass of the high-p_{T} jet accompanying the lepton[6]   (i.e. the jet in the jet-lepton pair). When the addition of the lepton does not contribute significantly to Q_{visible}, x_{lepton} will tend towards zero, whereas an important mass-drop resulting from the omission of the lepton's contribution will translate into $x_{\text{lepton}} \to 1$. A large value of x_{lepton} is thus indicative of the fact that the invariant mass of the system composed of the visible decay products (Q_{visible}) is really generated by the geometrical addition of the jet and the lepton. This is indeed the case for genuine leptonically decaying top quarks, as shown in Figure 5–6. In multi-jet events on the

---

[6] When x_{lepton} is calculated for jet-electron pairs, care must be taken to not double count the electron energy, given that it is already included in the jet energy. The quantity m_b is thus computed by subtracting, from the reconstructed jet 4-momentum, the 4-momentum of the electromagnetic cluster associated with the reconstructed electron.
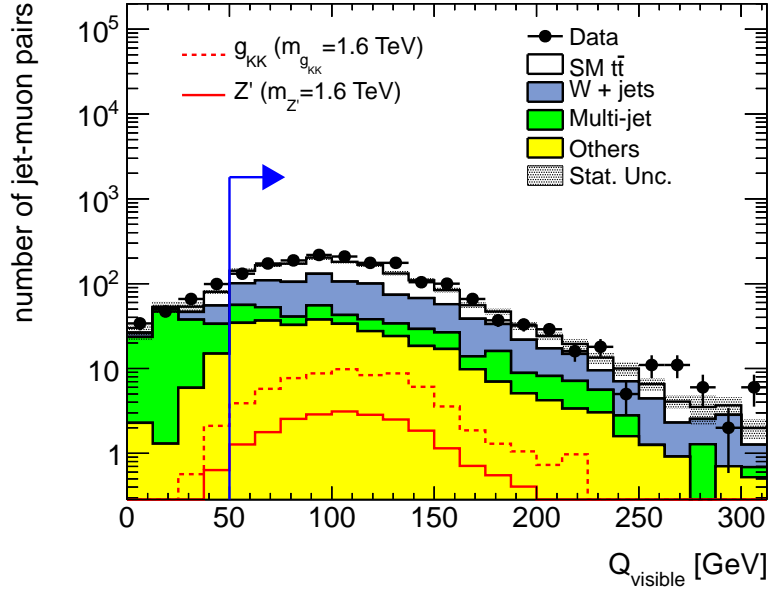
(a)
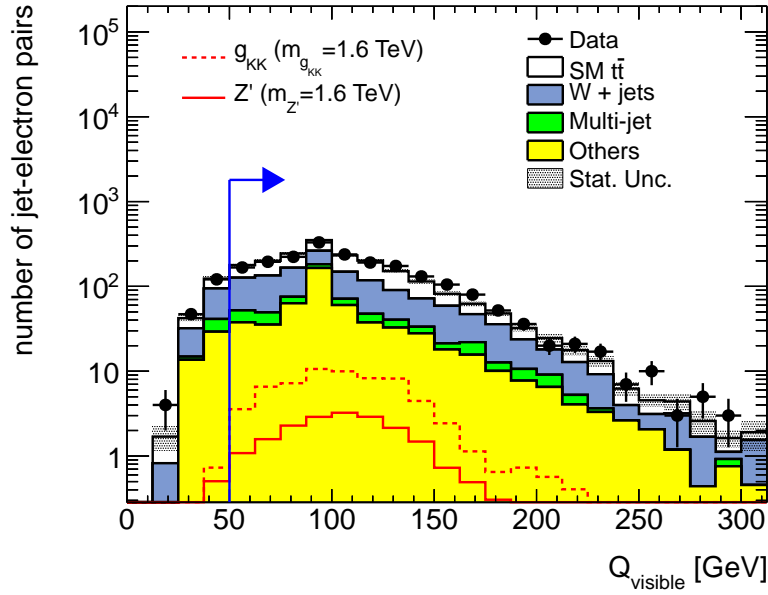
(b)

Figure 5–5: Q_{visible} for jet-muon (a) and jet-electron (b) pairs, in events satisfying the basic object selection, the trigger requirement and the mini-isolation requirement on the lepton. The blue line and arrow indicate the position and direction of the cut value.

79

other hand, the lepton does not carry a significant fraction of the energy of the jet-lepton pair such that high values of Q_{visible} are mostly due to high values of the jet mass itself. Selecting candidates with $x_{\text{lepton}} > 0.5$ therefore results in a high signal efficiency while removing a large fraction of the remaining multi-jet events after the $Q_{\text{visible}} > 50$ GeV requirement, especially in the muon+jets channel.

Both the normalization and shape of the total expected background are in good agreement with the data in terms of the different observables that were presented. Table 5–1 summarizes the selection criteria used to identify a jet-lepton pair candidate as originating from a leptonically decaying top quark. The identification of leptonically decaying top quarks is based solely on the kinematic properties of the identified jet-lepton pair candidate, and does not rely on the full reconstruction of the top decay.

	Observable	Cut
(e only)	$p_{e\perp\text{jet}} \times \Delta R\,(\text{jet}, e)$	> 1 GeV
(e only)	jet $\sqrt{d_{12}}$	> 10 GeV
	lepton mini-iso	> 1/1.05
	$\Delta R\,(\text{jet}, \text{lepton})$	< 1
	Q_{visible}	> 50 GeV
	x_{lepton}	> 0.5

Table 5–1: Observables and kinematic cut values used to identify leptonically decaying top quarks.

Figure 5–7 shows the fraction of leptons selected by the leptonic top tagger selection for various samples of Monte Carlo simulated events. It thus consists of the fraction of reconstructed leptons that satisfy the mini-isolation requirement and that could be associated with a jet to form a jet-lepton pair satisfying the Q_{visible} and
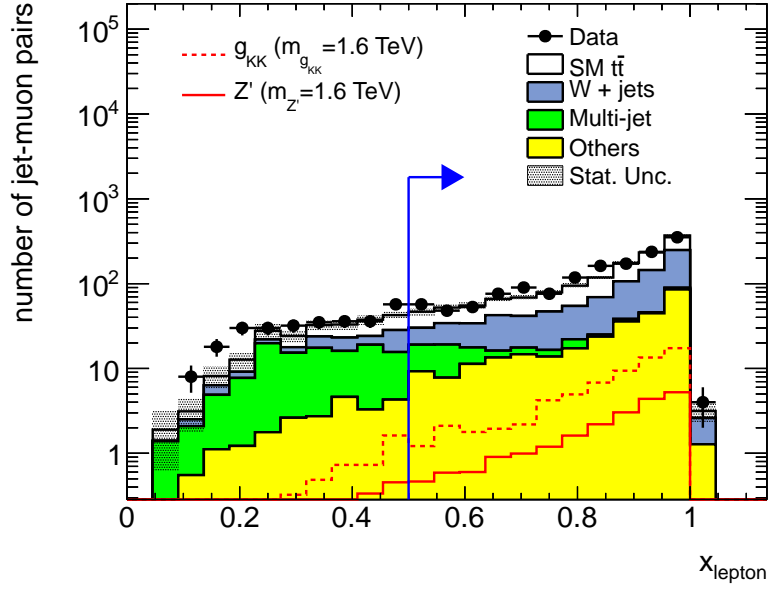
(a)
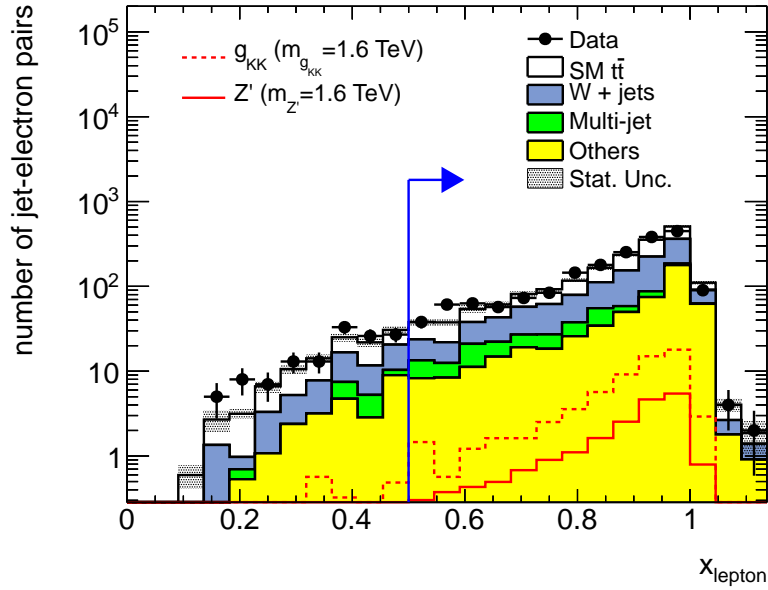
(b)

Figure 5–6: x_{lepton} for jet-muon (a) and jet-electron (b) pairs, in events satisfying the basic object selection, the trigger requirement, the mini-isolation requirement on the lepton, and the Q_{visible} requirement on the jet-lepton pair. The blue line and arrow indicate the position and direction of the cut value.

81

the x_{lepton} requirements. In order to appreciate the selection efficiency on genuine leptonically decaying top quarks, reconstructed leptons in simulated signal and Standard Model $t\bar{t}$ samples were required to be geometrically close (in $\eta - \phi$ space) to the true generated leptons from the W bosons (decaying leptonically). The pronounced downward trend for the multi-jet background in the electron channel is due to events in which the leading or sub-leading jet was falsely identified as an electron. In such cases, since the electron candidate and the close-by high-p_{T} jet are in fact the same object, the leptonic top candidate fails the overlap removal requirement.

5.4.3 Hadronic top tagging

With a tagged leptonic top candidate in the event, the goal is now to identify another reconstructed jet in the detector that could be a hadronic top candidate. In the boosted top reconstruction approach, it is expected that all the decay products of the boosted top quark $(t \rightarrow Wb \rightarrow q'\bar{q}b)$ will be reconstructed as a single large-R jet. An efficient way to ensure that this is actually the case is to select candidates with a high reconstructed jet mass calculated after the jet trimming procedure.

Figure 5–8 shows the reconstructed jet mass for high-p_{T} ($p_{\text{T}} > 350$ GeV) hadronic top candidates in a Standard Model $t\bar{t}$ Monte Carlo sample, before and after the jet trimming procedure. The jet mass calculated using trimmed jet shows three distinct regions. First, trimmed jets reconstructed to have a low value of jet mass correspond to jets that contain either only one of the three top quark decay products, or an energetic light quark or gluon from the underlying event. Trimmed jets with $m_{\text{jet}} \sim m_W$, on the other hand, correspond to jets that contain only two of the three
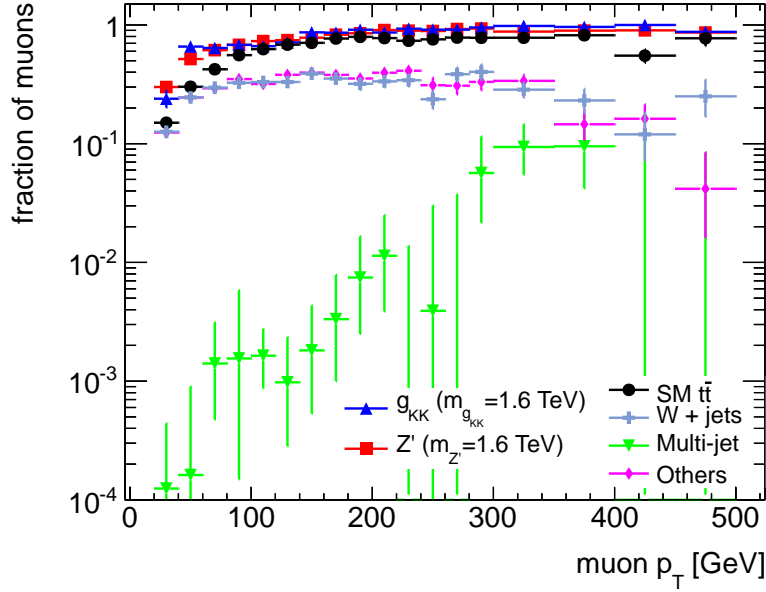
(a)
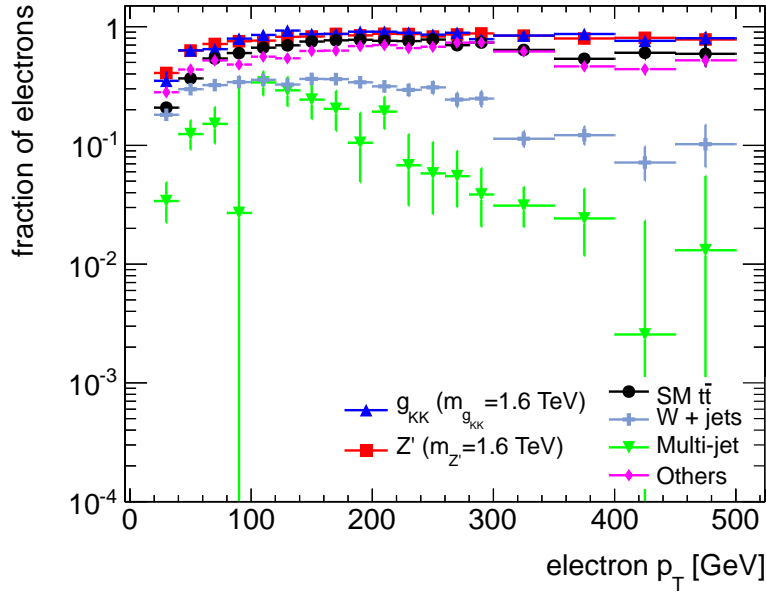
(b)

Figure 5–7: Fraction of muons (a) and electrons (b) selected by the leptonic top tagger selection in Monte Carlo simulated events satisfying the basic object selection. For the signal and Standard Model $t\bar{t}$ samples, reconstructed leptons are geometrically matched to the true generated leptons from W decays. Error bars represent the statistical uncertainties.

decay products. The second peak is located at a value of jet mass close to the W
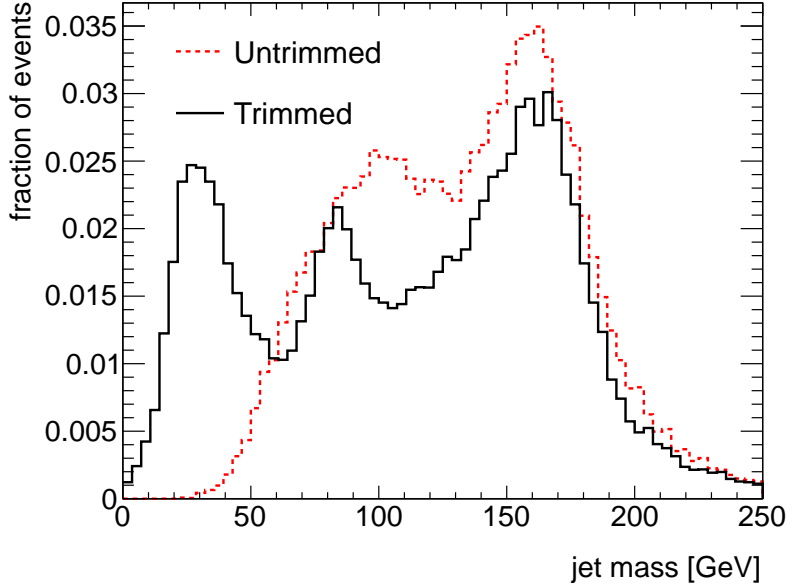
Figure 5–8: Jet mass calculated from untrimmed and trimmed jets for high-p_T hadronic top candidates in Monte Carlo simulations of SM $t\bar{t}$ decaying to a semi-leptonic final state. Both distributions are normalized to unity.

mass when the two quarks originating from the W decays are contained within the top jet[7] . Finally, when all three decay products are contained in a single jet, the reconstructed jet mass value lies near m_top. The reconstructed trimmed jet mass of the hadronic top candidate can thus be used to differentiate the different top decay topologies.

---

[7] The reconstructed jet mass of a jet containing the b quark and one quark from the W decay will also lie in the vicinity of m_W due to kinematic constraints[84].

The assumptions regarding the mapping of the reconstructed trimmed jet mass onto the decay topology are confirmed by looking at the correlations between the jet mass and the N-subjettiness variables, τ_{21} and τ_{32}, for which values towards zero indicate a preference for a 2-sub-jets or 3-sub-jets configuration, respectively. As shown in figure 5–9, low-mass jets show no preference for either configurations (both τ_{ij} values tend towards one), which is consistent with the "one parton" hypothesis. Medium-mass jets, however, are definitely more likely to contain only 2 hard sub-jets (i.e. τ_{21} is closer to zero, while τ_{32} is close to one). Finally, jets reconstructed to have a higher value of jet mass are better described by 3-sub-jets configurations (τ_{32} tends towards zero). The (trimmed) jet mass therefore gives a good description of the substructure topology of boosted hadronic top decays. The selected hadronic top candidates are thus required to have at least 120 GeV of jet mass in order to ensure that all three decay products are fully contained in the reconstructed jet for a large fraction of the top candidates.

Figure 5–10 shows the distribution of the jet mass in events where one leptonically decaying top candidate was identified using the selection criteria presented in the previous section. The contribution to the expected background from boosted hadronically decaying top quarks is clearly visible as a bump at approximately the top quark mass value.

Many processes predicted by the Standard Model (but other than top-antitop pair production) produce high mass jets. In the context of the semi-leptonic $t\bar{t}$ final state, after the leptonic top tagging selection, the dominant reducible background comes from events that contain a prompt lepton and a number of high p_{T} jets,
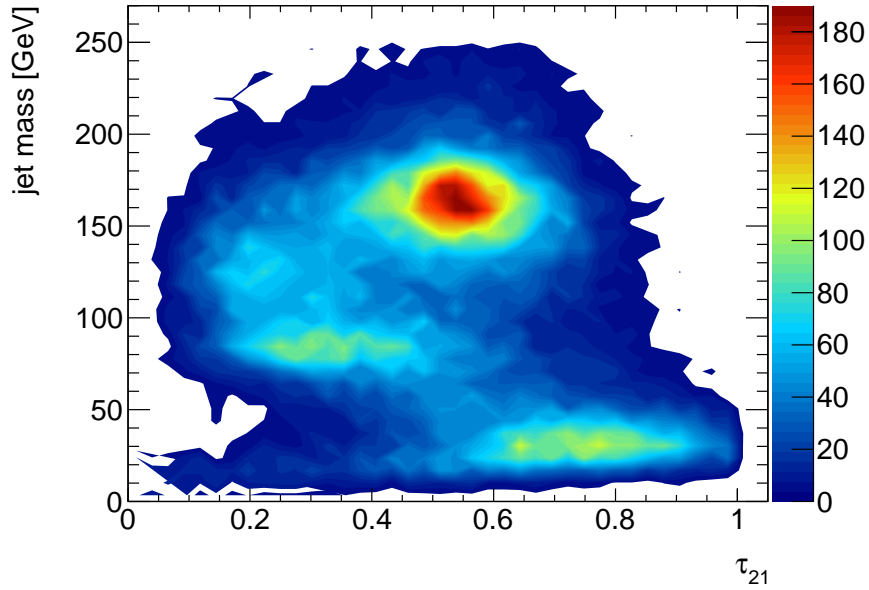
(a)
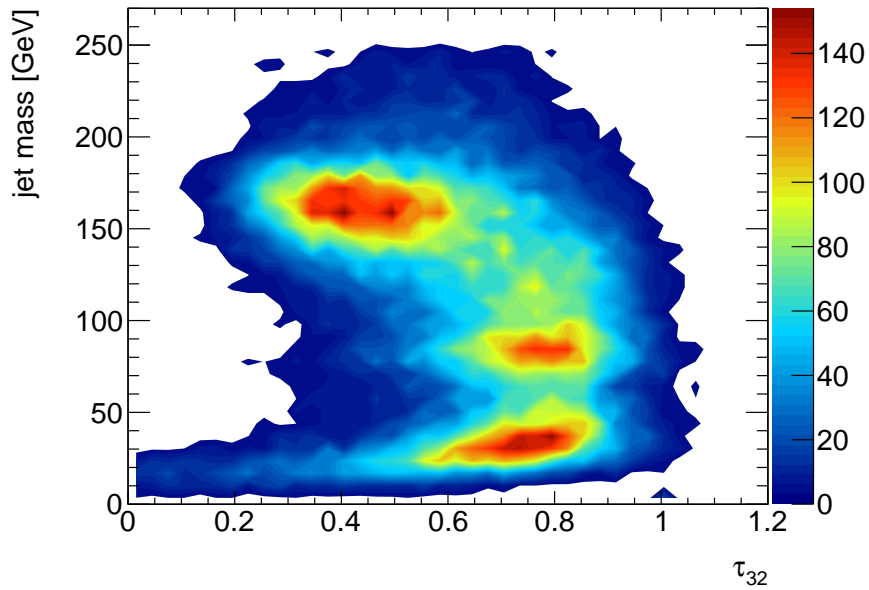
(b)

Figure 5–9: Correlations between the hadronic top candidates (trimmed) jet mass and N-subjettiness variables τ_{21} (a) and τ_{32} (b) in SM $t\bar{t}$ Monte Carlo events decaying semi-leptonically. The two dimensional distributions are arbitrarily normalized.

86
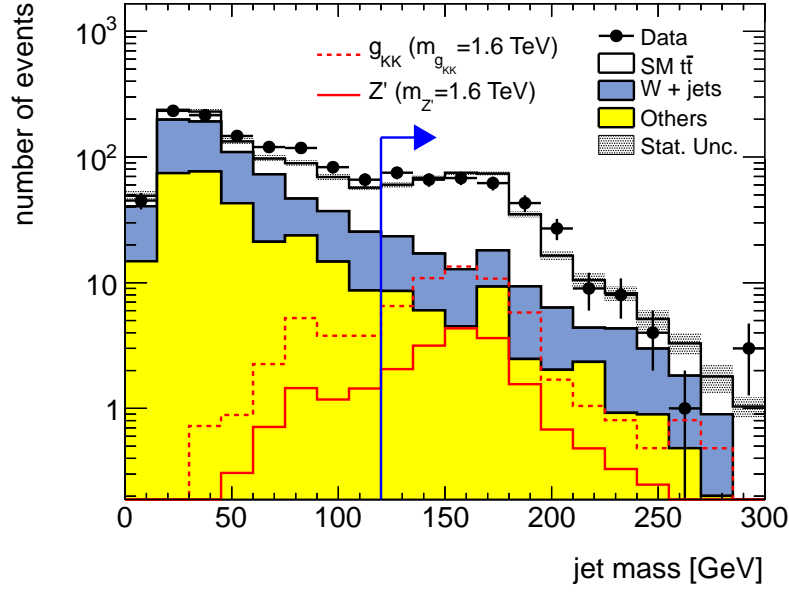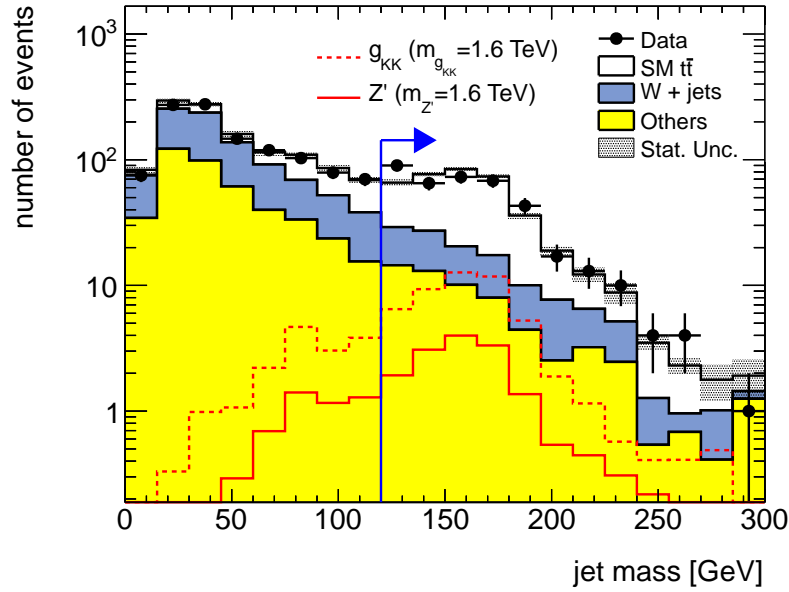
Figure 5–10: Jet mass of the highest-p_{T} jet ($p_{\mathrm{T}} > 350$ GeV) in events where one leptonic top candidate was identified in the muon + jets channel (a) and the electron + jets channel (b). The multi-jet background contribution is included in the "Others" category. The blue line and arrow indicate the position and direction of the cut value.

such as those coming from the direct production of a (leptonically decaying) W boson together with three or more energetic partons. In this case, high mass jets emerge when two spatially close partons are reconstructed in a single large-R jet. As previously discussed, one distinctive feature of boosted hadronic top decay is the presence of a hadronic W boson decay within the reconstructed jet. Candidate jets that do exhibit this feature can be selected by requiring a large value of the jet substructure observable Q_W together with a small value of τ_{32}. Figure 5–11 shows the correlation between the two variables in signal (Z', with $m_{Z'} = 1.6$ TeV) and background (W+jets) events for a high-mass hadronic top candidate. Requiring that candidates, which already have $p_{\mathrm{Tjet}} > 350$ GeV and $m_{\mathrm{jet}} > 120$ GeV, further satisfy $Q_W > 40$ GeV and $\tau_{32} < 0.75$ results in approximately 75% of the signal events being selected whereas only one background event out of three is selected. Furthermore, requiring that the hadronic top candidate satisfies $\tau_{21} > 0.2$ (i.e. not consistent with being made of two objects) slightly increases the background rejection while preserving the fraction of selected signal events. Figures 5–12, 5–13 and 5–14 present the distribution of hadronic top candidate Q_W, τ_{32} and τ_{21} values respectively. Despite some statistical fluctuations, the distributions observed directly in data are in good agreement with the expectations obtained from Monte Carlo simulations.

Both the normalization and shape of the total expected background are in good agreement with the data in terms of the different observables that were presented. Table 5–2 summarizes the set of observables and associated cut values used to identify hadronically decaying top quarks. These requirements select high-p_{T} jets with a mass
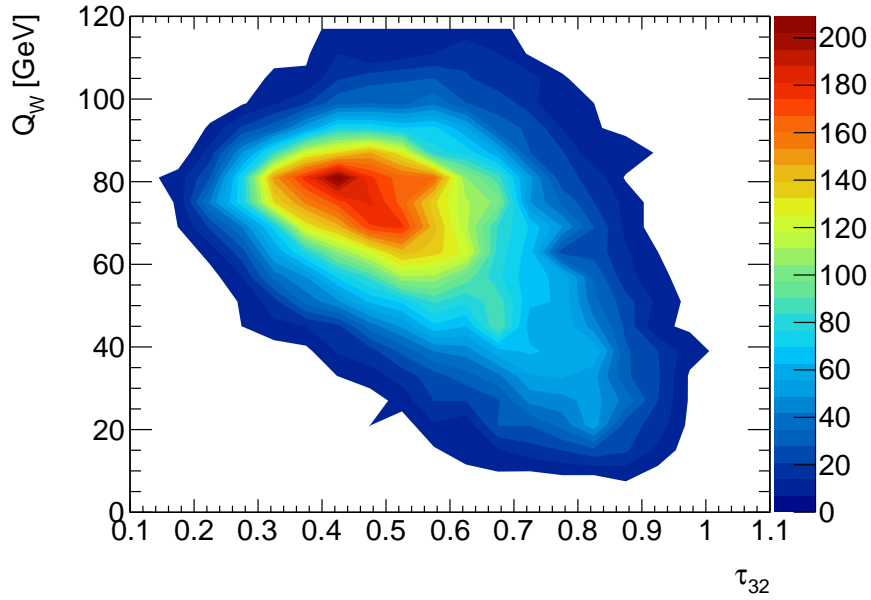
(a)
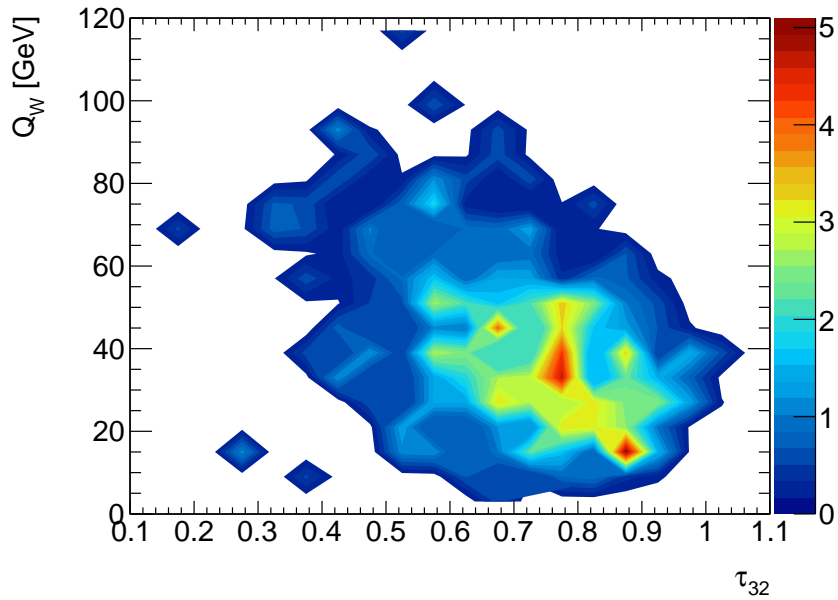
(b)

Figure 5–11: Correlations between high-mass ($m_{\text{jet}} > 120$ GeV) hadronic top candidates jet Q_W and N-subjettiness variable τ_{32}, in $Z' \to t\bar{t}$ (a) and W+jets background (b) Monte Carlo events. The two dimensional distributions are arbitrarily normalized.
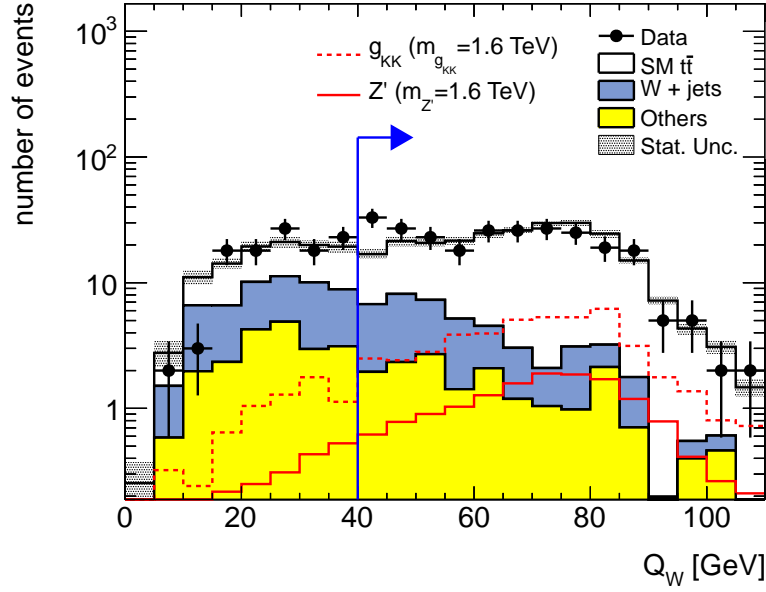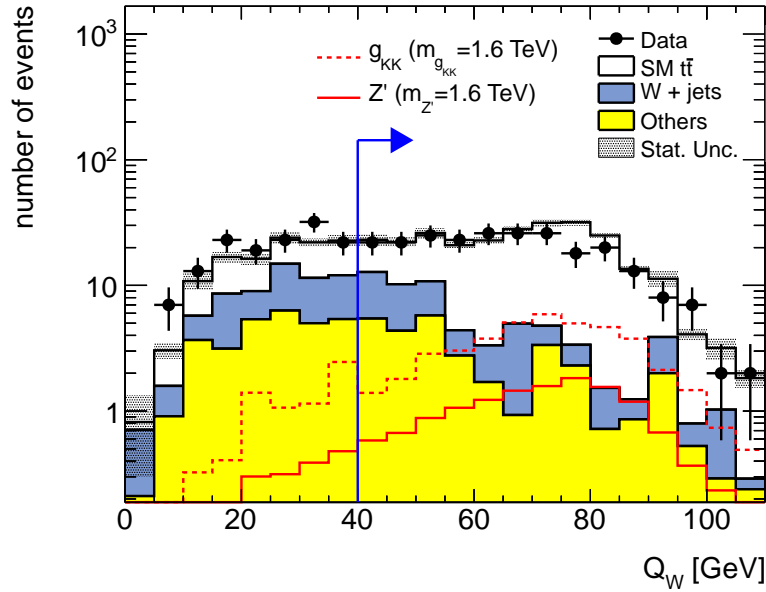
Figure 5–12: Jet Q_W for high-mass (jet mass > 120 GeV) jets in events where one leptonic top candidate was identified in the muon + jets channel (a) and the electron + jets channel (b). The multi-jet background contribution is included in the "Others" category. The blue line and arrow indicate the position and direction of the cut value.

Figure 5–13: Jet τ_{32} for high-mass (jet mass > 120 GeV) jets in events where one leptonic top candidate was identified in the muon + jets channel (a) and the electron + jets channel (b). The multi-jet background contribution is included in the "Others" category. The blue line and arrow indicate the position and direction of the cut value.

Figure 5–14: Jet τ_{21} for high-mass (jet mass > 120 GeV) jets in events where one leptonic top candidate was identified in the muon + jets channel (a) and the electron + jets channel (b). The multi-jet background contribution is included in the "Others" category. The blue line and arrow indicate the position and direction of the cut value.

Observable	Cut
p_{T}	> 350 GeV
mass	> 120 GeV
Q_W	> 40 GeV
τ_{32}	< 0.75
τ_{21}	> 0.2

Table 5–2: Observables and cut values used to identify hadronically decaying top quarks. All variables are computed on trimmed jets.

consistent with the top quark mass, and which exhibit a 3-sub-jets configuration with two sub-jets being consistent with a W boson hadronic decay.

Figure 5–15 shows the fraction of events selected by the hadronic top identification in Monte Carlo simulated events. For all simulated samples, events are required to contain at least one leptonically decaying reconstructed top candidate. For the Standard Model $t\bar{t}$ and signal samples, only events in the true generated semi-leptonic final state were considered and the highest-p_{T} jet in the event was required to geometrically match a generated hadronically decaying top quark. For genuine top quark decays, the fraction of selected events increases as a function of the jet p_{T} up to approximately 70% in signal events. The fraction of events selected in reducible backgrounds remains mostly below 10% for the whole jet p_{T}-range under consideration.

5.5 $M_{t\bar{t}}$ reconstruction

Once both hadronic and leptonic top decays have been identified in the event, the mass of the $t\bar{t}$ system is reconstructed using the two jets, the identified lepton, and the missing transverse energy. To that end, the four-momentum of the two top
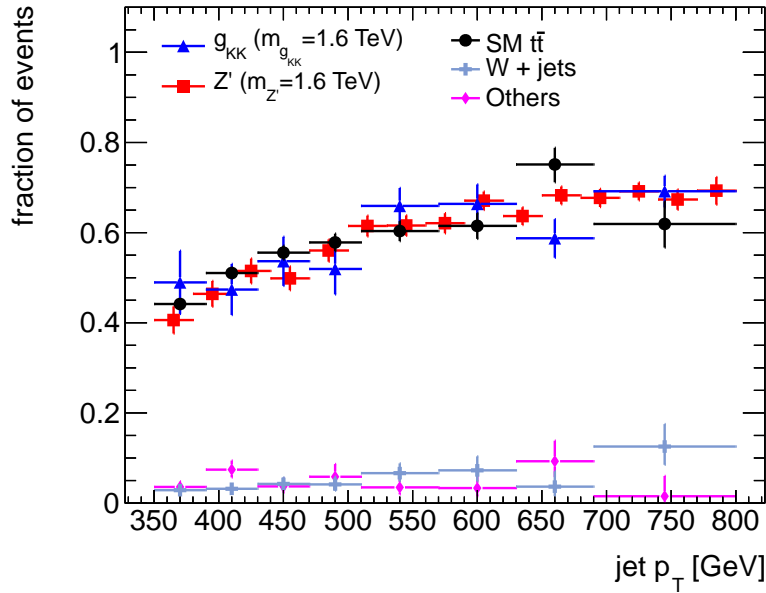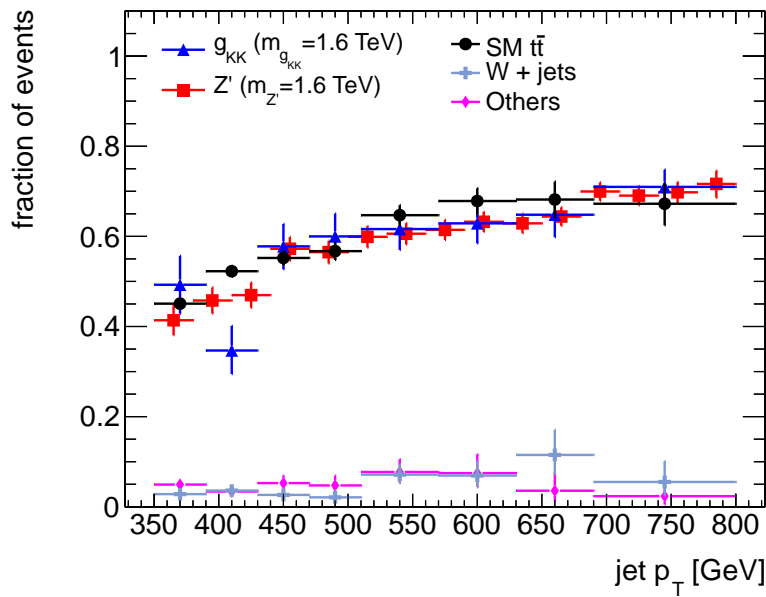
Figure 5–15: Fraction of events in which the highest-p_T jet was selected by the hadronic top tagger selection in Monte Carlo simulated events for the muon + jets (a) and electron + jets (b) channels. Only events in which a leptonic top candidate was already identified are considered. For the signal and Standard Model $t\bar{t}$ samples, reconstructed highest-p_T jets are geometrically matched to true generated hadronically decaying top quarks. Error bars show only the statistical uncertainties.

94

quark candidates are individually reconstructed. The reconstructed four-momentum of the hadronic top candidate is simply taken to be the 4-momentum of the identified hadronically decaying top jet. The four-momentum of the leptonic top quark is reconstructed from the identified jet-lepton pair and reconstructed neutrino. The z-component of the neutrino's momentum is calculated from the four-momentum of the lepton and the $E_{\mathrm{T}}^{\mathrm{miss}}$. The addition of the lepton and neutrino four-momenta is required to be equal to a four-momentum vector with mass equal to that of the W boson[8] . The reconstructed neutrino should further satisfy $\Delta R\left(l, \nu_l\right) < 1.2$, given that the top's decay products are expected to be collimated. Figure 5–16 shows the distribution of $\Delta R\left(l, \nu_l\right)$ and confirms that most candidates in signal events have low values of $\Delta R\left(l, \nu_l\right)$. The leptonic top four-momentum is then defined as the sum of the jet-lepton pair and reconstructed neutrino four-momenta[9] . The leptonic top candidates are also required to have a reconstructed mass and p_{T} of at least 120 GeV and 350 GeV, respectively, in order to be consistent with the hadronic top quark selection and select candidates with kinematic properties compatible with a boosted top quark. Figure 5–17 shows the distribution of the leptonic top candidate mass. After all previous requirements applied, the selected leptonic top candidates already preferentially have high reconstructed mass values. This last requirement

---

[8] The reconstruction of the z-component of the neutrino based on the W mass constraints amounts to solving a quadratic equation. If two solutions exist for the neutrino's p_z, the smallest $|p_z|$ is taken. If no real solution exists, only the real part of the complex solutions is considered [82].

[9] When the reconstructed lepton is an electron, the lepton four-momentum is not explicitly added because it is already included in the jet kinematics.

thus removes an additional small number of background events with a very minimal impact on the signal efficiency.

Figures 5–18(a), 5–18(b) and 5–18(c) show the reconstructed mass resolution for Z' and g_{KK} signal samples after the full selection. A mass resolution of approximately 6-10% [10] is obtained for both semi-leptonic final states considered in the analysis. The tail towards negative value for high mass samples is due to an increasing amount of radiation from the top quarks that fails to be included in the reconstructed jet energy.

The total combined reconstruction and selection efficiency is presented in Figure 5–18(d) as a function of the mass points at which the Z' and the g_{KK} were generated. The efficiency increases with the mass as a larger fraction of boosted top decays can be successfully identified. The difference between the electron + jets and muon + jets channels at high masses of the $t\bar{t}$ system is due to the lower electron reconstruction and identification efficiency at very high-p_{T}. In contrast with the narrow Z' resonance, the mass distribution of the $t\bar{t}$ system in the g_{KK} samples is much more skewed towards lower mass values for high values of the generated g_{KK} pole mass. The selection efficiency for the g_{KK} signal is thus slightly lower than that of the Z'.

---

[10] As estimated by the standard deviation of a Gaussian fitted to the central core of the distribution.
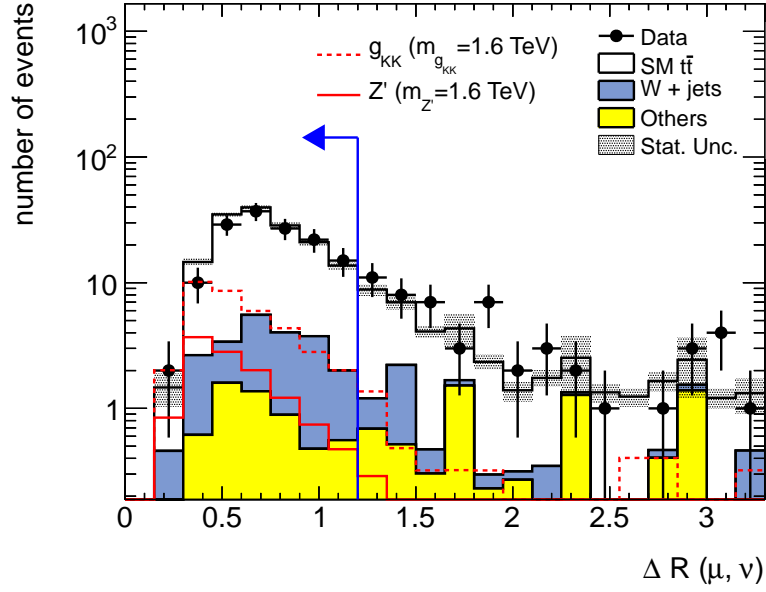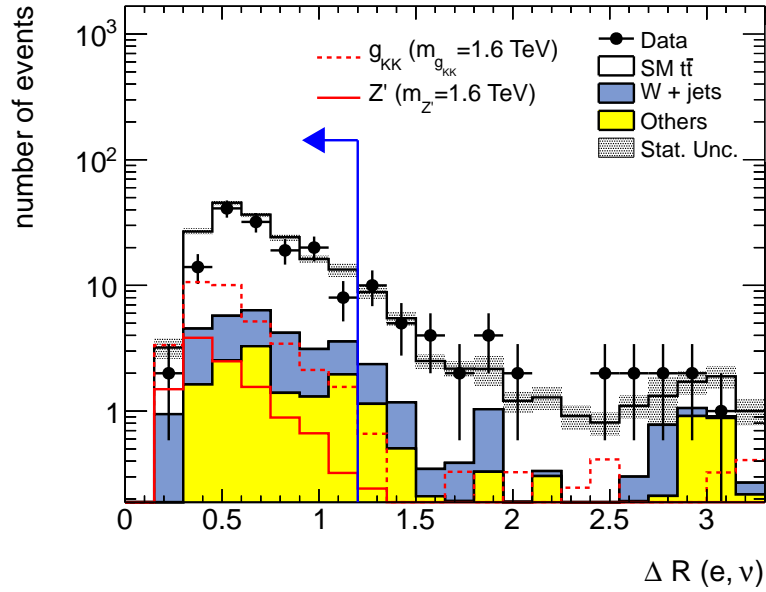
Figure 5–16: $\Delta R(l, \nu_l)$ for leptonic top candidates with $p_{\mathrm{T}} > 350$ GeV in the muon + jets (a) and the electron + jets (b) channels. Events are required to have an identified leptonic and hadronic top candidates. The blue line and arrow indicate the position and direction of the cut value.

97
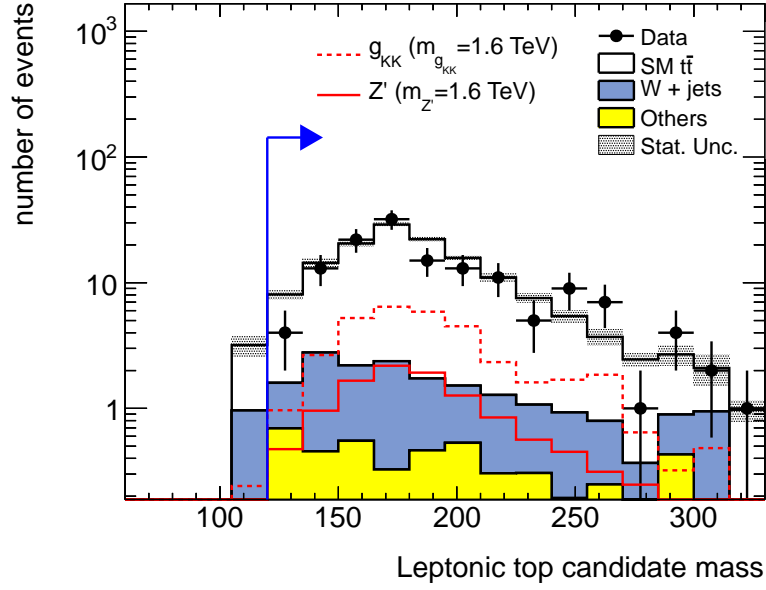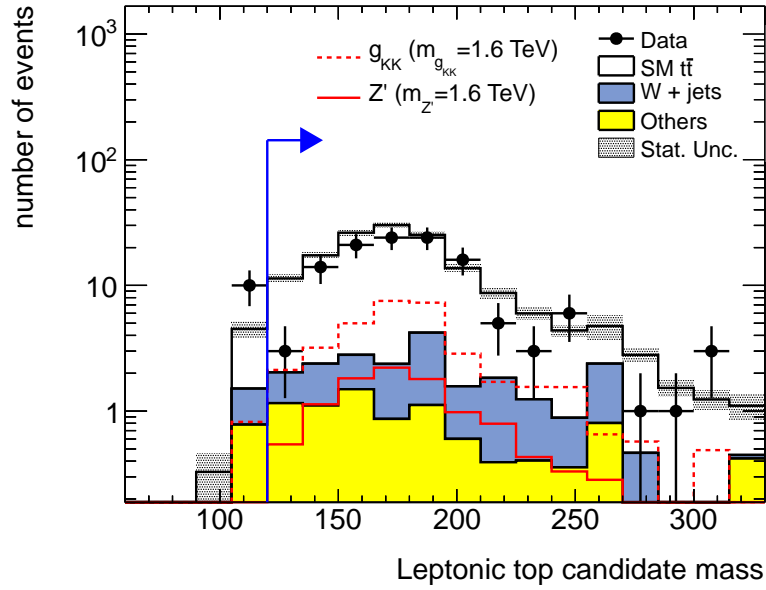
Figure 5–17: Leptonic top candidate mass for leptonic top candidates with $p_T >$ 350 GeV and $\Delta R\,(l, \nu_l) < 1.2$ in the muon + jets (a) and the electron + jets (b) channels. Events are required to have an identified leptonic and hadronic top candidates. The blue line and arrow indicate the position and direction of the cut value.
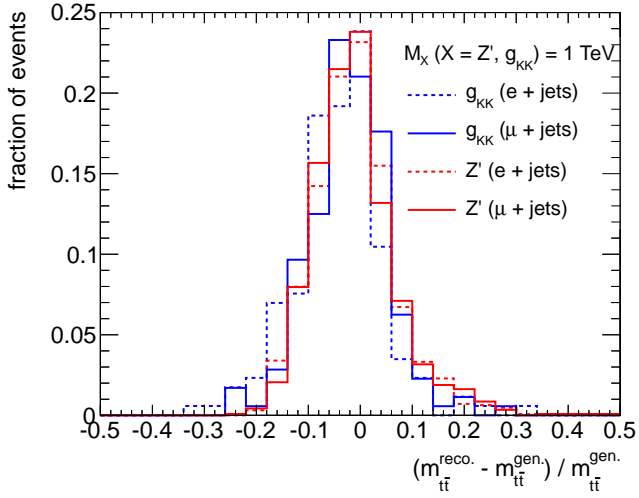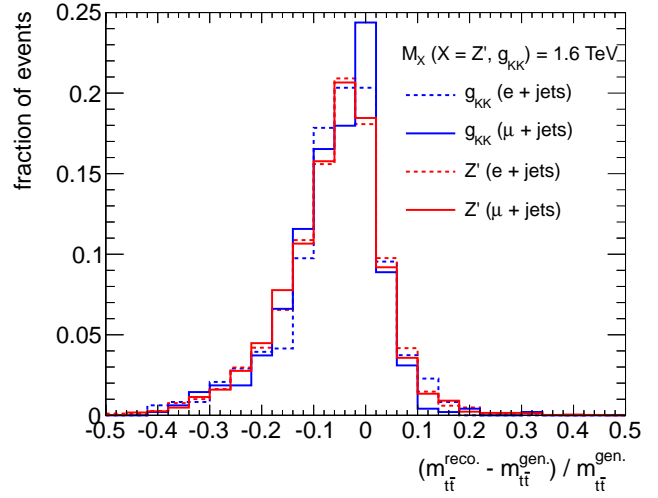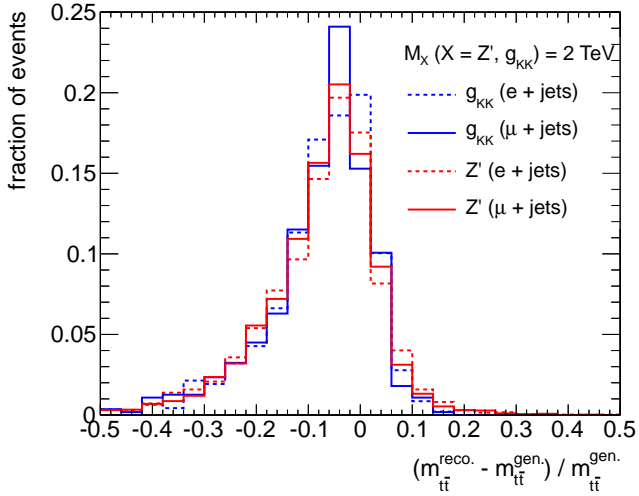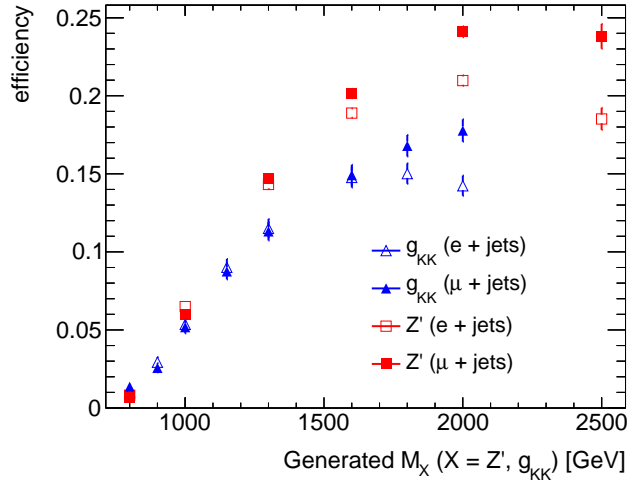
Figure 5–18: Relative difference between the reconstructed and generated mass of the $t\bar{t}$ system in Z' and g_{KK} samples after the full event selection for $m_{Z',g_{KK}} = 1$ TeV (a), 1.6 TeV (b) and 2 TeV (c). Reconstruction and selection efficiency of the $t\bar{t}$ system, as a function of the generated mass points for the Z' and g_{KK} signal samples (d).

99

5.6 Cutflow

Tables 5–3(b) and 5–3(a) present the number of data events selected after the different stages of the event selection. The number of events selected in the different Monte Carlo samples of simulated events is also shown with the associated statistical uncertainty. The "Object selection" comprises the preselection detailed in Section 5.1 as well as the criteria presented in Section 5.3. The "Trigger" selection is described in Section 5.2. The "Leptonic top" and "Hadronic top" selections are detailed in Tables 5–1 and 5–2 respectively. The "Full $M_{t\bar{t}}$" selection is presented in Section 5.5. The steps of the event selection are cumulative; they include the results from the previous steps. A negligible number of multi-jet events remain after the full selection. Similarly, only a small number of events from the other reducible backgrounds (notably W+jets production) satisfy all requirements. The majority of selected events come from the irreducible contribution from Standard Model $t\bar{t}$ production which exhibits the exact same final state as signal events.

Requirements (μ+jets)	Data	Total bkg.	Backgrounds				Signals	
			SM $t\bar{t}$	W+jets	multi-jet	Others	Z'	g_{KK}
Object selection + trigger	92887	94300 ± 1700	1828 ± 17	1997 ± 25	89500 ± 1700	995 ± 15	82 ± 1	248 ± 5
Leptonic top	1465	1393 ± 17	531 ± 5	527 ± 12	51 ± 7	284 ± 8	32 ± 1	96 ± 3
Hadronic top	228	234 ± 5	196 ± 3	23 ± 4	4 ± 2	11 ± 1	16 ±1	48 ± 2
Full $M_{t\bar{t}}$	143	151 ± 3	130 ± 3	16 ± 2	0 ± 1	5 ± 1	13 ± 1	39 ± 2

(a)

Requirements (e+jets)	Data	Total bkg.	Backgrounds				Signals	
			SM $t\bar{t}$	W+jets	multi-jet	Others	Z'	g_{KK}
Object selection + trigger	6186	5836 ± 53	1063 ± 8	2394 ± 31	1357 ± 40	1022 ± 15	40 ± 1	126 ± 3
Leptonic top	1934	1918 ± 22	629 ± 6	666 ± 16	106 ± 11	517 ± 10	31 ± 1	100 ± 3
Hadronic top	217	242 ± 5	195 ± 3	23 ± 3	6 ± 3	18 ± 2	14 ±1	45 ± 2
Full $M_{t\bar{t}}$	126	158 ± 4	134 ± 3	15 ± 2	1 ± 1	8 ± 1	12 ±1	39 ± 2

(b)

Table 5–3: Number of selected events after the different criteria were applied in the μ+jets (a) and e+jets (b) channels. Backgrounds categorized in *Others* consist in $W \to \tau\nu$ + jets, Z + jets, single top and diboson ($WW/ZZ/WZ$) production processes. The signal samples correspond to a generated mass of 1.6 TeV. The quoted uncertainties are statistical only.

CHAPTER 6
Systematic uncertainties

Many systematic uncertainties limit the precision at which the reconstructed $t\bar{t}$ mass distribution can be predicted. They can be categorized into two groups: uncertainties on the reconstructed properties of physics objects (e.g. jet energy) and uncertainties on the modeling of the different expected background and signal processes.

6.1 Object reconstruction

Uncertainties on the reconstructed properties of physics objects used in the selection can affect the predictions of both the event yield (i.e. the number of events entering the $M_{t\bar{t}}$ distribution) and the reconstructed invariant mass of the $t\bar{t}$ system. Both background and signal efficiencies are affected by uncertainties associated with the reconstruction of physics objects.

Uncertainties on the measured trajectory and energy of leptons, as well as uncertainties on the $E_{\mathrm{T}}^{\mathrm{miss}}$ values were estimated to be small (sub-percent level for leptons [88] [89] [66], a few percent for $E_{\mathrm{T}}^{\mathrm{miss}}$ [76]). The impact of these uncertainties on the reconstructed invariant mass of the $t\bar{t}$ system was estimated by varying (up and down) the energy scale of the leptons and of the $E_{\mathrm{T}}^{\mathrm{miss}}$ values by an amount corresponding to their uncertainty. The resulting variations in the expected $M_{t\bar{t}}$ distribution is

small and within the Monte Carlo statistical uncertainty. These uncertainties were therefore not considered further in the analysis.

6.1.1 Jet reconstruction and identification

Uncertainties associated with the measured properties of jets have the largest impact on the prediction of the $M_{t\bar{t}}$ distribution notably because jets account for a significant fraction of the energy of the $t\bar{t}$ system. The values of systematic uncertainties related to the measured jet properties are estimated using an inclusive jet sample which covers a wide range of jet p_{T} values, as described in [75].

Systematic uncertainties associated with the jet energy calibration result in uncertainties on the measured jet transverse momentum and jet mass, and therefore have a direct impact on the $M_{t\bar{t}}$ reconstructed value.

The relative scale uncertainty on the reconstructed jet p_{T} is approximately 4-5% [75]. The effect on the $M_{t\bar{t}}$ distribution, obtained by varying in a correlated way all jet reconstructed p_{T} values by that amount (in all MC samples), varies as a function of $M_{t\bar{t}}$ between 10% and almost 40%.

The jet mass scale uncertainty ranges between approximately 5% and 8% depending on the $|\eta|$ and p_{T} of the jets [75]. It is treated here as being uncorrelated with the p_{T} scale uncertainty but fully correlated with the uncertainty in the reconstructed value of Q_W[1] . The effect of the jet mass scale uncertainty on the $M_{t\bar{t}}$ distribution is thus obtained by varying (up or down) the reconstructed jet mass value according

---

[1] The jet substructure observable Q_W is a measure of mass. Both Q_W and the jet mass are thus affected in a similar way by different distributions of the energy inside a jet.

to the mass scale uncertainty. At the same time, the cut value on Q_W is changed by 5% (up or down, in the same direction as the jet mass variation) which corresponds to the jet mass scale uncertainty that applies to the vast majority of the selected jets. This procedure results in a 5-15% effect on the $t\bar{t}$ mass distribution.

Potential mis-modeling of the spatial and energy distributions of the calorimeter clusters inside a jet will have an impact on the reconstructed values of jet substructure variables used in the top identification algorithms. This in turn will affect the number of top quark candidates identified, thereby having a direct impact on the reconstructed invariant mass distribution of the $t\bar{t}$ system. The method used to estimate an uncertainty associated with the reconstruction of the variable Q_W was described in the previous paragraph. From the studies of the substructure variables presented in [75], a 5% uncertainty on the reconstructed value of each of the variables $\sqrt{d_{12}}$, τ_{21} and τ_{32}, independent on the jet p_{T}, was assumed. The effect of these uncertainties on the $M_{t\bar{t}}$ distribution was estimated by varying, independently, the cut value on each of these three variables by $\pm 5\%$. The resulting variations on the $M_{t\bar{t}}$ distribution range between 1% and 20%.

The uncertainties associated with other variables used specifically for the leptonic top identification are either accounted for indirectly through uncertainties on the jet kinematics[2] or benefit from being a ratio of quantities that are both affected

---

[2] For instance, the uncertainty on the reconstructed value of Q_{visible} is accounted for in the estimation of the systematic variation of the $M_{t\bar{t}}$ distribution due to the uncertainty on the jet mass scale.

similarly by systematic uncertainties which, to a first approximation, cancel out.

6.2 Simulation uncertainties

Theoretical predictions of the reconstructed invariant mass of the $t\bar{t}$ system depend on several approximations. These include calculations of the cross-section of a process at a finite order in perturbative theory, dependence of higher order cross-section calculations on the renormalization and factorization scales, and parameterization of non-perturbative effects (e.g. PDF, parton showering and hadronisation). Uncertainties on the theoretical predictions of the $M_{t\bar{t}}$ distribution are obtained by varying several parameters on which the event simulation depends, as well as by estimating the impact on the $M_{t\bar{t}}$ distribution of some of the approximations made. Since the Standard Model $t\bar{t}$ and W+jets events constitute together $\sim 95\%$ of the total number of expected background events, simulation uncertainties are only estimated for these two classes of events, in addition to their effect on signal events.

6.2.1 Standard Model $t\bar{t}$ production

Many systematic uncertainties affecting the predicted $t\bar{t}$ reconstructed mass distribution of Standard Model $t\bar{t}$ events are investigated. These uncertainties can have an impact on either the normalization or the shape of the distribution, or have an impact on both. They are all considered uncorrelated to each other such that the contributions from all the different sources of uncertainty are added in quadrature to obtain a total uncertainty.

The uncertainty on the predicted $t\bar{t}$ cross-section used to normalize the simulated distribution of SM $t\bar{t}$ events is estimated to be 10.7%. This uncertainty corresponds

to the sum in quadrature of uncertainties on the choice of renormalization[3] and factorization[4] scales, parton distribution function (PDF), and value of α_S used in the calculation of the $t\bar{t}$ cross-section [90][25][56]. This uncertainty only applies to the normalization of the predicted $M_{t\bar{t}}$ distribution.

The uncertainty on the predicted SM $t\bar{t}$ mass distribution due to next-to-leading order scale corrections was obtained by multiplying or dividing by a factor of two the renormalization and factorization scales for samples generated with MC@NLO. Each variation sample is normalized to the nominal $t\bar{t}$ cross-section so as to make this a shape-only uncertainty. The estimated uncertainty varies as a function of $M_{t\bar{t}}$ between 10 and 20%.

The choice of a PDF set used to simulate the production of SM $t\bar{t}$ events also impacts the shape of the predicted $M_{t\bar{t}}$ distribution. The uncertainty is estimated by taking the extremum of the variations in the shape of the $M_{t\bar{t}}$ distribution resulting from the use of different PDF sets and their associated uncertainties, as advocated by the PDF4LHC group [91]. The shape of the $M_{t\bar{t}}$ distribution obtained from all these variations is normalized to the nominal $t\bar{t}$ cross-section so as to not double count systematics effects already included in the cross-section uncertainty described above. The uncertainty on the shape of the $t\bar{t}$ distribution associated to the choice of a PDF set ranges from 5-10% at $M_{t\bar{t}} \approx 1$ TeV to more than 50% for reconstructed masses

---

[3] The renormalization scale is the energy scale at which α_s is computed.

[4] The factorization scale is the energy scale above which perturbative QCD calculations can take place. It stems from factorization theorems which allow to consider non-perturbative and perturbative effects independent of each other in a calculation (i.e. both effects can be factorized).

above 2.5 TeV. Large values of $M_{t\bar{t}}$ are affected by large uncertainties associated with the PDF of gluons carrying a large fraction of the proton's momentum. The gluon PDF has the largest uncertainties of all parton distributions in this kinematic regime.

An uncertainty on the predicted value of the $t\bar{t}$ cross-section due to missing contributions from electroweak radiation in the calculations is considered. The size of electroweak virtual corrections computed in [92] for top quark pair production is taken as an indication of the size of the total electroweak radiation corrections[5] and taken as a systematic uncertainty. The size of this correction increases with $M_{t\bar{t}}$ from a few percent to reach $\sim 10\%$ for masses above 2 TeV.

The uncertainty associated with the choice of the parton shower and hadronisation models is estimated from simulated event samples generated using the POWHEG-BOX program [93, 94] and interfaced[6] to PYTHIA or HERWIG. The uncertainty is taken as the relative difference between the two variations (with respect to the mean of the two variations). The uncertainty varies as a function of $M_{t\bar{t}}$ from a few percent to approximately 20% in a few bins of the $M_{t\bar{t}}$ distribution.

The uncertainty associated with the modeling of the initial- and final-state (QCD) radiation[7] was determined from MC samples produced with ACERMC+PYTHIA

---

[5] Which includes the contribution from real radiation of electroweak bosons (i.e. "real" corrections).

[6] For the showering, hadronisation and underlying event simulation.

[7] Energetic QCD radiation off one of the final-state partons may increase the reconstructed mass of a jet for instance.

with variations in the parameters controlling the simulation of the radiation. Two such samples are generated and the uncertainty is taken as half the relative difference between the two variations. The uncertainty varies on average between 5-10% over the range of reconstructed $M_{t\bar{t}}$ values considered.

6.2.2 W+jets production

The precise knowledge of the W+jets background normalization, inferred directly from data, is primarily limited by the available data statistics. An uncertainty of 20% is associated with the normalization of this background [59].

An uncertainty on the shape of the predicted W+jet distribution is also considered. It is estimated by changing the parametrization in ALPGEN of the renormalization and factorization scales used in the simulation of events with the ALPGEN generator [51]. The minimum parton p_{T} as defined by ALPGEN is also changed from its default value. The resulting distributions are normalized to the nominal event yield so as to preserve the overall (data-driven) normalization. They were then symmetrized around the nominal distribution (so as to provide both "up" and "down" variations) and added together in quadrature on a bin-by-bin basis. The combined effect on the shape of the distribution is largest at high values of reconstructed $M_{t\bar{t}}$ where it reaches $\sim 20\%$. The shape-only uncertainty associated with the choice of factorization and renormalization scales per se were found to be small and covered by the aforementioned shape uncertainty and was thus neglected.

Other possible sources of theoretical uncertainty such as the impact of the choice of the parton shower and hadronisation models, the choice of a PDF set, and the

modeling of the initial- and final-state radiation, are found to be sub-dominant components of the total uncertainty for $t\bar{t}$ events. Because the W+jets events already form a sub-leading contribution to the total expected background, these uncertainties were neglected. The estimated statistical uncertainty due to the finite size of the W+jets Monte Carlo sample has furthermore a large relative contribution ($> 20\%$, in any individual bin) to the total uncertainty for W+jets events.

6.2.3 Signal expectations

Only shape uncertainties are relevant for the signal distributions since the signal cross-section is taken as a free parameter that is eventually to be measured. No theoretical uncertainties were considered as none were found to significantly alter the expected shape of the signal distributions.

Next-to-leading order QCD corrections can affect the shape of the generated signal $M_{t\bar{t}}$ distribution[8] [64]. For instance, at NLO, an energetic gluon can radiate off one of the top quarks and shift the $M_{t\bar{t}}$ to a lower value, broadening the resonance peak. This effect is more prominent at large values of the generated signal mass but is significantly reduced by the large experimental resolution. Part of this effect is included in the simulation of the final-state radiations (in the parton shower). No further attempt was therefore made to account for this effect.

Other theoretical uncertainties affecting the shape of the $M_{t\bar{t}}$ distribution (such as the choice of parton shower and hadronisation models, and the modeling of the

---

[8] In the present work, the signal distributions are calculated at leading order in QCD.

intial- and final-state radiation) were found to be negligible with respect to uncertainties associated with the physics object reconstruction (e.g. jet reconstruction). These uncertainties were thus ignored for the signal distributions.

The shape uncertainty associated with the PDF set used in the simulation is much smaller for signal processes than for Standard Model $t\bar{t}$ production and was therefore neglected. This is in large part due to the fact that signal events are expected to be produced only via quark-antiquark annihilation while SM $t\bar{t}$ events are predominantly produced via the gluon fusion mechanism. The much smaller uncertainty on the quark (and antiquark) parton distribution functions (as compared to the gluon distribution function) therefore translates into a much smaller uncertainty on $M_{t\bar{t}}$ due to the choice of PDF set used in the simulation.

6.3 Luminosity

The total number of expected events, for both background and signal processes, is directly proportional to the integrated luminosity of the analyzed data sample as described in Eq. 3.1. The uncertainty inherent to the luminosity calculation thus affects the precision to which the overall normalization of the $M_{t\bar{t}}$ distribution can be predicted. The uncertainty on the luminosity measurement is 3.9%[95]. This value is taken as an uncertainty on the normalization of the $M_{t\bar{t}}$ distribution for each MC

Table 6–1 summarizes the different types and approximate size of all the systematic uncertainties considered in this analysis.

Systematic uncertainties channel	total bkg. (%)		SM $t\bar{t}$ (%)		W+jets (%)		Others (%)		Z' (%)		g_{KK} (%)	
sample	e	μ	e	μ	e	μ	e	μ	e	μ	e	μ
Object reconstruction	13	13	12	13	26	20	20	16	6	6	6	6
Event Simulation												
$t\bar{t}$ normalization	9	9	11	11	-		-		-		-	
NLO scale correction (shape)	11	11	13	13	-		-		-		-	
PDF (shape)	7	7	8	8	-		-		-		-	
Missing electroweak radiations	5	5	6	6	-		-		-		-	
Parton shower/hadronization models	8	6	8	7	-		-		-		-	
Initial/final-state radiations	4	3	4	3	-		-		-		-	
W+jets normalization	2	2	-		20	20	-		-		-	
ALPGEN parametrizations	1	1	-		14	11	-		-		-	
Luminosity	3	3	4	4	-		4	4	4	4	4	4
Total	23	23	25	25	36	31	21	26	7	7	7	7

Table 6–1: Impact of the different systematic uncertainties considered in this analysis on the background and signal (with a generated mass of 1.6 TeV) yields. The numbers correspond to a shift calculated in percent with respect to the nominal yield after the full event selection. They are estimated by the maximum shift between the "up" and "down" variations for each source of systematic uncertainty. The bottom line corresponds to the quadratic sum of all shifts. The uncertainties associated with the object reconstruction and luminosity are treated as being fully correlated among the Monte Carlo samples.

---

[9] With the exception of the W+jets background for which the overall normalization of the $M_{t\bar{t}}$ distribution is obtained directly from data.

CHAPTER 7
Results

In this chapter, the reconstructed $t\bar{t}$ invariant mass distribution, obtained from selected events in which both a semi-leptonic top decay and a hadronic top decay were successfully identified, is compared to the Standard Model predictions. The compatibility of the observed distribution with the expected background distribution is then assessed using a statistical hypothesis test.

7.1 Comparison between data and expected background

After all selection criteria have been applied, a total of 269 events are observed in the data sample in comparison with 309 ± 69 events predicted by Standard Model processes. The observed number of events is within one standard deviation of the total expected number of events and is thus statistically compatible. Table 7–1 lists the event yields separately for the e + jets and μ + jets final states and for the different background sources that were considered in the analysis.

Figure 7–1 shows the reconstructed $M_{t\bar{t}}$ distribution after the final selection of events. In the e + jets channel, a deficit in the number of data events is observed for reconstructed $M_{t\bar{t}}$ values around 1.2 TeV. In the μ + jets channel, the expected distribution of events from SM processes describes well the observed distribution of data events.

112

Source	e + jets	μ + jets
$t\bar{t}$	134 ± 34	130 ± 33
W + jets	15 ± 6	16 ± 5
Others	9 ± 2	5 ± 1
Total	158 ± 37	151 ± 35
Data	126	143

Table 7–1: Event yields after the final selection for the different expected background sources as well as the observed number of events in data. Background processes categorized in *others* are detailed in Section 5.6. The total uncertainty on the event yields expected from SM processes consists of the statistical uncertainty of the MC samples added in quadrature with the total systematic uncertainty.

For each bin of the histogram, the statistical significance of the difference between the observed number of data events and the predicted number of events from SM processes is shown. This significance is calculated according to the prescription described in [96]. In each bin, the probability of finding a deviation as important as or greater than the one observed in the analyzed data sample, the "p-value", is calculated (exactly) under the assumption that the data follows a Poisson distribution. The p-value is then converted into units of standard deviations of a Gaussian distribution, the "z-value", using the following formula [96]:

$$p\text{-value} = \int_{z\text{-value}}^{\infty} \frac{1}{\sqrt{2\pi}} e^{\frac{-x^2}{2}} \, dx. \tag{7.1}$$

It is this z-value that is plotted for each bin[1] . In the case of a deficit in the observed number of data events, the negative of the z-value is plotted for visualization

---

[1] As proposed in [96], the z-value is not plotted if the p-value is bigger than 0.5.

purposes. Incorporating the total uncertainty on the expected background into the calculation leads to a decrease of the observed statistical significance, as expected.

The statistical significance of the deficit of data events in the e+jets channel at around $M_{t\bar{t}} \approx 1.2$ TeV is at most $\sim 1.1\sigma$ in any individual bin. Several studies were performed to understand the origin of this small observed deficit of data. These studies suggest that the observed deviation between data and the expected background is consistent with a statistical fluctuation and is treated as such in the remaining of this thesis. Example of plots used to study this effect can be found in Appendix C.
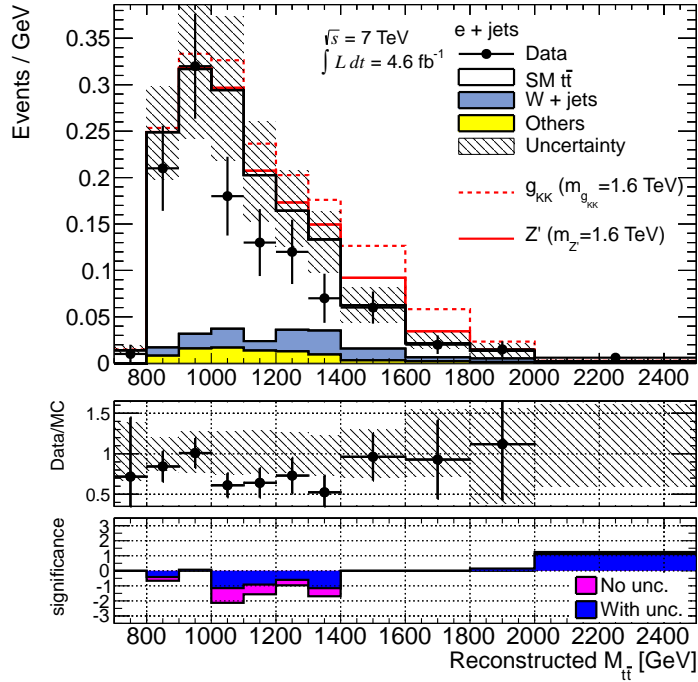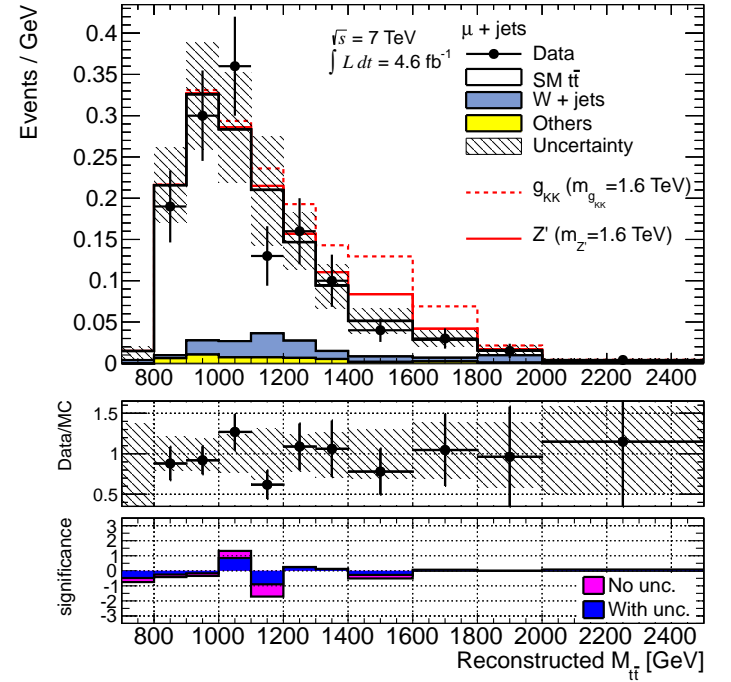
Figure 7–1: Reconstructed $M_{t\bar{t}}$ in the e+jets (a) and the μ+jets (b) channels, after the final selection of events. The number of events in each bin is divided by the corresponding bin width. The uncertainty corresponds to the (bin by bin) quadratic sum of all sources of uncertainties (including the statistical uncertainty of the MC samples) considered in the analysis. The statistical significance of the difference between data and the predicted background is shown in the bottom inset (see text). Hypothetical signals (a Z' with $\mathrm{m}_{Z'} = 1.6$ TeV and a g_{KK} with $\mathrm{m}_{g_{KK}} = 1.6$ TeV) are shown on top of the expected Standard Model background.

7.2 Hypothesis testing

The first step in the search for new physics phenomena is to establish the level of compatibility of the observed $M_{t\bar{t}}$ distribution with the Standard Model background-only (null) hypothesis. This can be assessed with a hypothesis test.

When quantifying the consistency of observed data with a hypothesis, a "test statistic" t needs to be constructed. The test statistic is a number that quantifies the difference between the observations and the predictions; the larger the value of t, the more discrepant the data are with respect to the hypothesis. The probability of observing a deviation at least as large as the one observed in the actual data, assuming the hypothesis is true, is presented as a so-called "p-value". The p-value depends on the probability density distribution of the data and can be calculated either analytically or by means of pseudo-experiments. In the latter case, several pseudo-data samples are generated by applying random fluctuations to the hypothesis. The value of the test statistic is computed for each of these pseudo-experiments and the p-value is then estimated as the fraction of pseudo-experiments for which the value of the test statistic t is larger than the observed one t_0 (that is computed with the actual data). The p-value ranges between 0 and 1 and it is common to translate it into equivalent units of standard deviations (σ) of a Gaussian distribution[2] .

The p-value of a hypothesis test is to be strictly speaking interpreted as a false-discovery probability. Given an observed p-value, one could declare the null hypothesis to be false, based on this hypothesis test, but would do so with a probability of

---

[2] That is, the p-value is converted into a z-value using Equation 7.1.

being wrong equal to the value of the observed p-value. Therefore, the smaller the p-value, the larger the statistical significance of a deviation between an observed and expected outcome of a measurement. "Evidence" for a discovery is usually claimed at 3σ which corresponds to a p-value of ~ 0.001, whereas discovery (which would mean rejecting the null hypothesis) is commonly claimed at 5σ (p-value of $\sim 3 \times 10^{-7}$).

The hypothesis test utilized in the present analysis is called BUMPHUNTER [97] and is designed to be sensitive to local excesses (bumps), or deficits (dips), of data in a distribution.

As a first step, the consistency of the data with the expectation is assessed locally in different regions of the distribution of interest (here, the reconstructed $M_{t\bar{t}}$ distribution) by means of a local p-value calculated analytically. Each region consists in a certain number of consecutive bins in the distribution. The p-value$^{\text{local}}$ is given by the Poisson cumulative distribution function (see [97] for more details). The hypothesis test is configured to look specifically for excesses, or for deficits of data. It can also consider any kind of disagreement between the expected background and the data distributions. The three modes are mutually exclusive and they differ from each other by additional requirements made on the allowed values of p-value$^{\text{local}}$. When looking specifically for excesses, any deficits are considered as maximally uninteresting. The p-value$^{\text{local}}$ is therefore set to a value of 1 if the number of observed events is smaller than the expected number of background events in the studied region. Similary, when looking for deficits, p-value$^{\text{local}}$ is set to unity in the case of an excess. When making no distinction between an excess and a deficit, that is when

looking simply for a deviation with respect to the expectation, no such additional requirement is applied on p-value$^{\text{local}}$.

Because, a priori, there is no preferred location in the distribution to look at, this local test is then repeated in different regions varying in size and location. The global test statistic t is then constructed from the results of the local tests performed in all regions of the distribution. It is defined as

$$t = -\log\left(p\text{-value}_{\min}^{\text{local}}\right),\tag{7.2}$$

where p-value$_{\min}^{\text{local}}$ is the smallest p-value obtained among all the local hypothesis tests (that is where the most disagreement with the expectation is observed). As such, BUMPHUNTER is referred to as a *hypertest* because it incorporates the results of many local tests, and thus naturally accounts for the trials factor (the so-called "look elsewhere effect" [98] [99]).

The BUMPHUNTER (global) p-value is then defined just as any other hypothesis test; it is the probability for the test statistic t defined in Equation 7.2 to be greater than the observed one calculated using the data, t_0, given the (Standard Model only) predictions. This is estimated using pseudo-experiments. Pseudo-experiments are generated by randomly fluctuating the expected Standard Model background according to Poisson statistics. The ensemble of pseudo-experiments gives rise to a distribution of test statistic values $\hat{f}(t)$ from which the p-value can be estimated as

$$p\text{-value} \approx \frac{\int_{t_0}^{\infty} \hat{f}(t)}{\int_0^{\infty} \hat{f}(t)}\tag{7.3}$$

In the context of this hypothesis test, if the observed p-value is large enough, then this indicates that the observed data distribution of interest is compatible with the distribution expected from Standard Model processes.

The effect of systematic uncertainties on the expected background distribution is included by allowing the background distribution to shift with respect to its nominal position so that a better agreement with data can be achieved (as quantified with p-value$^{\text{local}}$). A more detailed discussion of how this is technically performed can be found in Appendix B.

Tables 7–2(a) and 7–2(b) present the results of the BUMPHUNTER tests in each analysis channel obtained without and with taking into account systematic uncertainties, and under the three modes of operations of the test. The region in the $M_{t\bar{t}}$ distribution where the most significant data excess, deficit, or disagreement is observed is also indicated.

The error on the p-value is statistical and due to the fact that only a finite number of pseudo-experiments are generated. The p-value is converted to units of standard deviations (using Equation 7.1) with a corresponding range of values that accounts for the statistical error as propagated from the error on the p-value. It is to be noted that according to Equation 7.1, a negative number of standard deviations correspond to a p-value greater than 0.5. Also shown are the "combined" results for which the BUMPHUNTER test statistics values from each analysis channel are added if the corresponding regions of the distribution minimally overlap, otherwise the combined test statistic value is set to 0. This procedure for the combined results

119

Excesses			
Channel	p-value	σ (low, high)	region (GeV)
e + jets	0.762 ± 0.004	$-0.71 \ (-0.73, -0.70)$	$1800 - 2500$
μ + jets	0.877 ± 0.003	$-1.16 \ (-1.18, -1.15)$	$900 - 1100$
combined	no excess		
Deficits			
Channel	p-value	σ (low, high)	region (GeV)
e + jets	0.003 ± 0.001	$2.71 \ (2.65, 2.77)$	$1000 - 1400$
μ + jets	0.677 ± 0.005	$-0.46 \ (-0.47, -0.45)$	$1100 - 1600$
combined	0.009 ± 0.001	$2.35 \ (2.31, 2.39)$	$1100 - 1600$
Disagreement			
Channel	p-value	σ (low, high)	region (GeV)
e + jets	0.008 ± 0.001	$2.43 \ (2.39, 2.48)$	$1000 - 1400$
μ + jets	0.924 ± 0.003	$-1.47 \ (-1.49, -1.45)$	$1100 - 1600$

(a)

Excesses			
Channel	p-value	σ (low, high)	region (GeV)
e + jets	0.371 ± 0.005	$0.33 \ (0.32, 0.34)$	$1800 - 2500$
μ + jets	0.638 ± 0.005	$-0.35 \ (-0.37, -0.34)$	$900 - 1100$
combined	no excess		
Deficits			
Channel	p-value	σ (low, high)	region (GeV)
e + jets	0.370 ± 0.005	$0.33 \ (0.32, 0.34)$	$1200 - 1400$
μ + jets	0.598 ± 0.005	$-0.25 \ (-0.26, -0.23)$	$1100 - 1300$
combined	0.148 ± 0.004	$1.05 \ (1.03, 1.06)$	$1100 - 1300$
Disagreement			
Channel	p-value	σ (low, high)	region (GeV)
e + jets	0.136 ± 0.003	$1.10 \ (1.08, 1.12)$	$1000 - 1400$
μ + jets	0.910 ± 0.003	$-1.34 \ (-1.36, -1.32)$	$900 - 1100$

(b)

Table 7–2: The largest deviations in the reconstructed $M_{t\bar{t}}$ distribution found by the BUMPHUNTER test and their statistical significance. Only the statistical uncertainty on the expected background is considered in (a). Both statistical and systematic uncertainties on the expected background are taken into account in (b).

is motivated by the fact that a hypothetical $t\bar{t}$ resonance would give rise to an excess of events in the distribution of both channels in roughly the same region.

When accounting for systematic uncertainties, no statistically significant deviations from the Standard Model only hypothesis are observed. The expected background and data distributions agree in both channels well within the 3σ threshold (i.e. p-value $\gtrsim 0.001$). No local excess (bump) is found when considering both channels together, nor when considering channels individually. There is thus no evidence for the production of a new heavy particle decaying to a top and anti-top quark in the analyzed data sample.

CHAPTER 8
Constraints on theoretical models

Given the absence of evidence for the production of a new heavy particle decay-ing to a top and anti-top quark, upper limits on the production cross-section times branching ratio of new bosons are obtained for the two benchmark models under consideration, the Topcolor and Randall-Sundrum warped extra-dimension models. Limits are calculated using a Bayesian statistical inference method[1] which will be detailed below.

8.1 Limit calculation in the Bayesian framework

In this analysis, the expected number of events d is given by:

$$d = a\sigma + b \, , \tag{8.1}$$

where the parameters a, σ, and b are, respectively, the effective luminosity of the signal[2] , the signal cross-section[3] , and the expected yield from the (Standard Model)

---

[1] The original implementation of the method was provided by the DØ collaboration, according to the procedure described in [100].

[2] Which is equivalent to the signal acceptance multiplied by the integrated luminosity of the data sample: $a \equiv \epsilon\mathcal{L}$.

[3] The branching ratio to the $t\bar{t}$ final state is implicitly assumed ($\sigma \equiv \sigma_{g_{KK}, Z' \to X} \times \text{BR}$) and omitted for simplicity.

background processes. The compatibility of the observed number of events D with the expectation is encoded in the *likelihood* function of the data, given the statistical model for d. In a counting experiment, such as in the present case, the likelihood is taken to be a Poisson distribution with mean d. The probability of observing D events, given the expectation value d $(= a\sigma + b)$ is thus:

$$L(D|d) = \frac{e^{-d}d^{D}}{\Gamma(D+1)} = \frac{e^{-(a\sigma+b)}(a\sigma+b)^{D}}{\Gamma(D+1)} = L(D|a,b,\sigma) \qquad (8.2)$$

When considering counts in multiple (independent) bins, the total likelihood is defined as the product of the single-bin likelihoods:

$$L(\mathbf{D}|\mathbf{a},\mathbf{b},\sigma) = \prod_{i} L(D_{i}|a_{i},b_{i},\sigma) \ , \qquad (8.3)$$

where the index i runs over all bins of the $M_{t\bar{t}}$ distribution in both the e + jets and μ + jets analysis channels, and $\mathbf{D}$, $\mathbf{a}$ and $\mathbf{b}$ are vectors of the observed counts, the signal effective luminosities and the expected background yields, respectively.

According to Bayes' Theorem [101], the probability that the signal hypothesis describes the observations given the data (the *posterior* probability) is proportional to the likelihood function of the data multiplied by the *prior* probability (i.e. the *a priori* probability) of the signal hypothesis parameters:

$$P(\mathbf{a},\mathbf{b},\sigma|\mathbf{D}) \propto L(\mathbf{D}|\mathbf{a},\mathbf{b},\sigma)P(\mathbf{a},\mathbf{b},\sigma) \ , \qquad (8.4)$$

Because the signal cross-section is independent of any (prior) knowledge of the $\mathbf{a}$ and $\mathbf{b}$ parameters, the prior probability density can be factorized as : $P(\mathbf{a},\mathbf{b},\sigma) =$

$P(\mathbf{a}, \mathbf{b})P(\sigma)$. The signal cross-section prior is assumed here to be flat (i.e. constant) in σ and non-zero only for $\sigma > 0$.

The posterior probability density distribution as a function of signal cross-section, given the observed counts and irrespective of the $\mathbf{a}$ and $\mathbf{b}$ parameters, is obtained by means of integration:

$$P(\sigma|\mathbf{D}) = \iint P(\mathbf{a}, \mathbf{b}, \sigma|\mathbf{D}) \, d\mathbf{a} \, d\mathbf{b} = \frac{1}{\mathcal{N}} \iint L(\mathbf{D}|\mathbf{a}, \mathbf{b}, \sigma)P(\mathbf{a}, \mathbf{b})P(\sigma) \, d\mathbf{a} \, d\mathbf{b} \, , \quad (8.5)$$

where $\mathcal{N}$ is a normalization constant defined such that $\int_0^\infty P(\sigma|\mathbf{D})d\sigma = 1$. The 95% credibility level (CL) upper limit on the signal production cross-section times branching ratio ($\sigma_{95\%}$) then corresponds to the value for which the integral of the posterior probability density is equal to 0.95:

$$\int_0^{\sigma_{95\%}} P(\sigma|\mathbf{D}) \, d\sigma = 0.95 \quad (8.6)$$

When uncertainties on the signal effective luminosities and background yields are ignored, the prior knowledge of $\mathbf{a}$ and $\mathbf{b}$, which is encoded in the prior probability density, is given (exactly) by the estimated nominal values $\mathbf{a}_0$ and $\mathbf{b}_0$: $P(\mathbf{a}, \mathbf{b}) = \delta(\mathbf{a} - \mathbf{a}_0)\delta(\mathbf{b} - \mathbf{b}_0)$. The posterior for the cross-section $P(\sigma|\mathbf{D})$ is thus directly proportional to the likelihood $L(\mathbf{D}|\mathbf{a}_0, \mathbf{b}_0, \sigma)$. The next section describes how uncertainties on $\mathbf{a}_0$ and $\mathbf{b}_0$ are incorporated in the prior $P(\mathbf{a}, \mathbf{b})$.

8.1.1 Treatment of systematic uncertainties

The systematic uncertainties are taken into account by smearing the distributions of probable values of $\mathbf{a}$ and $\mathbf{b}$ such that they become Gaussian distributed

around the nominal values $\mathbf{a}_0$ and $\mathbf{b}_0$. The prior $P(\mathbf{a}, \mathbf{b})$ is therefore modeled as a composition of several Gaussians with standard deviations estimated from the $\pm 1\sigma$ systematics variations.

The effects of the systematic uncertainties are implemented in the limit calculation by applying random Gaussian shifts to the estimated nominal values $(\mathbf{a}_0, \mathbf{b}_0)$ for each individual source of systematic uncertainty. The same shift is applied to all bins of both analysis channels (for both the background and signal expectations) for each systematic uncertainty[4] . More precisely, given the estimated $\pm 1\sigma$ variation of one source of systematic uncertainty $(\mathbf{a}_{\pm 1\sigma}^{sys}, \mathbf{b}_{\pm 1\sigma}^{sys})$, and a random number sampled from a Gaussian distribution with mean 0 and unit variance $g(0, 1)_{sys}$, a new vector $(\mathbf{a}', \mathbf{b}')$ is constructed as:

$$(\mathbf{a}', \mathbf{b}') = (\mathbf{a}_0, \mathbf{b}_0) + \sum_{sys} (\Delta \mathbf{a}_{sys}, \Delta \mathbf{b}_{sys}) \ , \tag{8.7}$$

where $\Delta \mathbf{x}_{sys}$ is the random gaussian shift for systematic sys:

$$\Delta \mathbf{x}_{sys} = g(0, 1)_{sys} \times \begin{cases} \left(\mathbf{x}_{+1\sigma}^{sys} - \mathbf{x}_0\right) \ , & \text{if} \quad g(0, 1)_{sys} \geq 0 \\ \left(\mathbf{x}_0 - \mathbf{x}_{-1\sigma}^{sys}\right) \ , & \text{if} \quad g(0, 1)_{sys} < 0 \ . \end{cases} \tag{8.8}$$

Each vector constructed as such is thus randomly sampled from the prior probability density function $P(\mathbf{a}, \mathbf{b})$. This allows us to perform the integration in equation 8.5 numerically through the Monte Carlo importance sampling method; the posterior

---

[4] With the exception of the uncertainty coming from the limited statistical size of the Monte Carlo simulated samples for which a different random shift is applied to each bin.

can therefore be estimated as:

$$P(\sigma|\mathbf{D}) \approx \frac{P(\sigma)}{\mathcal{N}K} \sum_{k=1}^{K} L(\mathbf{D}|\mathbf{a}'_k, \mathbf{b}'_k, \sigma) \ , \tag{8.9}$$

where, K points are randomly sampled from $P(\mathbf{a}, \mathbf{b})$, the prior for the $\mathbf{a}$ and $\mathbf{b}$ parameters.

8.1.2 Data ensembles and expected limit

The 95% CL upper limit on the signal cross-section times branching ratio derived from the data counts $\mathbf{D}$ is referred to as the *observed* limit. The *expected* limit, on the other hand, is obtained by replacing the observed data counts with pseudo-data corresponding to the expected background yield $\mathbf{b}$. Pseudo-data are generated by repeatedly fluctuating the expected background yield $\mathbf{b}$ according to a Poisson distribution in each bin. The ensemble of pseudo-data is used to obtain a distribution of limits. The expected limit is defined as the median of this distribution. The $\pm 1\sigma$ ($\pm 2\sigma$) uncertainty on the expected limit is defined as the values of cross-section times branching ratio which encompass 68% (95%) of the limit distribution.

8.2 Limits on the existence of new heavy particles

Using data events selected according to the criteria detailed in Chapter 5, as well as estimations of the total background and signal expectations as described in Section 5.6, upper limits on the cross-section times branching ratio are obtained following the procedure described in Section 8.1.

The 95% CL upper limits on the cross-section times branching ratio as a function of the hypothetical particle mass are summarized in Tables 8–1 and 8–2 for Z' and g_{KK} signals, respectively. Limits are calculated assuming different values of Z' (g_{KK}) mass in the range 0.8-2.5 TeV (0.8-2.0 TeV). The observed limit values are generally lower than the expected ones when omitting systematic uncertainties. This behavior is due to the the slight deficit in the number of observed data counts with respect to the expectation. When accounting for systematic uncertainties however, the observed limits lie within one σ of the expected limit for practically all mass points, for both the Z' and the g_{KK}. This result is consistent with the compatibility of the observed $M_{t\bar{t}}$ distribution with the expected distribution as assessed in the previous chapter.

Figures 8–1 and 8–2 present the upper limits for the Z' and g_{KK} bosons, respectively, as a function of the generated boson mass[5] . The expected theoretical cross-section times branching ratio is also shown for both types of signal. The difference in the shape of the limit curve between the two types of signal is attributable to their different mass widths (the Z' is a narrow resonance, whereas the g_{KK} is a wide resonance) which affect the predicted signal distributions. The rise of the limit at low values of $M_{t\bar{t}}$ is due to a lower signal efficiency as a lesser amount of top decays are boosted enough to satisfy the boosted top quark identification criteria.

The hypothetical particle is excluded to exist, at any given mass, whenever the observed limit on the cross-section times branching ratio is lower that the theoretical prediction. When considering systematic uncertainties, the observed limits exclude

---

[5] Interpolating linearly between the masses at which a limit is calculated.

at 95% CL Z' bosons from the Topcolor model in the mass range 0.85-1.65 TeV as well as Kaluza-Klein gluons from the Randall-Sundrum model in the mass range 0.8-1.88 TeV.

Z' Mass	Statistical				Statistical + Systematics			
	Obs.	Exp.			Obs.	Exp.		
[TeV]	[pb]	[pb]	$+1\sigma$ [pb]	-1σ [pb]	[pb]	[pb]	$+1\sigma$ [pb]	-1σ [pb]
0.80	1.4	2.2	3.1	1.6	3.6	3.3	5.2	2.1
1.00	0.20	0.30	0.42	0.22	0.65	0.52	0.77	0.36
1.30	0.060	0.11	0.16	0.081	0.13	0.17	0.24	0.12
1.60	0.044	0.060	0.084	0.043	0.070	0.086	0.128	0.060
2.00	0.042	0.035	0.049	0.025	0.063	0.043	0.064	0.030
2.50	0.029	0.024	0.035	0.018	0.037	0.029	0.041	0.021

Table 8–1: Cross-section times branching ratio 95% CL upper limits on a leptophobic Z' boson, from the Topcolor model, decaying to a $t\bar{t}$ pair. Observed (Obs.) and expected (Exp.) limits are quoted both without and with systematics uncertainties taken into account. The $\pm 1\sigma$ uncertainty on the expected limits is also shown.

8.3   Comparisons with existing constraints

Several searches for $t\bar{t}$ resonances were performed at the Tevatron and more recently at the LHC. The CDF [102, 103] and DØ [104] collaborations have both set exclusion limits on leptophobic Topcolor Z', using an integrated luminosity of approximately 5 fb^{-1}; the most stringent limit excludes at 95% CL Z' bosons with mass below 900 GeV.

| g_{KK} Mass | Statistical | | | | Statistical + Systematics | | | |
| | Obs. | Exp. | | | Obs. | Exp. | | |
[TeV]	[pb]	[pb]	$+1\sigma$ [pb]	-1σ [pb]	[pb]	[pb]	$+1\sigma$ [pb]	-1σ [pb]
0.80	0.95	1.5	2.1	1.1	2.0	2.0	3.0	1.4
0.90	0.44	0.73	1.02	0.53	0.97	1.0	1.6	0.75
1.00	0.24	0.39	0.55	0.28	0.97	0.76	1.2	0.50
1.15	0.11	0.23	0.32	0.16	0.62	0.52	0.76	0.34
1.30	0.081	0.17	0.24	0.12	0.22	0.29	0.41	0.20
1.60	0.063	0.092	0.130	0.067	0.11	0.14	0.21	0.095
1.80	0.062	0.073	0.102	0.053	0.14	0.12	0.18	0.077
2.00	0.069	0.065	0.092	0.047	0.13	0.094	0.14	0.063

Table 8–2: Cross-section times branching ratio 95% CL upper limits on a g_{KK} boson decaying to a $t\bar{t}$ pair. Observed (Obs.) and expected (Exp.) limits are quoted both without and with systematics uncertainties taken into account. The $\pm1\sigma$ uncertainty on the expected limits is also shown.

The CMS[6] collaboration [105, 87] excluded at 95% CL a narrow Z' in the mass range $0.5 - 1.5$ TeV, and a g_{KK} in the range $1.0 - 1.82$ TeV (in pp collisions at $\sqrt{s} = 7$ TeV).

Results presented in this thesis therefore constitute some of the most stringent limits on the existence of a leptophobic Z' boson and a Kaluza-Klein gluon.

Recent results from ATLAS [59] using the full 2011 dataset (4.7 fb^{-1} at $\sqrt{s} = 7$ TeV) exclude leptophobic Topcolor Z' for masses in the range $0.5 - 1.74$ TeV and g_{KK} for masses in the range $0.7 - 2.07$ TeV. In those results, both the resolved[7] and the boosted topology are considered. This combination increases the search

---

[6] CMS is the other "general-purpose" detector at the LHC.

[7] The resolved topology refers to events in which all the decay products of the hadronically decaying top quark can be resolved by individual jets.

sensitivity, mostly at low values of $M_{t\bar{t}}$, with respect to a boosted-only analysis. A different and less stringent selection is also employed to maximize the signal efficiency, at the expense of a larger background. The presence of a jet initiated by a b quark is also required to reduce the contribution of the reducible backgrounds (such as QCD multijet and W + jets events). This approach is to be contrasted with the one adopted in the present analysis, where a more sophisticated and strict selection relying on the jet substructure is used in order to compensate for the absence of an explicit requirement on the presence of a b quark (so-called b-tagging). The results presented herein achieve comparable search sensitivities in the boosted-only topology.

Recent preliminary results for searches for $t\bar{t}$ resonances in the semi-leptonic final state using pp collisions at $\sqrt{s} = 8$ TeV were made available by both ATLAS [106] and CMS [107] experiments. Searches performed at the LHC with $\sqrt{s} = 8$ TeV benefit from a higher reach in $M_{t\bar{t}}$ thanks to the higher center-of-mass energy. Using 14.3 fb^{-1}, the ATLAS result excludes (at 95% CL) a leptophobic Z' boson in the mass range $0.5 - 1.8$ TeV, and a g_{KK} in the range $0.5 - 2.0$ TeV. The CMS result has slightly more stringent limits of $m_{Z'} < 2.1$ TeV and $m_{g_{KK}} < 2.5$ TeV thanks to a larger data sample (19.6 fb^{-1}) and a downward statistical fluctuation of the data at high masses.
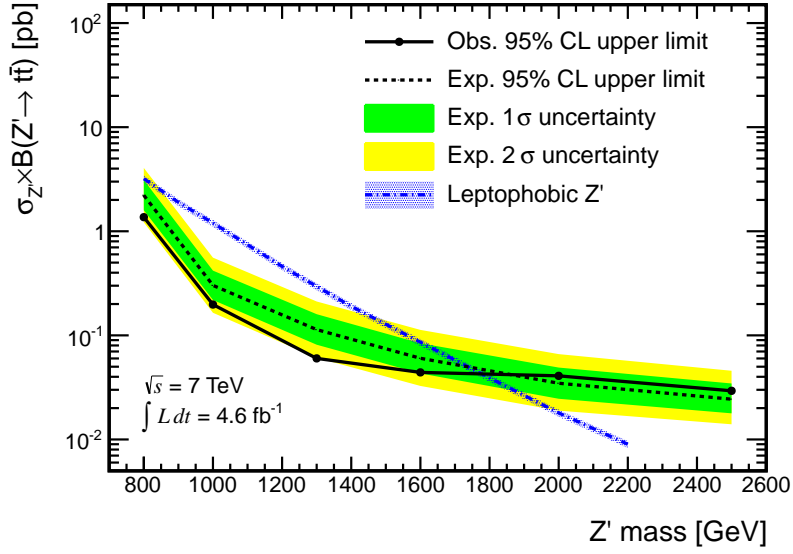
(a)
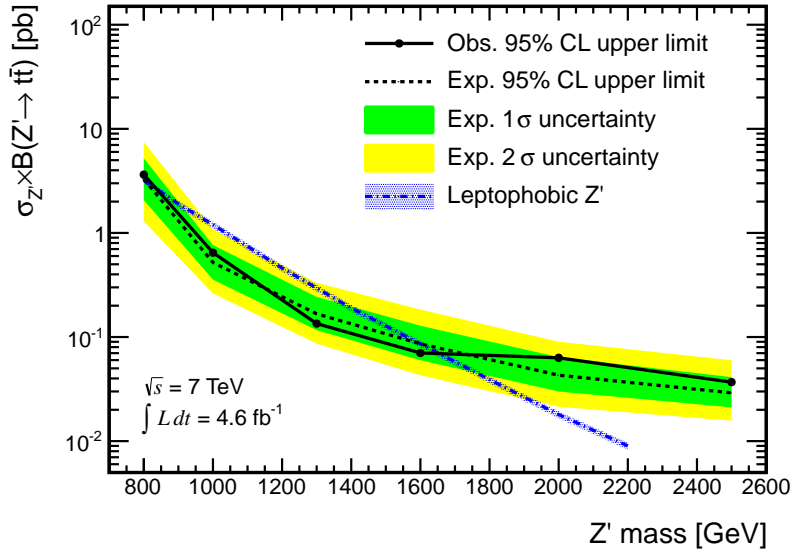
(b)

Figure 8–1: Cross-section times branching ratio 95% CL upper limits as a function of the mass of a leptophobic Z' boson from the Topcolor model. Statistical uncertainties only are considered in (a) whereas both statistical and systematic uncertainties are considered in (b).

131
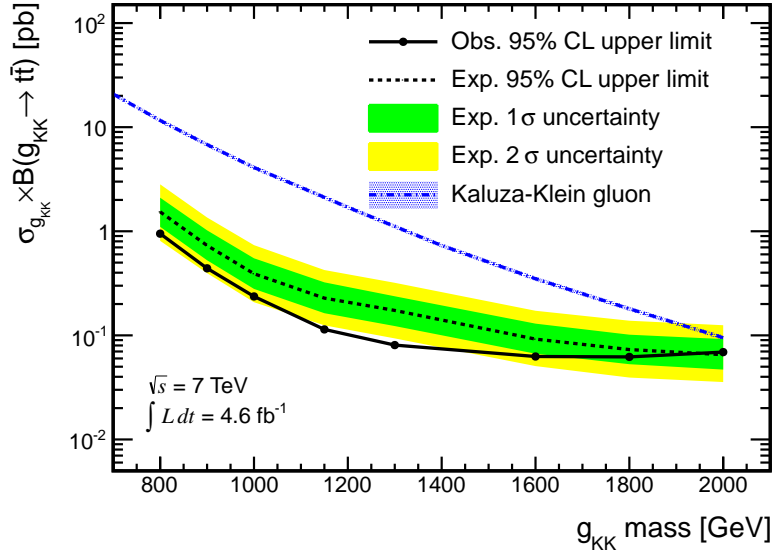
(a)
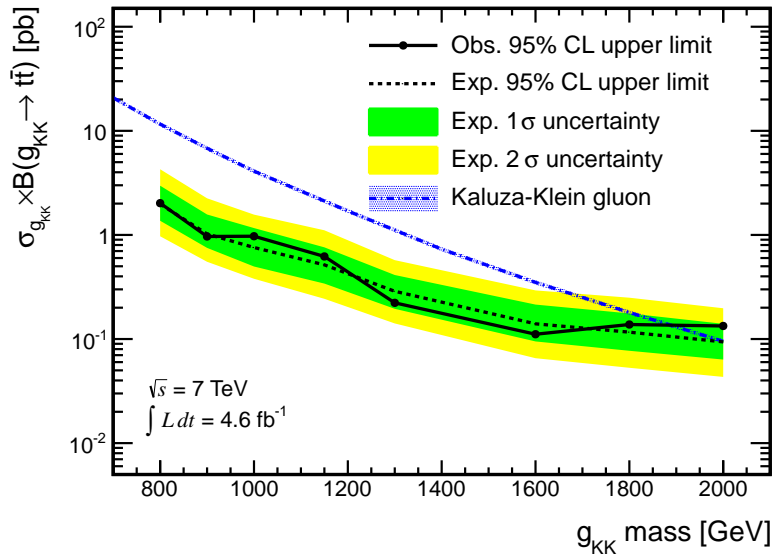

(b)

Figure 8–2: Cross-section times branching ratio 95% CL upper limits as a function of the mass of a g_{KK} boson from the Randall-Sundrum model. Statistical uncertainties only are considered in (a) whereas both statistical and systematic uncertainties are considered in (b).

CHAPTER 9
Conclusion

A search for a heavy particle decaying to a top-antitop ($t\bar{t}$) quark pair in the semi-leptonic final state was performed using proton-proton collisions at center-of-mass energy of 7 TeV. Data was collected in 2011 by the ATLAS detector at the LHC and amounted to an integrated luminosity of approximately 4.6 fb^{-1}.

The reconstruction of the $t\bar{t}$ invariant mass ($M_{t\bar{t}}$) required the development of dedicated identification and reconstruction techniques in order to identify top quarks produced with transverse momentum exceeding their intrinsic mass. To that end, a novel approach for reconstructing *boosted* top quarks decaying hadronically as a single large-R jet was presented. The study of the jet substructure was employed as a means to efficiently discriminate jets containing a genuine boosted top hadronic decay, from generic jets. The identification of leptonic top quark decays was also adapted to identify top quarks produced with large values of transverse momentum. An innovative lepton isolation requirement was used and distinctive kinematic properties of leptonic top decays were exploited in order to considerably reduce background contamination.

Excesses in the reconstructed $M_{t\bar{t}}$ distribution were searched for using the BUMPHUNTER test; no statistically significant deviations were found with respect to the Standard Model expectations. Upper limits on the cross-section times branching ratio were set on the production of a new particle decaying to $t\bar{t}$ in the context

of the Topcolor model (Z' leptophobic boson) and the Randall-Sundrum extra dimensions model (Kaluza-Klein gluon, g_{KK}). The observed 95% CL upper limit, set using a Bayesian method, varies between 3.6 pb (at $M_{Z'} = 0.8$ TeV) and 0.037 pb (at $M_{Z'} = 2.5$ TeV) for Z' bosons, and 2.0 pb (at $M_{g_{KK}} = 0.8$ TeV) and 0.13 pb (at $M_{g_{KK}} = 2.0$ TeV) for Kaluza-Klein gluons.

In light of these results, a leptophobic Z' boson is excluded to exist, at 95% CL, in the mass range 0.85-1.65 TeV. Likewise, a g_{KK} gluon is excluded, at 95% CL, in the mass range 0.8-1.88 TeV. The upper mass limits are more stringent than results obtained so far by other experiments and consistent with recent ATLAS results obtained using a different analysis approach.

The use of jet substructure to identify energetic top quarks is inevitable at the LHC. With the amount of data collected up to now and as this thesis has shown, it has been possible to achieve a good understanding of jet substructure with the ATLAS detector. In future analyses, search sensitivities could be greatly enhanced by making use of these techniques in a more sophisticated way. Exploiting, for instance, subtle correlations amongst substructure observables through a multi-variate classifier could help decrease even more the data sample contamination from reducible backgrounds and thus allow to reach better search sensitivities.

Appendices

APPENDIX A
Q_{visible} **derivation**

It is instructive to go through the straightforward derivation of the expected

invariant mass of the lepton $+ b$ quark system.

The four-momentum sum of the visible decay products, in the rest frame of the W

boson, is given by

$$p_{lb} \equiv p_l + p_b = \left(\frac{m_W}{2} + E_b, \ \frac{m_W}{2} \frac{\vec{p_l}}{|\vec{p_l}|} + \vec{p_b} \right), \tag{A.1}$$

where the lepton was assumed massless for simplicity. The invariant mass is thus

$$
\begin{aligned}
Q_{\text{visible}}^2 \equiv p_{lb} \cdot p_{lb} &= E_b m_W + E_b^2 - |\vec{p_b}|^2 - m_W \vec{p_b} \cdot \frac{\vec{p_l}}{|\vec{p_l}|} \\
&= E_b m_W + m_b^2 - m_W |\vec{p_b}| \cos \theta \\
&= \frac{m_t^2 - m_W^2 + m_b^2}{2} - m_W |\vec{p_b}| \cos \theta,
\end{aligned}
\tag{A.2}
$$

where θ is the angle between the lepton and b momenta, and the last simplification

is due to the constraint coming from the invariant mass of the top quark, $m_t^2 =$

$(m_W + E_b)^2 - |\vec{p_b}|^2 = m_W^2 + 2E_b m_W + m_b^2$. This also allows us to express $|\vec{p_b}|^2$ in

terms of the different masses involve:

$$
\begin{aligned}
|\vec{p_b}|^2 = E_b^2 - m_b^2 &= \left(\frac{m_t^2 - m_W^2 - m_b^2}{2m_W} \right)^2 - m_b^2 \\
&= \frac{(m_t^2 - m_W^2)^2}{(2m_W)^2} \left[1 - \frac{2m_b^2}{m_t^2 - m_W^2} - \frac{4m_b^2 m_W^2}{(m_t^2 - m_W^2)^2} \right] + \mathcal{O}\left(m_b^4\right) \quad \text{(A.3)} \\
&= \frac{(m_t^2 - m_W^2)^2}{(2m_W)^2} \left[1 - \frac{2m_t^2 + 2m_W^2}{(m_t^2 - m_W^2)^2} m_b^2 \right] + \mathcal{O}\left(m_b^4\right).
\end{aligned}
$$

It follows that in the small m_b limit,

$$
|\vec{p_b}| \approx \frac{m_t^2 - m_W^2}{2m_W} \left[1 - \frac{m_t^2 + m_W^2}{(m_t^2 - m_W^2)^2} m_b^2 \right], \tag{A.4}
$$

and therefore,

$$
Q_{\text{visible}}^2 \approx \frac{m_t^2 - m_W^2 + m_b^2}{2} - \left[\frac{m_t^2 - m_W^2}{2} - \frac{m_t^2 + m_W^2}{2\left(m_t^2 - m_W^2\right)} m_b^2 \right] \cos\theta. \tag{A.5}
$$

The expected range of kinematically allowed Q_{visible}^2 values is thus $(\cos\theta \to \pm 1)$

$$
\frac{m_t^2 m_b^2}{m_t^2 - m_W^2} \lesssim Q_{\text{visible}}^2 \lesssim m_t^2 - m_W^2 + \mathcal{O}\left(m_b^2\right), \tag{A.6}
$$

in accordance with [83]. Although Q_{visible} can take small values, it peaks at a value just past 100 GeV [1] for leptonic top decays whereas a much smaller value is to be expected for heavy flavor jets with an accompanying soft and almost collinear lepton.

---

[1] That is assuming a distribution of $\cos\theta$ in agreement with the expected polarization states of the W boson. See [108].

APPENDIX B
BumpHunter with systematics

BUMPHUNTER's test statistic is computed from many local hypothesis tests. For each of these local tests, the deviation of the observed data with respect to the expectation is assessed and quantified using a local p-value. The (global) test statistic is then defined as the negative of the logarithm of the smallest local p-value, denoted as p-value$_{\text{min}}^{\text{local}}$.

Since the expected background distribution is only known within some uncertainty, systematic errors can reduce the significance of a deviation observed in data. There is no standard prescription as to how to incorporate systematic uncertainties into the hypothesis test. For simplicity, a single nuisance parameter λ is defined and indicates by how many σ (of the total uncertainty[1]) the background is varied (uniformly and coherently for all bins). The background is thus allowed to shift from its nominal position in order to improve the agreement with data. That is to say that p-value$_{\text{min}}^{\text{local}}$ is maximized as a function of λ. Under the assumption that the number of background events and its total systematic uncertainty can be modeled by a Gaussian distribution, the probability of a shift λ should follow a Gaussian

---

[1] The systematic errors are combined, in each bin, by adding in quadrature the maximum of the "up" and "down" shifts from the different sources of uncertainties considered in the present work.

138

distribution. This last requirement can be satisfied by maximizing :

$$p\text{-value}_{\text{min}}^{\text{local}} \times G(0,1)(\lambda) = p\text{-value}_{\text{min}}^{\text{local}} \times \frac{1}{\sqrt{2\pi}} e^{-\lambda^2/2} \ . \tag{B.1}$$

This is equivalent to maximizing:

$$-t - \lambda^2/2 \equiv R(\lambda) \ , \tag{B.2}$$

where t is BUMPHUNTER's test statistic ($p\text{-value}_{\text{min}}^{\text{local}} = e^{-t}$).

When dealing with large systematics and when looking specifically for excesses or deficits, it can happen that the most favored λ found (by maximizing R) is such that $t = 0$ (and hence BUMPHUNTER's p-value $= 1$). This is due to the Gaussian *penalty factor* not being restrictive enough to prevent large shifts of the background covering all deviations with the data. To avoid such situations, R is maximized under the condition that $t \neq 0$.

B.1   Injected signal

Tables B–1(a) and B–1(b) present the results of the BUMPHUNTER test when simulated signal distributions (shown in Figure 7–1) are deliberately added to the observed data distribution.

The Z' has a small predicted cross-section (0.086 pb at $m_{Z'} = 1.6$ TeV) and its effect on the $M_{t\bar{t}}$ distribution is barely significant when accounting for systematics. Indeed, as shown in Table B–1(a), a 1.2σ excess (located in the correct mass region) is found when combining both channels. Further investigations would have been necessary to conclude on the nature of such an excess.

The g_{KK} has a much higher predicted cross-section (0.35 pb at $m_{g_{KK}} = 1.6$ TeV) and its hypothetical presence in the observed distribution is in this case unambiguous. As presented in Table B–1(b), an excess of over 3σ is located again in the correct mass interval.

Excesses			
Channel	p-value	σ (low, high)	region (GeV)
e + jets	0.301 ± 0.005	$0.52\ (0.51, 0.53)$	$1400 - 1800$
μ + jets	0.381 ± 0.005	$0.30\ (0.29, 0.32)$	$1400 - 1800$
combined	0.114 ± 0.003	$1.21\ (1.19, 1.22)$	$1400 - 1800$
Deficits			
Channel	p-value	σ (low, high)	region (GeV)
e + jets	0.325 ± 0.005	$0.45\ (0.44, 0.47)$	$1000 - 1200$
μ + jets	0.718 ± 0.004	$-0.58\ (-0.59, -0.56)$	$800 - 900$
combined	no deficit		
Disagreement			
Channel	p-value	σ (low, high)	region (GeV)
e + jets	0.009 ± 0.001	$2.38\ (2.34, 2.42)$	$1400 - 2500$
μ + jets	0.595 ± 0.005	$-0.24\ (-0.35, -0.23)$	$1100 - 1300$

(a)

Excesses			
Channel	p-value	σ (low, high)	region (GeV)
e + jets	0.004 ± 0.001	$2.66\ (2.61, 2.72)$	$1400 - 1800$
μ + jets	0.002 ± 0.001	$2.89\ (2.81, 2.96)$	$1400 - 1800$
combined	0.0001 ± 0.0001	$3.7\ (3.5, 5.7)$	$1400 - 1800$
Deficits			
Channel	p-value	σ (low, high)	region (GeV)
e + jets	0.283 ± 0.004	$0.58\ (0.56, 0.59)$	$1000 - 1200$
μ + jets	0.435 ± 0.005	$0.16\ (0.15, 0.18)$	$800 - 1000$
combined	no deficit		
Disagreement			
Channel	p-value	σ (low, high)	region (GeV)
e + jets	0.0003 ± 0.0002	$3.4\ (3.3, 3.7)$	$1400 - 2500$
μ + jets	0.003 ± 0.001	$2.77\ (2.71, 2.84)$	$1400 - 1800$

(b)

Table B–1: The largest deviations in the reconstructed $M_{t\bar{t}}$ distribution with injected signal found by the BUMPHUNTER test and their statistical significance. The signal distribution for a Z' with $m_{Z'} = 1.6$ TeV is added to the data distribution in (a). The signal distribution for a g_{KK} with $m_{g_{KK}} = 1.6$ TeV is added to the data distribution in (b). Both statistical and systematic uncertainties on the expected background are taken into account.

APPENDIX C
Comparison between data and expected background

This appendix contains plots used to assess the agreement between data and the expected background in different kinematic regions and for different kinematic variables.

Figures C–1 and C–2 show the expected and observed jet mass and Q_W distributions, for both channels separately, before the selection criteria on those two observables are applied (i.e. $m_{\text{hadronic}}^{\text{top}} > 120$ GeV and $Q_W > 40$ GeV). The top mass and W mass peaks are observed in the Standard Model $t\bar{t}$ production although a slight deficit of data is observed in the e + jets channel. When taking systematic uncertainties into account, no deviations beyond a significance of $\sim 1\sigma$ is observed in any bin.

Figure C–3 presents the reconstructed mass of the leptonic top candidate, after the full selection but without the $m_{\text{leptonic}}^{\text{top}} > 120$ GeV requirement. Despite more significant deviations (which remain below 2σ), the expected background appears to describe the data reasonably well.
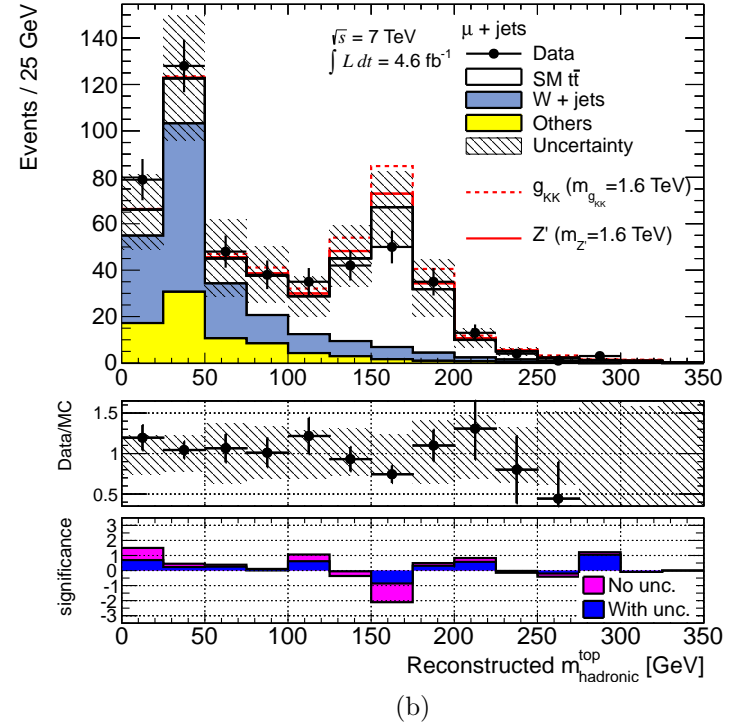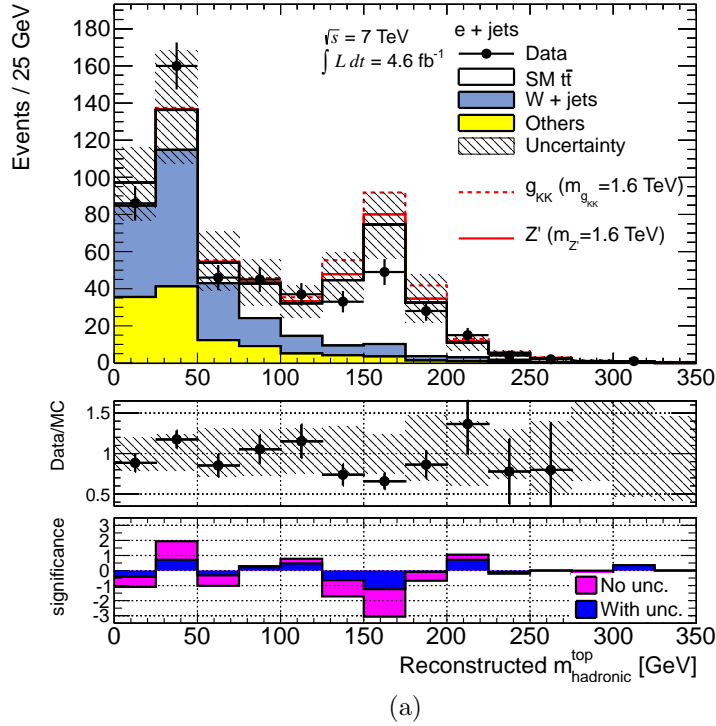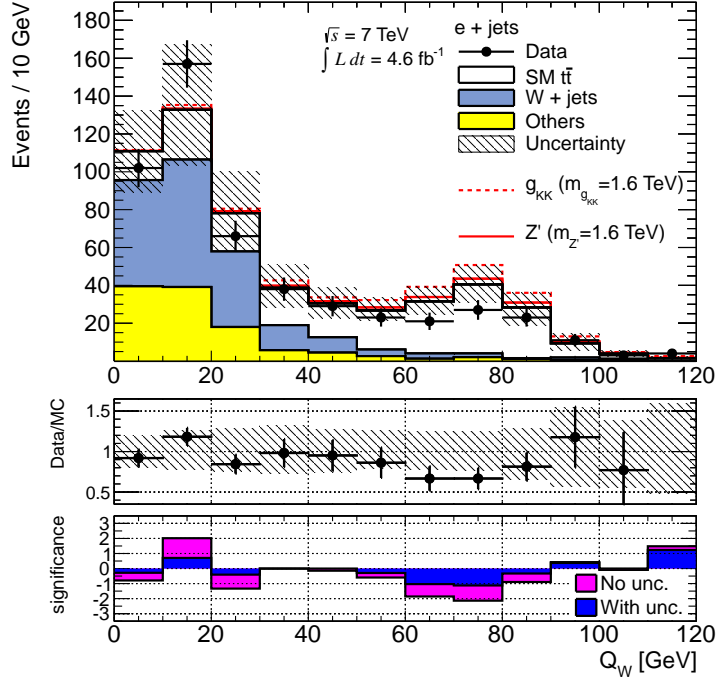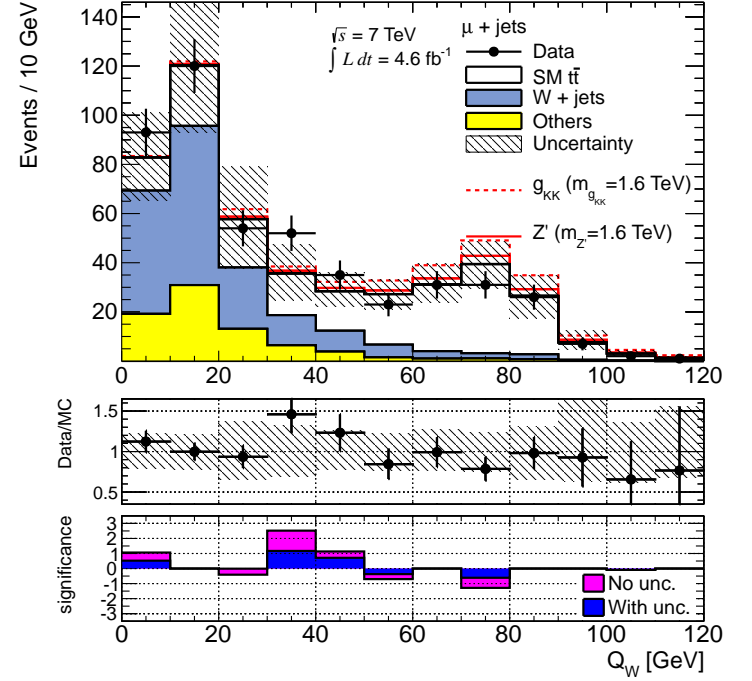
Figure C–1: Reconstructed jet mass of the hadronic top candidate in the e+jets (a) and the μ+jets (b) channels, after the final selection of events, except the requirements on the candidates reconstructed mass and Q_W observables. The uncertainty corresponds to the (bin by bin) quadratic sum of all sources of uncertainties (including the statistical uncertainty of the MC samples) considered in the analysis. The statistical significance of the difference between data and the predicted background is shown in the bottom inset. Hypothetical signals (a Z' with $m_{Z'} = 1.6$ TeV and a g_{KK} with $m_{g_{KK}} = 1.6$ TeV) are shown on top of the expected Standard Model background.

Figure C–2: Reconstructed jet Q_W value of the hadronic top candidate in the e+jets (a) and the μ+jets (b) channels, after the final selection of events, except the requirements on the candidates reconstructed mass and Q_W observables. The uncertainty corresponds to the (bin by bin) quadratic sum of all sources of uncertainties (including the statistical uncertainty of the MC samples) considered in the analysis. The statistical significance of the difference between data and the predicted background is shown in the bottom inset. Hypothetical signals (a Z' with $m_{Z'} = 1.6$ TeV and a g_{KK} with $m_{g_{KK}} = 1.6$ TeV) are shown on top of the expected Standard Model background.
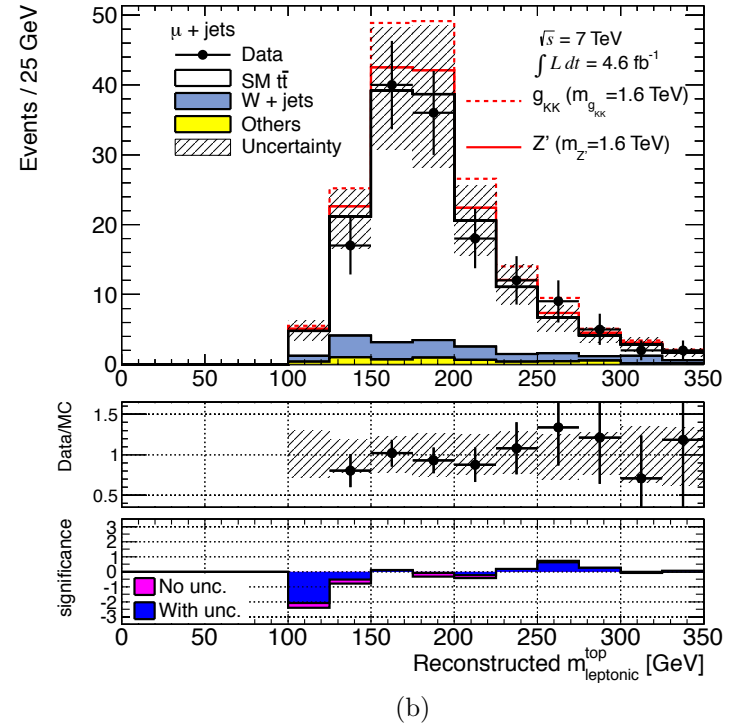
Figure C–3: Leptonic top candidate reconstructed mass in the e+jets (a) and the μ+jets (b) channels, after the final selection of events, except the requirement on candidates mass. The uncertainty corresponds to the (bin by bin) quadratic sum of all sources of uncertainties (including the statistical uncertainty of the MC samples) considered in the analysis. The statistical significance of the difference between data and the predicted background is shown in the bottom inset. Hypothetical signals (a Z' with $m_{Z'} = 1.6$ TeV and a g_{KK} with $m_{g_{KK}} = 1.6$ TeV) are shown on top of the expected Standard Model background.

REFERENCES

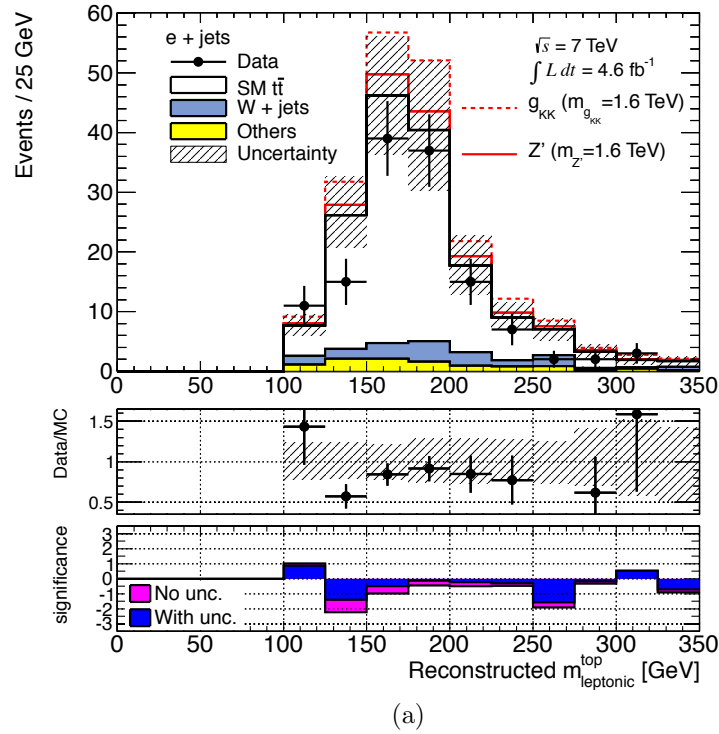[1] Particle Data Group Collaboration, J. Beringer *et al.*, *Review of Particle Physics (RPP)*, Phys. Rev. **D86** (2012) 010001.

[2] Wikipedia, "Standard Model." `http://en.wikipedia.org/wiki/File:Standard_Model_of_Elementary_Particles.svg`. [Online; accessed August 2013].

[3] S. Glashow, *Partial symmetries of weak interactions*, Nucl. Phys. **22** (1961) 579–588.

[4] A. Salam and J. Ward, *Electromagnetic and weak interactions*, Phys. Lett. **13** no. 2 (1964) 168 – 171.

[5] S. Weinberg, *A model of leptons*, Phys. Rev. Lett. **19** (1967) 1264–1266.

[6] CMS Collaboration, *Observation of a new boson at a mass of 125 GeV with the CMS experiment at the LHC*, Phys. Lett. **B716** (2012) 30–61, `arXiv:1207.7235 [hep-ex]`.

[7] ATLAS Collaboration, *Observation of a new particle in the search for the Standard Model Higgs boson with the ATLAS detector at the LHC*, Phys. Lett. **B716** (2012) 1–29, `arXiv:1207.7214 [hep-ex]`.

[8] P. W. Higgs, *Broken symmetries, massless particles and gauge fields*, Phys. Lett. **12** no. 2 (1964) 132 – 133.

[9] P. W. Higgs, *Broken symmetries and the masses of gauge bosons*, Phys. Rev. Lett. **13** (1964) 508–509.

[10] G. S. Guralnik, C. R. Hagen and T. W. B. Kibble, *Global conservation laws and massless particles*, Phys. Rev. Lett. **13** (1964) 585–587.

[11] F. Englert and R. Brout, *Broken symmetry and the mass of gauge vector mesons*, Phys. Rev. Lett. **13** (1964) 321–323.

[12] A. S. Kronfeld and C. Quigg, *Resource Letter: Quantum Chromodynamics*, Am. J. Phys. **78** (2010) 1081–1116, `arXiv:1002.5032 [hep-ph]`.

[13] R. P. Feynman, *Very high-energy collisions of hadrons*, Phys. Rev. Lett. **23** (1969) 1415–1417.

[14] J. Bjorken and E. A. Paschos, *Inelastic Electron Proton and gamma Proton Scattering, and the Structure of the Nucleon*, Phys. Rev. **185** (1969) 1975–1982.

[15] G. Altarelli and G. Parisi, *Asymptotic Freedom in Parton Language*, Nucl. Phys. **B126** (1977) 298.

[16] K. G. Wilson, *Confinement of quarks*, Phys. Rev. D **10** (1974) 2445–2459.

[17] H. D. Politzer, *Reliable Perturbative Results for Strong Interactions?*, Phys. Rev. Lett. **30** (1973) 1346–1349.

[18] D. J. Gross and F. Wilczek, *Ultraviolet Behavior of Non-Abelian Gauge Theories*, Phys. Rev. Lett. **30** (1973) 1343–1346.

[19] J. C. Collins, D. E. Soper and G. F. Sterman, *Factorization of Hard Processes in QCD*, Adv. Ser. Direct. High Energy Phys. **5** (1988) 1–91, `arXiv:hep-ph/0409313 [hep-ph]`.

[20] R. P. Feynman, *The Theory of Positrons*, Phys. Rev. **76** (1949) 749–759.

[21] CDF Collaboration, F. Abe *et al.*, *Observation of top quark production in* $p\bar{p}$ *collisions with the collider detector at Fermilab*, Phys. Rev. Lett. **74** (1995) 2626–2631.

[22] D0 Collaboration, S. Abachi *et al.*, *Observation of the top quark*, Phys. Rev. Lett. **74** (1995) 2632–2637.

[23] A. Heinson. `http://www-d0.fnal.gov/Run2Physics/top/top_public_web_pages/top_feynman_diagrams.html`.

[24] A. Martin, W. Stirling, R. Thorne and G. Watt, *Parton distributions for the LHC*, Eur. Phys. J. **C63** (2009) 189–285, `arXiv:0901.0002 [hep-ph]`.

[25] M. Cacciari, M. Czakon, M. Mangano, A. Mitov and P. Nason, *Top-pair production at hadron colliders with next-to-next-to-leading logarithmic*

soft-gluon resummation, Phys. Lett. **B710** (2012) 612–622, `arXiv:1111.5869` `[hep-ph]`.

[26] C. T. Hill, *Topcolor assisted technicolor*, Phys. Lett. **B345** (1995) 483–489, `arXiv:9411426 [hep-ph]`.

[27] R. M. Harris, C. T. Hill and S. J. Parke, *Cross-section for Topcolor Z'
decaying to top-antitop*, `arXiv:9911288 [hep-ph]`.

[28] R. M. Harris and S. Jain, *Cross-sections for leptophobic Topcolor Z' decaying
to top-antitop*, Eur. Phys. J **C72** (2012) 2072, `arXiv:1112.4928 [hep-ph]`.

[29] L. Randall and R. Sundrum, *A large mass hierarchy from a small extra
dimension*, Phys. Rev. Lett. **83** (1999) 3370–3373, `arXiv:9905221 [hep-ph]`.

[30] B. Lillie, L. Randall and L.-T. Wang, *The bulk RS KK-gluon at the LHC*,
JHEP **0709** (2007) 074, `arXiv:0701166 [hep-ph]`.

[31] U. Baur and L. Orr, *Searching for $t\bar{t}$ resonances at the Large Hadron
Collider*, Phys. Rev. **D77** (2008) 114001, `arXiv:0803.1160 [hep-ph]`.

[32] L. Evans and P. Bryant, *LHC Machine*, JINST **3** no. 08 (2008) S08001.

[33] K. Schindl, *Space charge*, CAS - CERN accelerator school : basic course on
general accelerator physics, no. CERN-PS-99-012-DI (1999).
`http://cds.cern.ch/record/384395`.

[34] J.-L. Caron, *Accelerators chain of CERN : operating and approved projects*,
Sep, 2001. `https://cds.cern.ch/record/43487/`.

[35] ATLAS Collaboration. `https://twiki.cern.ch/twiki/bin/view/
AtlasPublic/LuminosityPublicResults#2011_pp_Collisions`.

[36] ATLAS Collaboration, *The ATLAS experiment at the CERN Large Hadron
Collider*, JINST **3** no. 08 (2008) S08003.

[37] J. Pequenao, *Computer generated image of the whole ATLAS detector*, Mar,
2008. `https://cds.cern.ch/record/1095924`.

[38] J. Pequenao and P. Schaffner, *A computer generated image representing how
ATLAS detects particles*, Jan, 2013. `https://cds.cern.ch/record/1505342`.

[39] J. Pequenao, *Computer generated image of the ATLAS inner detector*, Mar, 2008. `https://cds.cern.ch/record/1095926`.

[40] ATLAS Collaboration, *ATLAS pixel detector electronics and sensors*, JINST **3** no. 07 (2008) P07007.

[41] ATLAS Collaboration, *Beam tests of ATLAS SCT silicon strip detector modules*, Nucl. Instrum. Meth. **A538** no. 1–3 (2005) 384 – 407.

[42] ATLAS Collaboration, *The ATLAS Transition Radiation Tracker (TRT) proportional drift tube: design and performance*, JINST **3** no. 02 (2008) P02013.

[43] J. Pequenao, *Computer generated image of the ATLAS calorimeter*, Mar, 2008. `https://cds.cern.ch/record/1095927`.

[44] M. Bosman *et al.*, *Developments for a scintillator tile sampling hadron calorimeter with longitudinal tile configuration*, CERN-DRDC-93-3, DRDC-P-46 (1993). `https://cds.cern.ch/record/292990`.

[45] GEANT4 Collaboration, S. Agostinelli *et al.*, *GEANT4: A simulation toolkit*, Nucl. Instrum. Meth. **A506** (2003) 250–303.

[46] ATLAS Collaboration, *The ATLAS simulation infrastructure*, Eur. Phys. J **C70** (2010) 823–874, `arXiv:1005.4568 [physics.ins-det]`.

[47] S. Frixione, F. Stoeckli, P. Torrielli, B. R. Webber and C. D. White, *The MCatNLO 4.0 event generator*, `arXiv:1010.0819 [hep-ph]`.

[48] G. Corcella *et al.*, *HERWIG 6.5 release note*, `arXiv:0210213 [hep-ph]`.

[49] J. Butterworth, J. R. Forshaw and M. Seymour, *Multiparton interactions in photoproduction at HERA*, Z. Phys. **C72** (1996) 637–646, `arXiv:9601371 [hep-ph]`.

[50] H.-L. Lai *et al.*, *New parton distributions for collider physics*, Phys. Rev. **D82** (2010) 074024, `arXiv:1007.2241 [hep-ph]`.

[51] M. L. Mangano, M. Moretti, F. Piccinini, R. Pittau and A. D. Polosa, *ALPGEN, a generator for hard multiparton processes in hadronic collisions*, JHEP **0307** (2003) 001, `arXiv:0206293 [hep-ph]`.

[52] J. Pumplin *et al.*, *New generation of parton distributions with uncertainties from global QCD analysis*, JHEP **0207** (2002) 012, `arXiv:0201195 [hep-ph]`.

[53] B. P. Kersevan and E. Richter-Was, *The monte carlo event generator AcerMC version 2.0 with interfaces to PYTHIA 6.2 and HERWIG 6.5*, `arXiv:0405247 [hep-ph]`.

[54] T. Sjostrand, S. Mrenna and P. Z. Skands, *PYTHIA 6.4 physics and manual*, JHEP **0605** (2006) 026, `arXiv:0603175 [hep-ph]`.

[55] A. Sherstnev and R. Thorne, *Parton distributions for LO generators*, Eur. Phys. J **C55** (2008) 553–575, `arXiv:0711.2473 [hep-ph]`.

[56] M. Aliev *et al.*, *HATHOR: HAdronic Top and Heavy quarks crOss section calculatoR*, Comput. Phys. Commun. **182** (2011) 1034–1046, `arXiv:1007.1327 [hep-ph]`.

[57] R. Gavin, Y. Li, F. Petriello and S. Quackenbush, *W physics at the LHC with FEWZ 2.1*, `arXiv:1201.5896 [hep-ph]`.

[58] C.-H. Kom and W. J. Stirling, *Charge asymmetry in W + jets production at the LHC*, Eur. Phys. J **C69** (2010) 67–73, `arXiv:1004.3404 [hep-ph]`.

[59] ATLAS Collaboration, *A search for $t\bar{t}$ resonances in the lepton plus jets final state with ATLAS using 4.7 fb^{-1} of pp collisions at $\sqrt{s} = 7$ TeV*, Phys. Rev. **D88** (2013) 012004, `arXiv:1305.2756 [hep-ex]`.

[60] J. M. Campbell and R. K. Ellis, *An update on vector boson pair production at hadron colliders*, Phys. Rev. **D60** (1999) 113006, `arXiv:9905386 [hep-ph]`.

[61] N. Kidonakis, *Two-loop soft anomalous dimensions for single top quark associated production with a W^- or H^-*, Phys. Rev. **D82** (2010) 054018, `arXiv:1005.4451 [hep-ph]`.

[62] N. Kidonakis, *Next-to-next-to-leading-order collinear and soft gluon corrections for t-channel single top quark production*, Phys. Rev. **D83** (2011) 091503, `arXiv:1103.2792 [hep-ph]`.

[63] N. Kidonakis, *NNLL resummation for s-channel single top quark production*, Phys. Rev. **D81** (2010) 054028, `arXiv:1001.5034 [hep-ph]`.

[64] J. Gao, C. S. Li, B. H. Li, C.-P. Yuan and H. X. Zhu, *Next-to-leading order QCD corrections to the heavy resonance production and decay into top quark pair at the LHC*, Phys. Rev. **D82** (2010) 014020, `arXiv:1004.0876 [hep-ph]`.

[65] J. Alwall *et al.*, *MadGraph/MadEvent v4: The new web generation*, JHEP **0709** (2007) 028, `arXiv:0706.2334 [hep-ph]`.

[66] ATLAS Collaboration, *Electron performance measurements with the ATLAS detector using the 2010 LHC proton-proton collision data*, Eur. Phys. J **C72** (2012) 1909, `arXiv:1110.3174 [hep-ex]`.

[67] ATLAS Collaboration, *Calorimeter clustering algorithms: description and performance*, ATL-COM-LARG-2008-003. `https://cds.cern.ch/record/1099735`.

[68] ATLAS Collaboration, *Readiness of the ATLAS liquid argon calorimeter for LHC collisions*, Eur. Phys. J **C70** (2010) 723–753, `arXiv:0912.2642 [physics.ins-det]`.

[69] ATLAS Collaboration, *Readiness of the ATLAS tile calorimeter for LHC collisions*, Eur. Phys. J **C70** (2010) 1193–1236, `arXiv:1007.5423 [physics.ins-det]`.

[70] ATLAS Collaboration, *Local hadronic calibration*, ATL-LARG-PUB-2009-001. `https://cds.cern.ch/record/1112035`.

[71] M. Cacciari, G. P. Salam and G. Soyez, *The anti-k(t) jet clustering algorithm*, JHEP **0804** (2008) 063, `arXiv:0802.1189 [hep-ph]`.

[72] S. D. Ellis and D. E. Soper, *Successive combination jet algorithm for hadron collisions*, Phys. Rev. **D48** (1993) 3160–3166, `arXiv:9305266 [hep-ph]`.

[73] ATLAS Collaboration, *Performance of the ATLAS inner detector track and vertex reconstruction in the high pile-up LHC environment*, ATLAS-CONF-2012-042. `https://cds.cern.ch/record/1435196`.

[74] D. Krohn, J. Thaler and L.-T. Wang, *Jet trimming*, JHEP **1002** (2010) 084, `arXiv:0912.1342 [hep-ph]`.

[75] ATLAS Collaboration, *Performance of jet substructure techniques for large-R jets in proton-proton collisions at $\sqrt{s} = 7$ TeV using the ATLAS detector*, JHEP **1309** (2013) 076, `arXiv:1306.4945 [hep-ex]`.

[76] ATLAS Collaboration, *Performance of missing transverse momentum reconstruction in proton-proton collisions at 7 TeV with ATLAS*, Eur. Phys. J **C72** (2012) 1844, `arXiv:1108.5602 [hep-ex]`.

[77] ATLAS Collaboration, *Selection of jets produced in proton-proton collisions with the ATLAS detector using 2011 data*, ATLAS-CONF-2012-020. `https://cds.cern.ch/record/1430034`.

[78] M. H. Seymour, *Searches for new particles using cone and cluster jet algorithms: A Comparative study*, Z. Phys. **C62** (1994) 127–138.

[79] ATLAS Collaboration, *High p_T hadronic top quark identification part 1 : jet mass and YSplitter*, ATL-PHYS-CONF-2008-008. `https://cds.cern.ch/record/1077731`.

[80] J. Butterworth, J. R. Ellis and A. Raklev, *Reconstructing sparticle mass spectra using hadronic decays*, JHEP **0705** (2007) 033, `arXiv:0702150 [HEP-PH]`.

[81] J. Butterworth, B. Cox and J. R. Forshaw, *WW scattering at the CERN LHC*, Phys. Rev. **D65** (2002) 096014, `arXiv:0201098 [hep-ph]`.

[82] ATLAS Collaboration, *Reconstruction of high mass $t\bar{t}$ resonances in the lepton+jets channel*, ATL-PHYS-PUB-2009-081. `https://cds.cern.ch/record/1177410`.

[83] J. Thaler and L.-T. Wang, *Strategies to identify boosted tops*, JHEP **0807** (2008) 092, `arXiv:0806.0023 [hep-ph]`.

[84] ATLAS Collaboration, *Prospects for early $t\bar{t}$ resonance searches in ATLAS*, ATL-PHYS-PUB-2010-008. `https://cds.cern.ch/record/1278454`.

[85] J. Thaler and K. Van Tilburg, *Identifying boosted objects with N-subjettiness*, JHEP **1103** (2011) 015, `arXiv:1011.2268 [hep-ph]`.

[86] K. Rehermann and B. Tweedie, *Efficient identification of boosted semileptonic top quarks at the LHC*, JHEP **1103** (2011) 059, `arXiv:1007.2221 [hep-ph]`.

[87] CMS Collaboration, *Search for resonant $t\bar{t}$ production in lepton+jets events in pp collisions at $\sqrt{s} = 7$ TeV*, JHEP **1212** (2012) 015, `arXiv:1209.4397` `[hep-ex]`.

[88] ATLAS Collaboration, *Muon reconstruction efficiency in reprocessed 2010 LHC proton-proton collision data recorded with the ATLAS detector*, ATLAS-CONF-2011-063. `https://cds.cern.ch/record/1345743`.

[89] ATLAS Collaboration, *Muon momentum resolution in first pass reconstruction of pp collision data recorded by ATLAS in 2010*, ATLAS-CONF-2011-046. `https://cds.cern.ch/record/1338575`.

[90] A. Martin, W. Stirling, R. Thorne and G. Watt, *Uncertainties on alpha(S) in global PDF analyses and implications for predicted hadronic cross sections*, Eur. Phys. J **C64** (2009) 653–680, `arXiv:0905.3531` `[hep-ph]`.

[91] M. Botje *et al.*, *The PDF4LHC working group interim recommendations*, `arXiv:1101.0538` `[hep-ph]`.

[92] A. V. Manohar and M. Trott, *Electroweak sudakov corrections and the top quark forward-backward asymmetry*, Phys. Lett. **B711** (2012) 313–316, `arXiv:1201.3926` `[hep-ph]`.

[93] S. Frixione, P. Nason and C. Oleari, *Matching NLO QCD computations with parton shower simulations: the POWHEG method*, JHEP **0711** (2007) 070, `arXiv:0709.2092` `[hep-ph]`.

[94] S. Alioli, P. Nason, C. Oleari and E. Re, *A general framework for implementing NLO calculations in shower monte carlo programs: the POWHEG BOX*, JHEP **1006** (2010) 043, `arXiv:1002.2581` `[hep-ph]`.

[95] ATLAS Collaboration, *Luminosity determination in pp collisions at $\sqrt{s} = 7$ TeV using the ATLAS detector in 2011*, ATLAS-CONF-2011-116. `https://cds.cern.ch/record/1376384`.

[96] G. Choudalakis and D. Casadei, *Plotting the differences between data and expectation*, Eur. Phys. J Plus **127** (2012) 25, `arXiv:1111.2062` `[physics.data-an]`.

[97] G. Choudalakis, *On hypothesis testing, trials factor, hypertests and the BumpHunter*, `arXiv:1101.0390` `[physics.data-an]`.

[98] L. Lyons, *Open statistical issues in particle physics*, `arXiv:0811.1663`
`[stat.AP]`.

[99] E. Gross and O. Vitells, *Trial factors for the look elsewhere effect in high energy physics*, Eur. Phys. J **C70** (2010) 525–530, `arXiv:1005.1891`
`[physics.data-an]`.

[100] I. Bertram *et al.*, *A Recipe for the construction of confidence limits*,
FERMILAB-TM-2104 (2000).
`http://lss.fnal.gov/archive/2000/tm/TM-2104.pdf`.

[101] T. Bayes, *An essay towards solving a problem in the doctrine of chances.*,
Philosophical Transactions of the Royal Society of London **53** (1763)
370–418. `http://www.stat.ucla.edu/history/essay.pdf`.

[102] CDF Collaboration, T. Aaltonen *et al.*, *A search for resonant production of $t\bar{t}$ pairs in* 4.8 fb^{-1} *of integrated luminosity of $p\bar{p}$ collisions at $\sqrt{s} = 1.96$ TeV*,
Phys. Rev. **D84** (2011) 072004, `arXiv:1107.5063 [hep-ex]`.

[103] CDF Collaboration, T. Aaltonen *et al.*, *Search for resonant production of $t\bar{t}$ decaying to jets in $p\bar{p}$ collisions at $\sqrt{s} = 1.96$ TeV*, Phys. Rev. **D84** (2011)
072003, `arXiv:1108.4755 [hep-ex]`.

[104] D0 Collaboration, V. M. Abazov *et al.*, *Search for a narrow $t\bar{t}$ resonance in $p\bar{p}$ collisions at $\sqrt{s} = 1.96$ TeV*, Phys. Rev. **D85** (2012) 051101,
`arXiv:1111.1271 [hep-ex]`.

[105] CMS Collaboration, *Search for anomalous $t\bar{t}$ production in the highly-boosted all-hadronic final state*, JHEP **1209** (2012) 029, `arXiv:1204.2488 [hep-ex]`.

[106] ATLAS Collaboration, *A search for $t\bar{t}$ resonances in the lepton plus jets final state with ATLAS using 14 fb^{-1} of pp collisions at $\sqrt{s} = 8$ TeV*,
ATLAS-CONF-2013-052. `https://cds.cern.ch/record/1547568`.

[107] CMS Collaboration, *Search for $t\bar{t}$ resonances in semileptonic final state*,
CMS-PAS-B2G-12-006. `https://cds.cern.ch/record/1543467`.

[108] ATLAS Collaboration, *Measurement of the W boson polarization in top quark decays with the ATLAS detector*, JHEP **1206** (2012) 088, `arXiv:1205.2484`
`[hep-ex]`.